AFRL-AFOSR-VA-TR-2016-0346

Comprehensive Study of Plasma-Wall Sheath Transport Phenomena

MITCHELL WALKER
GEORGIA TECH RESEARCH CORPORATION

10/26/2016
Final Report

Air Force Research Laboratory
AF Office Of Scientific Research (AFOSR)/ RTA1
Arlington, Virginia 22203
Air Force Materiel Command

REPORT DOCUMENTATION PAGE

Form Approved
OMB No. 0704-0188

1. REPORT DATE *(DD-MM-YYYY)*	2. REPORT TYPE	3. DATES COVERED *(From - To)*
03-11-2016	Final Performance	01 Jul 2011 to 30 Jun 2016

4. TITLE AND SUBTITLE
Comprehensive Study of Plasma-Wall Sheath Transport Phenomena

5a. CONTRACT NUMBER

5b. GRANT NUMBER
FA9550-11-1-0160

5c. PROGRAM ELEMENT NUMBER
61102F

6. AUTHOR(S)
MITCHELL WALKER

5d. PROJECT NUMBER

5e. TASK NUMBER

5f. WORK UNIT NUMBER

7. PERFORMING ORGANIZATION NAME(S) AND ADDRESS(ES)
GEORGIA TECH RESEARCH CORPORATION
505 10TH ST NW
ATLANTA, GA 30318-5775 US

8. PERFORMING ORGANIZATION REPORT NUMBER

9. SPONSORING/MONITORING AGENCY NAME(S) AND ADDRESS(ES)
AF Office of Scientific Research
875 N. Randolph St. Room 3112
Arlington, VA 22203

10. SPONSOR/MONITOR'S ACRONYM(S)
AFRL/AFOSR RTA1

11. SPONSOR/MONITOR'S REPORT NUMBER(S)
AFRL-AFOSR-VA-TR-2016-0346

12. DISTRIBUTION/AVAILABILITY STATEMENT
A DISTRIBUTION UNLIMITED: PB Public Release

13. SUPPLEMENTARY NOTES

14. ABSTRACT

In order to facilitate the development of the next generation of electric propulsion (EP) devices for USAF space assets and overcome current limitations in power density and specific mass, investigators from Georgia Institute of Technology (GT), University of Alabama (UA), and George Washington University (GWU) performed a comprehensive multidisciplinary study on the nature and transport properties of the interaction between a plasma and a confining wall material. Hysteresis effects observed in the floating potential of wall material samples immersed in a low-temperature plasma were studied. Hysteresis is found to be due to secondary electron emission from the wall material surface. The impact of surface roughness and sheath-scale surface profiles on space charge saturation of plasma sheaths was investigated. The preliminary results of models have proven that the thermal conductivity distribution largely impacts the crack nucleation and propagation process in boron nitride. The experimental investigation of the erosion of stressed materials was continued for fused silica and M26 borosil. The work shows that the evolution of the M26 surface is governed by the complex microstructure of the material.

15. SUBJECT TERMS
Plasma

16. SECURITY CLASSIFICATION OF:			17. LIMITATION OF ABSTRACT	18. NUMBER OF	19a. NAME OF RESPONSIBLE PERSON
a. REPORT	b. ABSTRACT	c. THIS PAGE			BIRKAN, MITAT

Unclassified	Unclassified	Unclassified	UU	**PAGES**	**19b. TELEPHONE NUMBER** *(Include area code)* 703-696-7234

Comprehensive Study of Plasma-Wall Sheath Transport Phenomena Final Report 2016

Prof. Mitchell L. R. Walker
Georgia Institute of Technology
Aerospace Engineering
Atlanta, GA 30332

Dr. W. Jud Ready
Georgia Tech Research Institute
Electro-Optical Systems Laboratory
Atlanta, GA 30332

Prof. Greg Thompson
University of Alabama
Metallurgical and Materials Engineering
Tuscaloosa, AL 35487

Prof. Julian J. Rimoli
Georgia Institute of Technology
Aerospace Engineering
Atlanta, GA 30332

Prof. Michael Keidar
George Washington University
Micropropulsion and Nanotechnology Laboratory
Washington, DC 20052

Abstract

In order to facilitate the development of the next generation of electric propulsion (EP) devices for USAF space assets and overcome current limitations in power density and specific mass, investigators from Georgia Institute of Technology (GT), University of Alabama (UA), and George Washington University (GWU) performed a comprehensive multidisciplinary study on the nature and transport properties of the interaction between a plasma and a confining wall material. In year five, the High-Power Electric Propulsion lab at GT continued research into plasma sheath physics. Hysteresis effects observed in the floating potential of wall material samples immersed in a low-temperature plasma were studied. Hysteresis is found to be due to secondary electron emission from the wall material surface. The University of Alabama performed two studies in year five. The first effort investigated the influence of surface roughness on electron emission from graphite and graphite coated HET materials. The second study was performed in concert with the sheath experiments conducted at HPEPL: Investigating the effect of Debye-scale surface features on space charge saturation of plasma sheaths. In year five, the Computational Solid Mechanics Lab (CSML) at Georgia Tech created models of the development of cracks in polycrystalline materials. Preliminary results have proven that the thermal conductivity distribution largely impacts the crack nucleation and propagation process. In addition, CSML contributed towards a concurrent multi-scale model capable of predicting the thermo-mechanical response of polycrystalline structures including crack nucleation and propagation. The experimental investigation of the erosion of stressed materials was continued for fused silica and M26 borosil. The cell pattern observed created on fused silica samples was successfully modeled as a result of the angle-dependence of the sputtering yield of fused silica. Unlike fused silica, the work shows that the evolution of the M26 surface is governed by the complex microstructure of the material.

Introduction / Background

1.1 Motivation

Though USAF needs are currently being met by EP devices, a revolutionary understanding of the plasma-wall interaction is required to provide the power density increases necessary for future USAF needs. ***Current efforts to increase thruster power density have hit a limit that is indicated to be a direct function of the interaction of the thruster discharge with the chamber wall.*** Additionally, erosion of walls that occurs over the operating life of a thruster is currently the limiting factor for lifetime of EP devices.

Research endeavors in SOA Hall effect thrusters (HETs) have reached a point of diminishing return at an anode efficiency of ~70% at high specific impulse (I_{sp}) and ~93 mN/kW at low I_{sp}. In addition to performance limitations, current SOA HET systems are limited to a specific mass of approximately 180 W/kg. [1] Propulsion systems must have much higher specific masses to truly enable future AF space assets. The next generation of EP devices should increase the system specific mass by at least an order of magnitude while maintaining efficiencies greater than 70% in high-I_{sp} mode or >100 mN/kW in low-I_{sp} mode.

The only way to improve thruster specific mass is to increase the power density of the propulsion devices. This makes the plasma-wall interaction incredibly critical: wall erosion and energy loss mechanisms both affect propulsion device performance directly and dictate the wall material choice. Ideally, the wall will serve only to fix the physical location of the plasma. In reality, the wall absorbs energy from the plasma, exchanges energetic electrons for low energy electrons through secondary electron emission, neutralizes ions, and introduces undesired sputtered wall material. All of these processes serve to decrease the specific power of the propulsion device.

The limitation in power density is most clearly supported by current and previous efforts to increase the thrust-to-power (T/P) ratio of the HET. To increase the T/P ratio requires a direct increase in the ion number density in the discharge channel. All efforts show that there is a maximum threshold of this density, which is independent of acceleration voltage. That is, even when the energy of the electron population of the Hall current is sufficient for ionization, the device is unable to efficiently generate and accelerate high-density plasmas. Experimental results show that this limitation is a direct function of the sheath generated at the discharge chamber wall. ***Thus, significant improvements in the specific mass of electric propulsion devices require a revolutionary understanding of the transport mechanisms in the plasma-wall interaction.***

1.2 Hypothesis

The hypothesis of this research effort is that standard plasma assumptions break down in the plasma sheath and are greatly affected by the microstructural properties of the wall. It is proposed to apply a plasma- and materials-centric experimental program to the problem of plasma-wall interactions. Measurements and theoretical analysis of the plasma properties inside the plasma sheath, as well as measurements and modeling of the material response to the plasma, a generate models of the plasma-wall interaction that can predict the effect of wall material on bulk plasma properties. ***This approach will be a revolutionary shift in plasma-wall interaction studies as it is the first time the problem of plasma-wall interactions is approached from both a plasma physics and a materials science point of view.***

Questions that we aim to answer to investigate this hypothesis:

- What factors predict how the ion and electron densities of the plasma change near the wall?
- What factors predict how the electric field and plasma potential change near the wall?
- What factors predict the rate of mass transfer from the wall to the plasma (erosion) and the rate of mass transfer from the plasma to the wall (implantation?)
- What factors predict the thermal energy transfer between the plasma and wall?
- What plasma conditions most strongly affect the wall (ion energy distribution, incident ion flux, ion temperature, electron temperature, plasma potential?)
- What wall material factors most strongly affect the plasma (temperature, secondary electron emission yield, atomic sputtering yield, surface roughness?)

1.3 Research Objective

We conducted a highly integrated, cumulative research program to develop an understanding of the plasma-wall interaction and how both the sheath and the wall material affect the plasma as a whole. ***The research aims to determine the fundamental transport properties (mass, charge, and energy) within the plasma sheath, and determine the***

relationship between plasma properties and wall surface modification as a function of wall material. This research provides, for the first time, fundamental relationships between the plasma and wall, that will allow propulsion designers to take advantage of the plasma sheath and not be hindered by it.

1.4 Collaborative Research Plan

The research effort was organized into two major research areas: (1) interrogation and theoretical modeling of ***the plasma*** up to the wall boundary, and (2) interrogation and modeling of ***the wall*** up to the plasma boundary. As Figure 1 below illustrates, the collaborative research team is composed of functional relationships between models and experimental data for both the plasma and wall sides of the investigation. With that in hand, the models are used to predict and confirm plasma-wall interactions, with additional experimental data incorporated as it becomes available.

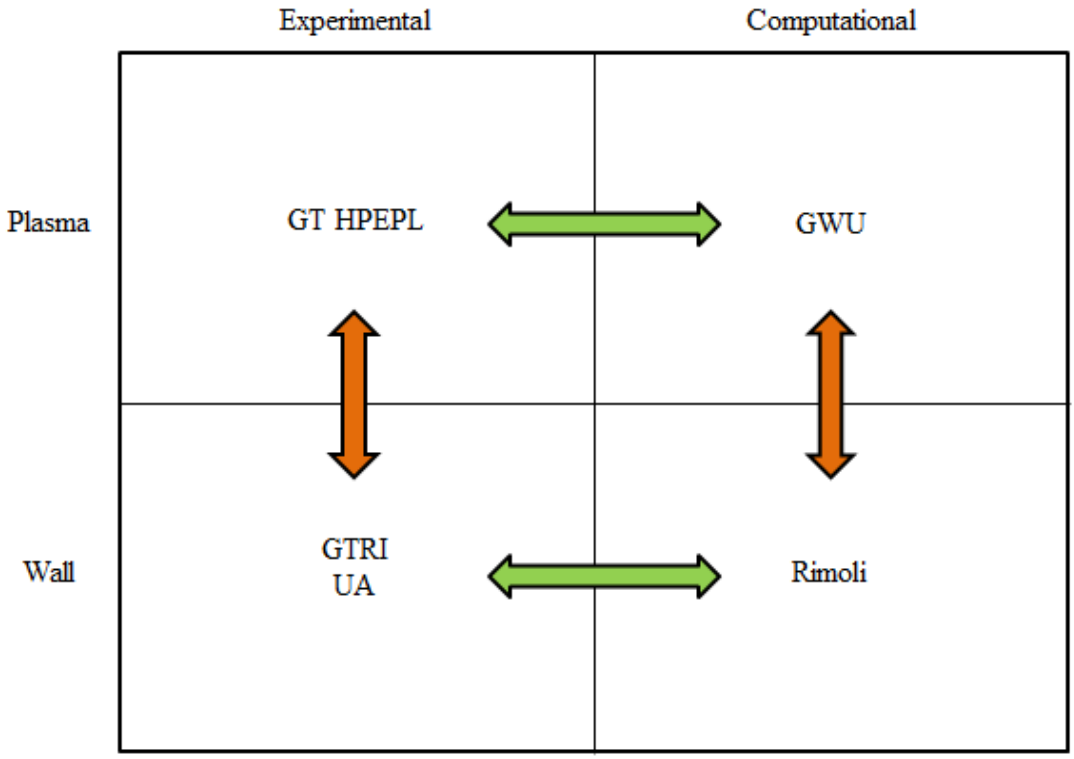

Figure 1. Collaborative Research Strategy: Phase I: Experimental ←→ Computational (Horizontal) Phase II: Refinement / Prediction (Vertical)

In particular:

(1) Plasma:

- GT HPEPL developed a standardized plasma cell that is compatible with the sheath thicknesses required for this work. GT interrogated the plasma up to the wall boundary, and worked with current transport theory to develop theoretical relationships between the bulk plasma and transport to the wall.
- GWU developed plasma simulations with the ability to resolve the plasma-wall interaction, and couple inputs and outputs with GT to experimentally verify models.

(2) Wall:

- GTRI worked with GT HPEPL to generate and provide eroded wall material samples to UA and to GT Professor Julian Rimoli.

- UA provided multi-dimensional and multi-length scale characterization of these samples, that provided the basis for a microstructural model. Data analysis performed in parallel with the model development allowed the model to be refined as new data became available.
- GT Professor Rimoli studied these samples in order to investigate the mechanisms that underlie thruster erosion.

1.5 Year One (2011-2012) Research Activities

Over the course of the first year of the project (2011-2012,) large-scale nominal plasma environment was designed, built, and characterized at the GT High-Power Electric Propulsion Laboratory (GT HPEPL), operable on Argon gas at pressures at or above 2 x 10^{-4} Torr, with preliminary electron and ion density measurements on the order of 10^{15} m^{-3}. Georgia Tech Research Institute (GTRI) worked with GT HPEPL to characterize an ion-assisted deposition plasma source (IAD) for use as a controlled plasma exposure environment for samples of wall material. The IAD supplies ions with mean energy adjustable between 40 and 160 eV. UA developed the capability to characterize the microstructure and phase of Boron Nitride (BN) wall material samples and performed analyses using X-Ray Diffraction (XRD), Scanning Electron Microscopy (SEM), Atomic Force Microscope (AFM), and Transmission Electron Microscopy (TEM). Surface mechanical properties were also measured using Nano-Indentation (NI). GWU developed a plasma simulation methodology that accounts for the multiple length scales governing the plasma in an EP device. GWU performed and published simulations studying the interaction of the near-wall plasma sheath with the magnetic field, and modeled the sheath of the GT HPEPL plasma environment using the experimental data from GT HPEPL, finding nominal agreement between simulation and experiment.

1.6 Year Two (2012-2013) Research Activities

Over the course of the second year of the project, activities continued on both the plasma and materials sides. On the plasma side, a more quiescent and lower density (10^{13} m^{-3}) plasma environment was designed and built at GT HPEPL, which yielded a more stable plasma environment for the interrogation of the sheaths around wall material samples. Experimental observations were made at GT HPEPL of two phenomena that can be of dominant importance in determining the plasma sheath structure: nonlocal high-energy plasma electrons and secondary electron emission (SEE) from the wall material. A transition was observed in the sheath potential structure when high-energy electrons triggered high levels of SEE from the wall, entering a regime with a low sheath potential drop of the order of the electron temperature. Transitions and collapsed sheaths of this nature are thought to occur in HET discharge channels.

GWU performed a simulation of the GT HPEPL experiments on plasma sheaths with nonlocal fast electron populations, and the results obtained agreed well with the experimental results when SEE was not strong but deviated in conditions of strong SEE. GWU also conducted an investigation into the validity of the thermalized potential approximation (a widely used simplification in HET design that fixes the plasma equipotentials to follow the magnetic field lines within a given factor) as a function of magnetic field shape, and determined that it is a valid approximation in regions where electrostatic drifts and pressure forces are not substantial enough to pull the electrons off of the magnetic field lines, such as near a HET channel exit. However, in regions of lower magnetic field strength and/or greater opposing forces such as a HET near-anode region or separatrix, the approximation breaks down and a 2D potential solver must be used.

On the materials side, a HET wall, subjected to xenon plasma at power levels of 1.5-5 kW for approximately 2000 hours, was characterized to determine the major features of erosion. Depending upon location in the chamber wall, the following three distinct regions were identified: low erosion, mild erosion, and high erosion. The low erosion region did not show any distinct erosion features. The mild erosion region showed the onset of surface roughening in the form of surface striations and protrusions from line-of-sight sputter erosion. The onset of micro-cracking in the BN was also observed. The high erosion region exhibited significant surface roughening, exfoliation of BN from the surface and micro-cracking within the BN. In addition, a darker discoloration was present on the surface of the high erosion region and is contributed to carbon deposits from the downstream graphite beam dump in the HET. The exfoliation of BN in the high erosion region resulted in the preferential retention of silica in the XPS analysis. BN's preferential loss left smooth silica surfaces. The major source of mechanical stress that contributed to the cracking is the anisotropic thermal expansion of BN in the silica matrix. As BN thermally expands in the more rigid silica matrix, in response to the high-temperature plasma, stress concentrations develop resulting in micro-cracking parallel to the basal plane. In some instances, the surface BN is liberated from the matrix material to accommodate this expansion. The prevalent micro-cracking in BN is suggestive of weak structural integrity during plasma exposure.

In order to develop predictive capability of the microstructure evolutions characterized experimentally, the GT materials modeling effort began the development of two main models: a 3D model of differential atomic sputtering and a 3D model of thermal cracks in heterogeneous ceramic compounds. The model of atomic sputtering incorporates the interaction of the material grain geometry with sputtering and with the shadowing of the ion beam, producing surface features and roughness reminiscent of the eroded channel wall studied in year one. It also predicts surface roughness, which is now known to be important for secondary electron emission and the details of the material may play a role in the formation of large-scale features unanticipated by less detailed models. The 3D model of thermal cracks is based on a direct numerical simulation approach in which heterogeneities, i.e. different phases in the material, are explicitly accounted for. Material evolution based on cracking behavior may represent another dimension which is not captured by a sputtering-only model. A combination of both models would possibly help explain the presence of planar silica surfaces in the eroded material: as cracks are created, grains may get detached and pulled out by incident ions.

1.7 Year Three (2013-2014) Research Activities

In year three, GT HPEPL continued experimental measurements of the effects of secondary electron emission on the plasma sheath. In year three, experiments were performed to compare smooth and roughened wall samples, and the effects of secondary electron emission, particularly the electron bombardment energies at which the sheath transitioned from a classical sheath to one with a lower magnitude potential drop. Smooth and roughened (9.08 μm RMS roughness) BN samples were compared, and it was found that the smooth sample's sheath transitioned at lower electron incident energies than the rough sheath samples. The transition mechanism is similar to a space-charged limited sheath predicted by Hobbs and Wesson, but the conditions leading to transition are different due to a population of energetic electrons with energy greater than the colder electrons in the plasma.

In year three, George Washington University developed a multi-scale model of the magnetized plasma discharge, in which a kinetic treatment is used to model electron transport along the magnetic field lines, while a 2D macroscopic model is employed for the global thruster discharge. This multi-scale formulation offers the benefit of self-consistently calculating electron motilities, while at the same time retaining the reduced computational requirements of a hybrid model.

George Washington University also modeled the effect of the surface roughness on SEE yield, and therefore on the breakdown of the classic Child-Langmuir sheath experimentally observed by HPEPL. It was predicted that the surface roughness reduces the effective SEE yield, due to emitted electrons being trapped in cavities and reabsorbed to the surface. It is possible for the SEE yield of a smooth wall to be above unity, and for a rough wall under similar conditions to be below unity. The reduced SEE yield produced predictions which agreed well with the HPEPL measurements.

In year three, University of Alabama pursued thermal cycling experiments for M26 and HP grade boron nitride samples. Each time the temperature and number of thermal cycles were varied. Thermal cycling was found to cause the nucleation and growth of cracks in the material. The rigid phase boundaries in M26 BN-SiO_2 were found to favor nucleation of new cracks, whereas the HP-grade BN samples favored increased growth of existing cracks. To theoretically ground the observations, density functional theory calculations were performed to determine the cohesive energy of the planes in BN. The basal plane was confirmed to have much lower cohesive energy than other directions, explaining the prevalence of cracks along the basal plane, and helping to generalize BN results to other materials.

The experiments and simulations of the plasma group highlighted the importance of coupling between the plasma and wall due to SEE. To this end, the UA team began collaborating with Dr. Alan Joly at the Pacific Northwest National Laboratory (PNNL) in using Photoemission Electron Microscopy (PEEM) to characterize the electron emission characteristics of wall materials. Concurrent with this development, LaB_6 materials were procured. Vacuum plasma spraying and spark plasma sintering were used as deposition methods, and the ability to mitigate vapor-pressure losses of BN was confirmed. Going forward, the combination of PEEM studies with the surface characterization techniques already developed permitted the quantitative and tightly coupled study of the effect of surface topology and electron emission on the plasma and wall structure evolution.

In year three, the GT materials modeling group began development of a model for the nucleation and propagation of thermo-mechanical micro cracking in heterogeneous ceramic compounds (HCC), such as BN-SiO_2. To accurately capture the underlying physics leading to the development of failure, a finite element (FE) model must include the microstructural details of the material. A parametric meshing tool able to incorporate the fully 3D mesoscale description of the HCC was developed, including the ability to model multiple material phases and voids. The influence of the phase volume fractions on the mean hydrostatic stress for a model subjected to a uniform 500 K temperature increase was investigated. The previous investigation demonstrated the necessity of incorporating cracks

into our model. The failure of the material may influence the physical behavior by releasing stresses and by affecting the thermal conductivity. To include fracture, the model must account for jumps in the displacement fields that are accounted for through cohesive zone elements introduced between bulk elements. These elements are characterized by a binding law that relates the opening to the applied stress on the element. In a parallel HPC framework, the result must be independent of the partitioning of the model. Implementation of a model to capture micro-cracking was begin in year three.

A potential mechanism to explain the development of anomalous erosion ridges in Hall Effect Thrusters was investigated by Dr. Aaron Schinder. These anomalous ridges, seen at the end of long duration life testing, are currently unexplained. The potential mechanism, referred to as the Strain Relief Hypothesis (SRH) is inspired by an instability investigated in the acid etching of aluminum by Kim, Hurtado, and Tan [2]. A computational model was created of an instability generated by the release of strain energy. The model confirmed certain aspects of the behavior of the analytical model for the SRH were reproduced for an arbitrary starting surface profile: namely the $1/\text{stress}^2$ dependence on the wavelength scale of the stable and unstable modes amplified by the resulting growth process.

An experiment was designed to investigate growth processes and instabilities in the plasma erosion of materials. Specifically, the experiment was intended to isolate and test the strain relief hypothesis. In year three, initial trials of the experiment were conducted in Georgia Tech Research Institute's (GTRI's) Ion Assisted Deposition (IAD) chamber. Initial results were ambiguous and difficult to reproduce, so further improvements to the experiment, test procedure, and instrumentation were made throughout 2013, including a pause to repair the IAD plasma source. The experiment was continued in year four and year five. The results are described later in this document.

In year three, GTRI performed pure electron beam bombardment of samples. The electron beam bombardment of BN samples produced discoloration at the point of impingement.

1.8 Year Four (2014-2015) Research Activities

In year four, new details of the plasma wall interaction were investigated, and continued collaboration between the groups supported the research effort. At HPEPL, experiments were conducted with a metal electrically conducting wall to improve measurements of the floating wall potential and the sheath structure. Year three measurements of the dependence of the sheath structure on the SEE and electron energy were sent to GWU for modeling. Wall temperature effects seen in previous years were found to be the result of outgassing and increased thermal desorption of surface contaminants from the walls. Investigation of features with length scales comparable to the sheath show an interesting potential structure forming on a wall with surface grooves. Finally, the observation was made of sheath scaling with plasma density. At George Washington University, a multi-scale model of the magnetized discharge in a HET was created, which self-consistently calculates electron mobilities while at the same time retaining reduced computational requirements. In addition, simulations of plasma-surface interaction over grooved samples were performed. In GTRI's Ion Assisted Deposition Chamber, an experiment was designed to investigate the growth of surface features while under plasma erosion. A striking cell structure was formed on the surface of pre-roughened fused silica samples eroded by an argon plasma. This growth process was found to be unaffected by mechanical loads applied to a sample and found not to occur when smooth samples were used. The cell pattern was found to appear wherever initial surface roughness exists.

1.9 Year Five (2015-2016):

The remainder of the report details the efforts of each team member to complete their investigations into plasma sheath physics, surface effects, and the effects of stress on plasma-wall interaction and plasma erosion.

Year Five (2015-2016) Research Activities

2.1 GT HPEPL – Measurement of Plasma Sheath Properties

2.1.1 Introduction: Hysteresis and mode transitions in plasma sheath collapse due to secondary electron emission.

The following content is taken from the paper "Hysteresis and mode transitions in plasma sheath collapse due to secondary electron emission."[1] Hysteresis and mode-shifting behavior have been reported in a wide variety of bounded plasma devices, including thermionic filament discharges,[1] magnetized linear plasmas, [2,3] radio-frequency-driven discharges, [4–6] and Hall effect thrusters. [7,8] A number of mechanisms for the observed behavior have been theorized (see, *e.g.*, Ref.4), many having to do with the electron power balance and energy flux to and from the device walls, as mediated by the nonlinear plasma sheath.

Experimental investigations by Takamura *et al.* [3] focused on the plasma-wall interaction and sheath in high-heat-flux plasmas revealed and explained a clear wall-dependent mechanism for hysteresis in the wall floating potential driven by thermionic electron emission from the wall. It is shown that when the plasma heats the wall to a sufficient temperature, thermionic electron emission from the wall causes a space-charge collapse of the magnitude of the sheath potential to the order of the electron temperature or lower/inverse, as described originally by Hobbs and Wesson [9] and recently by Campanell [10] and Sheehan. [11] With the decrease in sheath potential, the electron heat flux to the wall is increased, thereby again increasing thermionic electron emission from the wall. This creates a feedback mechanism and the sheath floating potential and wall temperature shift to a new "collapsed sheath" equilibrium. At a later time, if the heat flux from the plasma is then lowered, Takamura *et al*. observe that the sheath often remains collapsed at lower values of the plasma heat flux than were required to collapse it in the first place. Because the sheath potential has been collapsed, the wall is still receiving elevated heat flux from the plasma and generates enough thermionic electron emission to keep the sheath collapsed. If the heat flux is lowered below a threshold dependent on the wall material work function, the electron emission will become insufficient to maintain the collapsed sheath and the Debye sheath will be re-established. This mechanism explains observed hysteresis in plasmas where thermionic components are employed and heat flux from the plasma is significant.

Several plasma devices that exhibit hysteresis employ dielectric boundaries from which secondary electron emission (SEE) is significant. SEE was theorized to give rise to multi-valued floating potentials of cosmic dust grains in a work by Meyer-Vernet [12]. In first experiments by Nam *et al.*, [13] abrupt jumps were observed in the floating potential of Langmuir probes in a multi-dipole plasma and inferred the existence of multiple stable floating potentials of the probe. Work by Walch *et al.* [14] observed sharp transitions in floating potential of dust grains in response to an energetic electron population. These results suggest that SEE may play an important role in mode-shifts and/or hysteresis in plasma devices as well.

In the current experiment, we monitor floating potential of macroscopic wall material samples as the energy of beam-like electron population is either increased or decreased. This allows us to observe full hysteresis curves of the sample floating potentials. We compare results with a kinetic model [15] and find agreement with a nonlinear s-curve shape prediction of floating potential, similar to the predictions of Meyer-Vernet [12].

2.1.2 Experiments

Experiments are conducted in an open cylindrical multi-dipole plasma device in the Vacuum Test Facility-2 at the Georgia Institute of Technology. Figure 2 shows a schematic of the device and experimental layout. The discharge is operated at an argon gas pressure of 10^{-4} Torr-Ar. The discharge voltage is applied between the hot filaments and the electrically grounded aluminum frame. The discharge current is restrained to 10 mA by limiting the heating current and temperature of the filaments, to attain a plasma density n_e on the order of 10^7 cm^{-3} and a significant fraction of energetic electrons n_{ep} from the filament present in the plasma .The energy of the energetic electrons from the filament is varied by changing the discharge voltage, from 50-200 V in this experiment. The fraction of energetic electrons $\alpha = n_{ep}/n_e$ was measured using a planar Langmuir probe and the method described in Ref. 16, shown in **Figure 3**.

[1] Langendorf, S. J., Walker, M. L. R., "Hysteresis and Mode Transitions in Plasma Sheath Collapse Due to Secondary Electron Emission," Journal of Applied Physics, Volume 119, March 2016, pp. 113305 1-5.

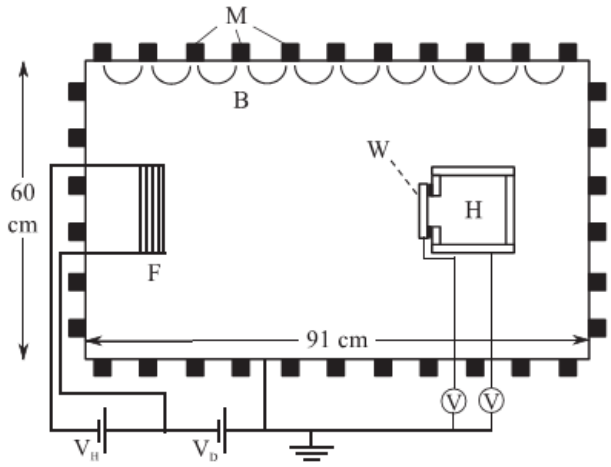

Figure 2. Schematic of the plasma device and experimental layout. M = magnets. B = notional magnetic field. F = filament cathode. W = wall material sample. H = heater volume. V_D = discharge power supply, and V_H = filament heater power supply.

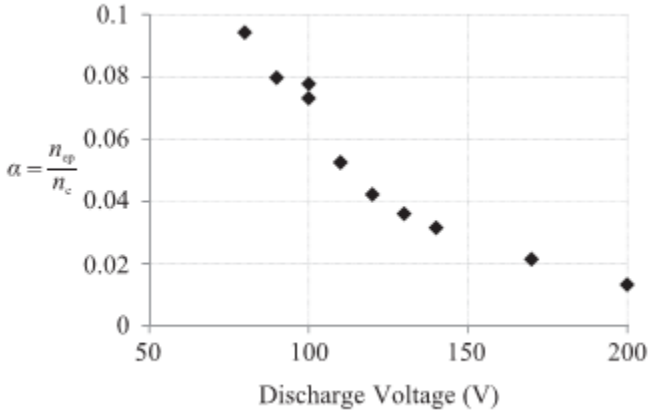

Figure 3. Measured fraction of energetic primary electrons $\alpha = n_{ep}/n_e$ in plasma 100 mm from wall material sample vs. discharge voltage. Relative uncertainty is less than 20%, absolute uncertainty is estimated at a factor of two.

2.1.2.1 LaB_6-coated steel material sample

Three-inch diameter wall material samples are mounted on a 4.5 in.-side cube-shaped sample heater, suspended in the plasma device opposite the discharge filaments. The heater contains coils of heating wire wrapped around the ceramic tubing. The stainless steel body of the heater is electrically isolated from the device frame by a ceramic standoff on its mounting rod. The focus of this part of the experiment was on a LaB_6-coated steel wall material sample. The sample is stood off 1/8 in. from the heater face by ceramic stand-offs and the gap along the perimeter is filled with ceramic adhesive. It is thus electrically isolated from the heater body and can be radiatively heated from the heating elements. A wire was connected to the sample, and its floating potential was measured with a 10 MΩ-impedance ADC channel.

The discharge voltage of the plasma device is varied from 50 to 200 V at a rate of approximately 1 V/s, while the floating potential of the wall material sample is monitored, as shown in Figure 4. The plasma potential remains fairly constant at -21 V, so the primary electron energy is offset from the discharge voltage by this amount but scales linearly with it. Figure 5 plots the results of the floating potential of the wall material sample vs. discharge voltage. The discharge voltage sweep from 50 to 200 V is repeated for heater powers from 170 W to 560 W and resulting average wall temperatures 55 ºC to 390 ºC. The discharge voltages at which the abrupt changes in floating voltage occur are plotted in **Figure 6** in which it is observed that as the heater power and wall temperature is increased, the hysteresis

loop in wall floating potential gradually shrinks and disappears. Concurrently with the disappearance of the hysteresis in floating potential, a glow is observed within the sample heater box, leading the experimenters to infer that plasma forms inside the box at these conditions. Supporting this belief, it is observed that the floating potential of the metal sample heater box and the LaB_6-coated steel sample under investigation become the same at temperatures above 450 ºC, even if the sample is electrically biased using the attached lead.

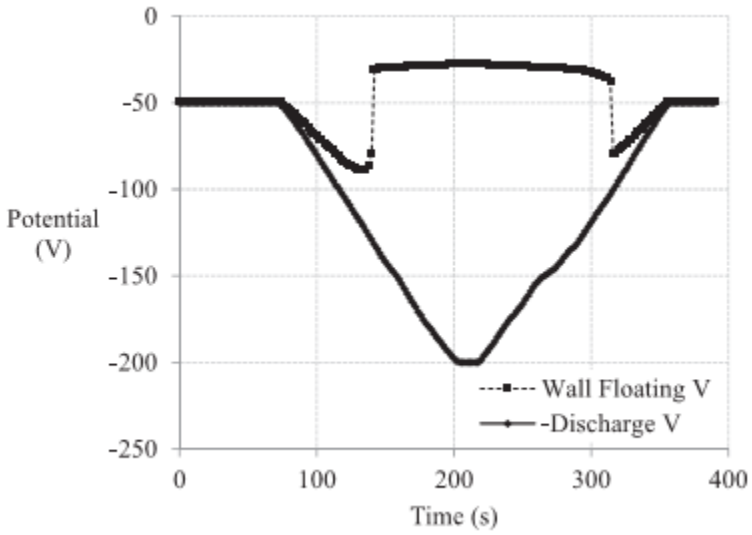

Figure 4. Floating potential of LaB_6-coated steel wall material sample in plasma and discharge voltage vs. time as discharge voltage is varied. The wall temperature is 50 ºC.

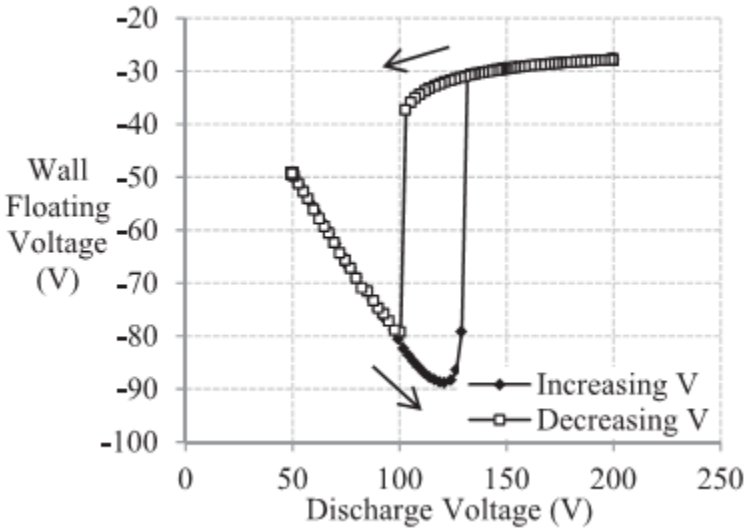

Figure 5. Floating potential of LaB_6-coated steel wall material sample vs. discharge voltage. The wall temperature is 50 ºC.

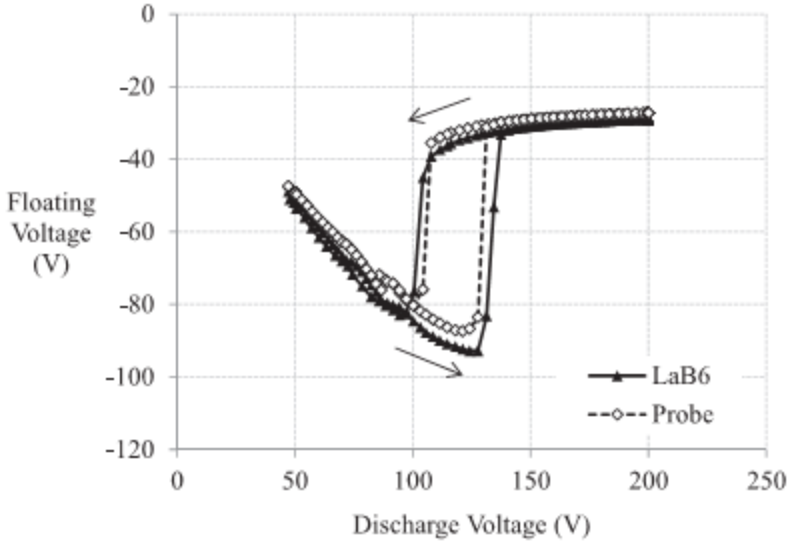

Figure 6. Floating potential of LaB_6-coated steel wall material sample and adjacent probe vs. discharge voltage. The wall temperature is 50 ºC.

2.1.2.2 Boron nitride (BN) sample

Experiments are continued with a roughened BN ceramic sample of equivalent dimensions. The sample had been utilized in previous experiments to do with surface roughness and had been prepared by sanding with 120-grit SiC paper to an average roughness of 10lm. As the sample is not electrically conductive, the floating potential could not be monitored by a simple wire as previously. A small 1-mm half-loop electrostatic probe was positioned on the surface of the device to monitor the floating potential. The probe tip was 0.005 in. diameter thoriated tungsten, and it was supported by a double-bore alumina tube. As the probe formed a small amount of the collecting area with a circle with radius equal to the plasma Debye length (which varied from 7 to 9 mm) on the sample surface, it was reasoned that the floating potential of the probe would be largely governed by the potential of the nearby BN surface. To confirm this, the probe was positioned over the LaB6 sample, and the probe potential was monitored along with that sample, as shown in Figure 7.

Positioning the probe over the rough BN sample, the floating potential of the probe was monitored in a similar study to the LaB6 sample. The results are shown in Figure 8 and Figure 9.

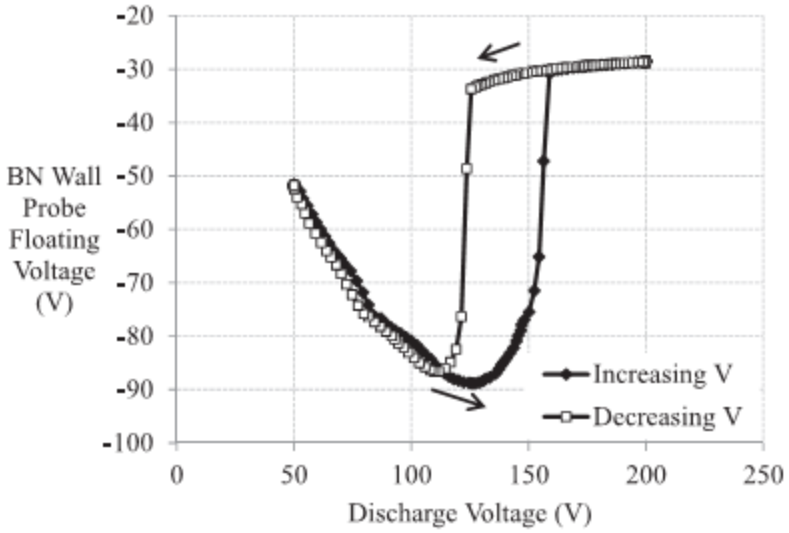

Figure 7. Floating potential of witness probe adjacent to BN sample vs. discharge voltage. The wall temperature is 50 ºC.

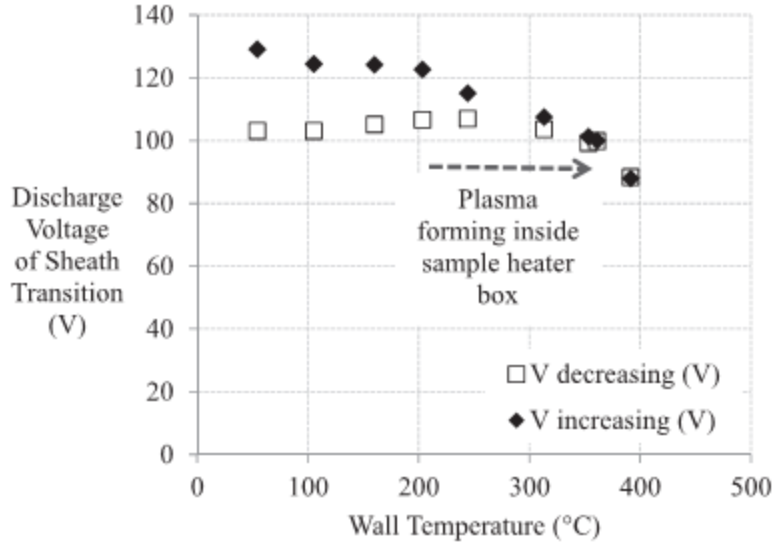

Figure 8. Transition voltages in wall floating potential as a function of wall temperature. Plasma glow observed within heater volume concurrently with the disappearance of hysteresis.

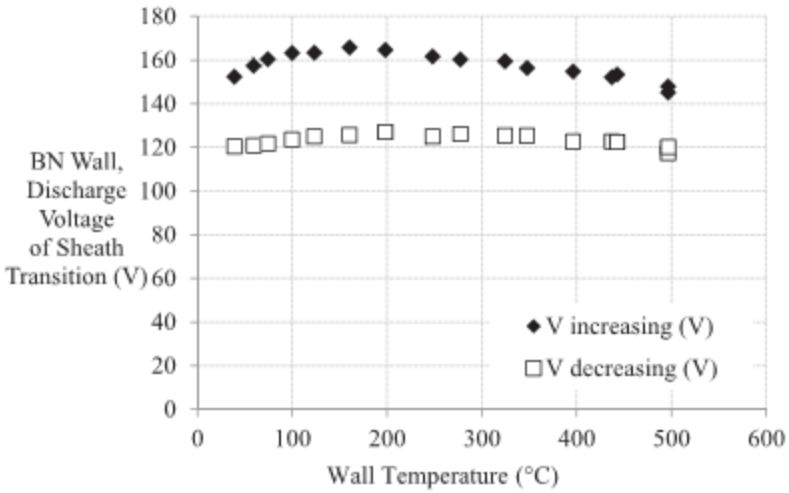

Figure 9. Transition voltages in floating potential of witness probe adjacent to BN sample as a function of wall temperature

2.1.3 Discussion

At low discharge voltages, the wall floating voltage is very close to the discharge voltage (Figure 4). This is due to the considerable prevalence of the energetic electrons in these conditions (**Figure 3**)—in order to satisfy the floating condition, the wall must repel almost all of the energetic electrons to equate their flux with the ion flux and thus must approximately match the discharge voltage. As the discharge voltage/primary electron energy increases, the prevalence decreases, and the wall is able to collect a larger fraction of the energetic electrons, and as such the floating voltage becomes increasingly separated from the discharge voltage.

As the discharge voltage is further increased, a sharp change is observed in wall floating voltage. This change indicates a space-charge sheath collapse, which is not unexpected as the wall had been collecting increased energetic electron energy and flux. The wall temperature is always well below that expected for significant thermionic emission from LaB_6, and the heat flux from the plasma is also low given the order 10^7 cm^{-3} density, so the electron emission mechanism causing the collapse must be SEE rather than thermionic emission. This collapse of the sheath potential allows the energetic electrons to impact the wall with increased energy, no longer slowed by the retarding sheath voltage. This appears to be the root cause of the observed hysteresis—once the sheath potential is collapsed, plasma electrons are able to impact the wall with increased energy and generate a greater secondary electron yield. The effect is to create a feedback mechanism and hysteresis similar to that observed by Takamura *et al.*, so when the plasma electron energy is again decreased, the sheath voltage is not restored until the electron energy is decreased substantially below that required to cause the collapse.

As the heater power is increased, a plasma is generated inside the heater box, and it is observed that the size of the hysteresis loop decreases and disappears. Although electrically isolated in a vacuum, the LaB_6 -coated wall material sample is un-insulated over most of its area facing the interior of the heater, and is thus able to receive plasma flux from both sides if there is plasma within the heater volume. The observed impact on the floating potential agrees with the prediction that a certain prevalence of energetic electrons is required for the hysteresis to occur, reasoning that the energies of the electrons in the plasma interior to the box are likely low and that as their number increases, the effective energetic electron prevalence experienced by the wall material sample decreases.

To more explicitly evaluate the measured floating potentials, the measured potentials of the BN wall are plotted against predictions of the model from Ref. 15. Results are shown in Figure 10. Average experimental values of α = 0.03 and T_e = 3 eV are used in input to the model (imperfect as the experimental value of α changes as the discharge voltage is varied, cf. **Figure 3**), along with SEE data from literature measurements of clean BN. [17] It is observed that the sheath collapses at higher voltages for the roughened BN sample, as it obstructs SEE by geometric obstruction. Adjusting the input SEE yield to the model, it is observed that the transition occurs at about the right voltages when the SEE yield is 70% of the literature value. This view also makes it apparent that the physically observed behavior corresponds to "falling off" the two stable branches of the s-curve solution, accounting for the observed abrupt changes in floating potential and the hysteresis loop.

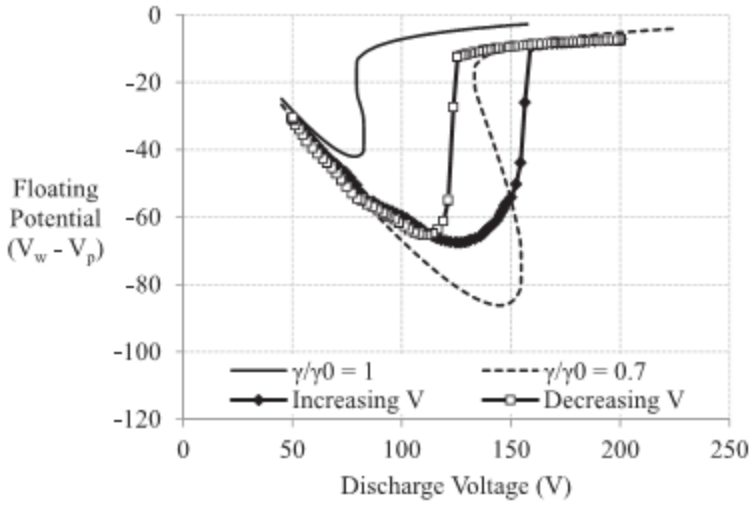

Figure 10. Comparison between observed floating potentials of rough BN wall and model of Ref. 15 using average experimental values of $\propto = n_{ep}/n_e = 0.03$ and $T_e = 3$ eV.

The full description of SEE yield with incident energy is not linear; at much higher energies it begins to decrease with incident energy [18]. Outcomes in those higher energy regimes may be interesting to study and differ from the current experiments, which are firmly within the regime where SEE yield increases with incident energy.

2.1.4 Conclusions

It is confirmed that a hysteresis in the plasma-wall interaction can occur in low-heat-flux plasmas when an energetic electron population is present. The hysteresis is precipitated by modification of the plasma electron energy distribution function (EEDF) by the acceleration of an energetic electron population. Distinct hysteresis curves have been measured experimentally. The effect of non-thermal electron populations as a cause for hysteresis and mode shifts in many devices has not been greatly explored, though non-thermal EEDF's have been identified or are suspected in many of the devices in which mode-shifting behavior is observed. [19,20] The mechanism identified in the current investigation may play a role in explaining observed hysteresis and mode-shifting behavior in plasma devices with dielectric walls and significant SEE in cases where there is significant deviation of the plasma EEDF from a thermal Maxwellian

2.1.5 References

[1] R. Timm and A. Piel, Contrib. Plasma Phys.32, 599 (1992).
[2] S. Takamura, N. Ohno, K. Shiraishi, and S. Masuzaki, J. Nucl. Mater. 196–198, 448 (1992).
[3] M. Ye, S. Masuzaki, K. Shiraishi, S. Takamura, and N. Ohno, Phys. Plasmas3, 281 (1996).
[4] M. Turner and M. Lieberman, Plasma Sources Sci. Technol.8, 313 (1999).
[5] S. Xu, K. Ostrikov, W. Luo, and S. Lee, J. Vac. Sci. Technol. A18, 2185 (2000).
[6] S. Singh, J. Appl. Phys.103, 83303 (2008).
[7] M. J. Sekerak, B. W. Longmier, A. D. Gallimore, D. L. Brown, R. R. Hofer, and J. E. Polk, "Mode Transitions in Hall Effect Thrusters," AIAA Paper No. 2013-4116, 2013.
[8] D. L. Brown, "Investigation of low discharge voltage Hall thruster characteristics and evaluation of loss mechanisms," Ph.D. thesis (University of Michigan, 2009).
[9] G. Hobbs and J. Wesson, Plasma Phys.9, 85 (1967).
[10] M. Campanell, Phys. Plasmas22, 040702 (2015).
[11] J. Sheehan, I. Kaganovich, H. Wang, D. Sydorenko, Y. Raitses, and N. Hershkowitz, Phys. Plasmas21, 063502 (2014).
[12] N. Meyer-Vernet, Astron. Astrophys.105, 98 (1982).
[13] C.-H. Nam, N. Hershkowitz, M. Cho, T. Intrator, and D. Diebold, J. Appl. Phys.63, 5674 (1988).
[14] B. Walch, M. Horanyi, and S. Robertson, Phys. Rev. Lett.75, 838 (1995).
[15] S. Langendorf and M. Walker, Phys. Plasmas22, 033515 (2015).
[16] N. Hershkowitz, J. R. DeKock, P. Coakley, and S. L. Cartier, Rev. Sci. Instrum.51, 64 (1980).

[17] J. P. Bugeat and C. Koppel, in Proceedings of the 23rd International Conference on Electric Propulsion, IEPC(1995), pp. 95–35.
[18] A. Shih, J. Yater, C. Hor, and R. Abrams, Appl. Surf. Sci.111, 251 (1997).
[19] V. Godyak, R. Piejak, and B. Alexandrovich, Plasma Sources Sci. Technol.11, 525 (2002).
[20] D. Sydorenko, A. Smolyakov, I. Kaganovich, and Y. Raitses, Phys. Plasmas13, 014501 (2006).

2.2 George Washington University – Plasma-Wall Multiscale Modeling

2.2.1 Overview

GWU has developed a multiscale model of the magnetized plasma discharge in which a kinetic treatment is used to model electron transport along magnetic field lines while a 2D macroscopic model is employed for the global thruster discharge. This multiscale formulation offers the benefit of self-consistently calculating electron mobilities, while at the same time retaining the reduced computational requirements of a hybrid model. The plasma-wall transition region is modeled kinetically using two models developed, *i.e.* multi-dimensional full kinetic model and one-dimensional full kinetic model. Simulation of plasma-surface interaction in the case of grooves was performed.

2.2.1.1 Summary

GWU effort focused on modeling plasma-material transition region. Development of the simulation capability was performed in close interaction with experimental efforts by Georgia Tech and the University of Alabama. GWU has developed a multiscale model of the magnetized plasma discharge in which a kinetic treatment is used to model electron transport along magnetic field lines while a multi-dimensional macroscopic model is employed for the global thruster discharge. This multiscale formulation offers the benefit of self-consistently calculating electron mobilities, while at the same time retaining the reduced computational requirements of a hybrid model. The plasma-wall transition region is modeled kinetically using the two models developed, *i.e.* the multi-dimensional full kinetic model and the one-dimensional full kinetic model. Simulations of plasma-surface interaction in the case of various wall materials and smooth surfaces and grooves were performed. Using different materials, the effect of secondary electron emission on the sheath was characterized.

General model prediction consistent with experimental data is that higher SEE yield leads to lower potential drop over the sheath. At lower energy values, the effects of backscatter highly affect the SEE yield, which is greatly affected by surface roughness. In order to demonstrate the effects that different shapes and sizes of erosion profiles have on SEE, one study pre-eroded materials to specific shapes of grooves. The results show that with grooves, the SEE yield is lower, and when considering the effect of second generation secondaries the yield slightly increase. Note that these second-generation secondaries have much lower energy than the first generation secondaries so they will have a much lower SEE yield. In the kinetic simulation of the grooves following assumptions and conditions were implemented. In particular, one can see that negative charge formation in grooves leads to potential distortion near the plasma-surface interface. This is in agreement with experimental observations.

Two types of the sheath appear near the plate depending on the voltage and thermo-emission electron current values. The first type of sheath has a large potential drop and its structure is set by the electron and ion currents from the plasma. The second type of the plate sheath appears when the energetic part of EEDF on the plate becomes reach enough to produce a large number of secondary electrons. In this case, the potential drop on the sheath is smaller and set by a balance of the electron current from plasma and the secondary electron emission current from the plate. The ion current from the plasma plays a minor role. The calculation results and the experimental date are in a good agreement. GWU has also performed a simulation of the GT HPEPL experiments on plasma sheaths with nonlocal fast electron populations, and the kinetic simulation results obtained agree fairly well with the experimental results, validating the simulation's capability in this area.

It was demonstrated that plasma-material interface could be controlled by a magnetic field incidence angle. In particular, it was found that the increase of a magnetic field angle leads to sheath thickness decrease. Both experimental measurements and simulations agree that larger incidence angle (about 70 degrees) might lead to the collapse of the sheath and decrease of ion flux to the wall reducing wall erosion.

2.2.1.2 Background

Although a fully-kinetic approach, where all species including electrons are treated kinetically, could resolve electron and wall effects directly, such an approach is not numerically effective. Fully-kinetic models are prohibitively slow and resource intensive since details on the spatial scale of electrons must be resolved. The simulation must also progress at prohibitively small time steps in order to resolve electron frequencies. Even with the use of supercomputers, these approaches are applicable only to the smallest (low power) HETs. Thus, the fully-kinetic approaches serve as an important research tool, however, do not offer much practical use to the EP design community.

Recently, progress has been made on tackling these difficulties by considering a multiscale approach to modeling HETs. This approach was developed over last few years at the GWU. Existing HET codes attempt to resolve the

electron and wall effects by either simulating the entire thruster kinetically at prohibitive computational expense or alternately replace the self-consistent behavior with non-predictive model fits. The multiscale approach retains the positive feature of both approaches, resulting in self-consistent modeling of kinetic effects while at the same time requiring only the computational resources available in a standard workstation. To accomplish this, GWU decomposes the HET analysis into three spatial scales. Each scale concentrates on a different subset of physics. The difficulty with fully kinetic codes is that they require large computational resources in order to describe the global thruster discharge. We instead apply the kinetic model only to a single magnetic field line. The magnetic field line serves as the first spatial scale, as shown in **Error! Reference source not found.**a). On this spatial scale, the dynamics are dominated by the microscopic cyclotron motion of electrons and their interaction with heavy particles and thruster walls. From the frame of reference of electrons on the temporal scales required to compute transport properties, heavy particle densities and cross-field properties can be assumed to remain frozen. The simulation thus concentrates only on kinetically resolving the electron motion along the walls, and self-consistently calculating electron transport and velocity distribution evolution. Collisions are included and mobility is computed by considering the drift speed of the particle guiding center. Since the simulation is limited to a single magnetic field line, the computation is fast and hundreds of electron orbits can be computed in a matter of minutes. Utilizing the multiple core architecture present in all modern CPUs, multiple magnetic field lines are analyzed in parallel.

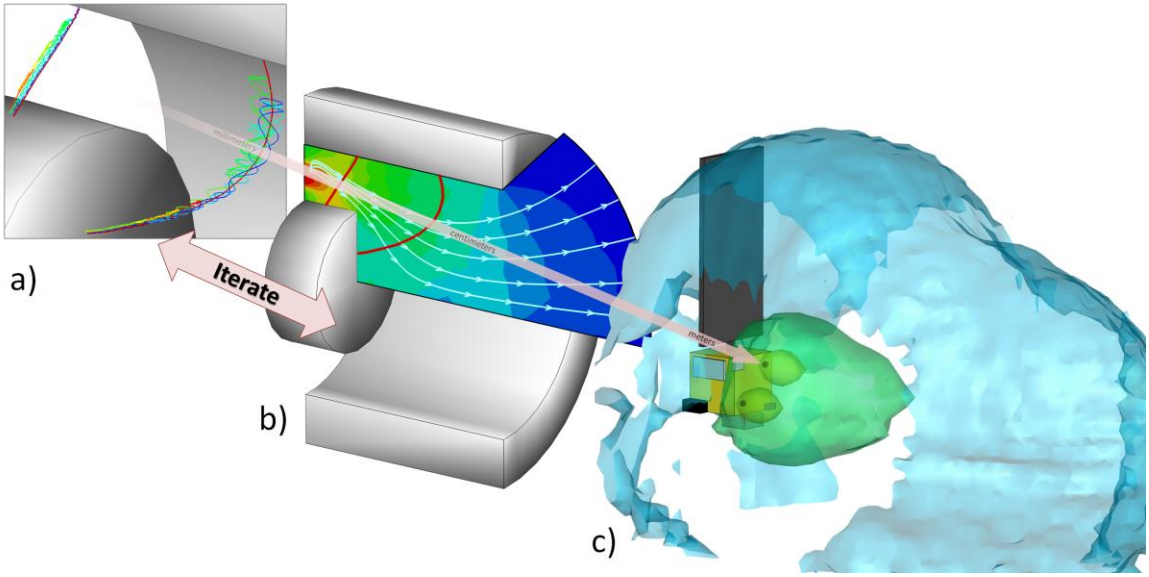

Figure 11. Schematic of the multiscale approach. A kinetic model of the microscopic electron motion about magnetic field lines (a) is used to self-consistently calculate electron mobility. This mobility is then used in a hybrid 2D axial code for thruster discharge (b). Upon reaching steady state, ions exiting the thruster are sampled to obtain a source model for plume analysis (c).

Since this electron kinetic simulation models only a single magnetic field line, information needs to be provided to the code on the global (axial) state of the thruster. This includes the electric field component normal to the field line, as well as the heavy particle densities, bulk electron temperature, and magnetic field gradients. This information is provided by a 2D axial hybrid code. This 2D code forms the second domain in our multiscale model. It is illustrated in **Error! Reference source not found.**b). Ion and neutral density are obtained by simulating kinetic particles. A computational mesh aligned with magnetic field lines is used internally in the code to compute electron properties. In our approach, the spatial variation in mobility is calculated self-consistently by the kinetic code.

The microscopic and macroscopic models described above depend on each other. In order to obtain a truly self-consistent solution, the two codes must be iterated until convergence. Alternatively, the 1D kinetic code can serve as a subroutine in the 2D code used to update the global mobility map. Once a converged solution has been reached, ion particles leaving the thruster can be sampled to obtain a discretized velocity distribution function for the beam.

In summary, we have developed a multiscale model of the HET discharge in which kinetic treatment will be used to model electron transport along magnetic field lines, while 2D macroscopic model will be employed for the global thruster discharge. This multiscale formulation offers the benefit of self-consistently calculating electron mobilities, while at the same time retaining the reduced computational requirements of a hybrid model. Initial coupling of the

microscopic and macroscopic model will be performed via axial electric field, electron fluxes to the wall and electron cross-field transport.

2.2.2 Effect of wall material and wall roughness on the plasma-wall transition region

This section describes an experimental and simulation study of the near-wall properties of different material samples immersed in a plasma for the purposes of studying the sheath is electric propulsion devices. The samples consist of alumina, HP-grade boron nitride, and quartz. Using different materials the effect of secondary electron emission on the sheath can be characterized. Also examined are the effects of changing the bias voltage.

Figure 12 shows the experimental values from the Georgia Tech experiment described earlier. They are used to experimentally show the sheath potential change between a BN and Alumina wall. Although the two sets of data are not from exactly the same set up (BN is at 87 V bias and Alumina is at 90 V), they are marginally similar and suffice for these purposes.

This experimental data shows as predicted; that since alumina has a higher SEE yield its potential drop will be smaller. Note that we can see the beginnings of a breakdown in the classic sheath profile in the alumina case due to the high SEE yield.

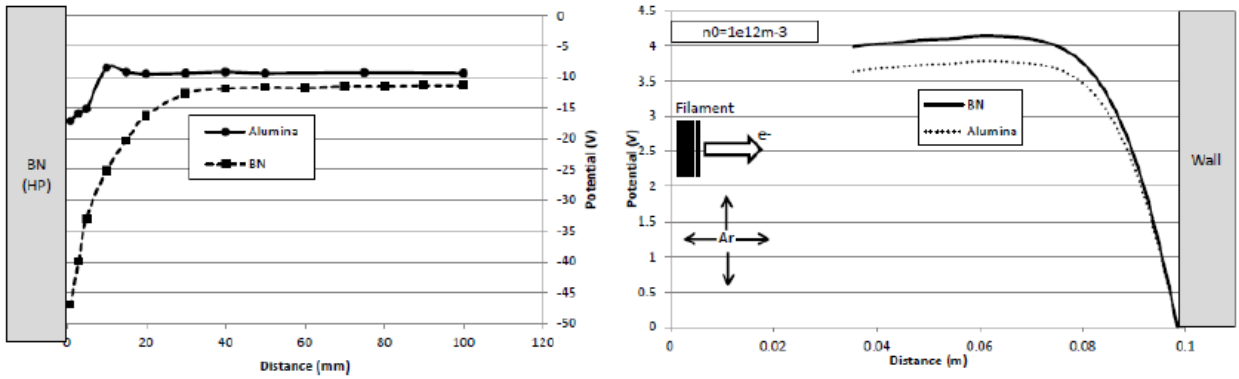

(a) (b)

Figure 12. Measured (a) and Calculated (b) potential profiles near the wall for different wall materials (BN and Alumina)

Effect of Wall Roughness

At lower energy values the effects of backscatter significantly affect the SEE yield that is greatly affected by surface roughness. SEE yield can be greater than one for a smooth surface or less than one for a rough surface. This implies that a rough surface creates less of a yield, a widely accepted theory. The lower SEE yield is due to the fact that as a secondary electron escapes it is likely to hit another spot on the wall and will not escape to the actual plasma. However, a concurrent mechanism can counter this reduction. SEE yield is a function of particle energy and angle of incidence. The incidence angle is measured to the normal of the smooth surface. For a rough surface, the angle that the electron hits is larger than it would be if the surface was smooth. This increased angle will increase the yield, but in general, it is assumed that a rough wall will increase SEE yield. **Figure 13** shows the profiles considered in this study.

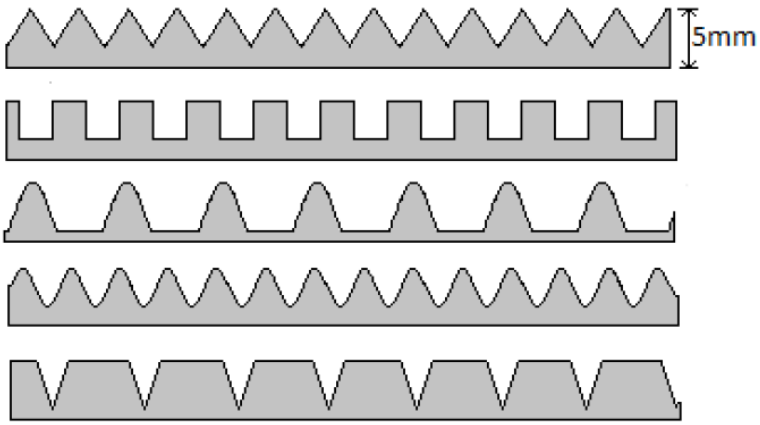

Figure 13. Various profiles used in the computational model.

Impact of Surface Profiles

In **Figure 14**, the top of the imperfections was increased to help visualize sheath size change as the imperfection size changes. It can be seen that the only change in the size of the sheath is due to the raised tip of imperfection. Since there is no secondary electron emission in this simulation it can be assumed that the size of the imperfection itself does not affect the sheath profile.

This study showed that some secondary electrons that escape will hit another portion of the wall. It is also possible that this bombardment could create what this paper called "second generation" secondaries. Figure 5 demonstrates this phenomenon. It shows the triangle and rectangular grooves used in that study.

The results from this study, as seen in **Figure 15** and **Figure 16**, show that with grooves the SEE yield is lower, and when considering the effect of secondary generation secondaries the yield slightly increase. It should be noted that these second generation secondaries have much lower energy than the first generation secondaries so they will have a much lower SEE yield.

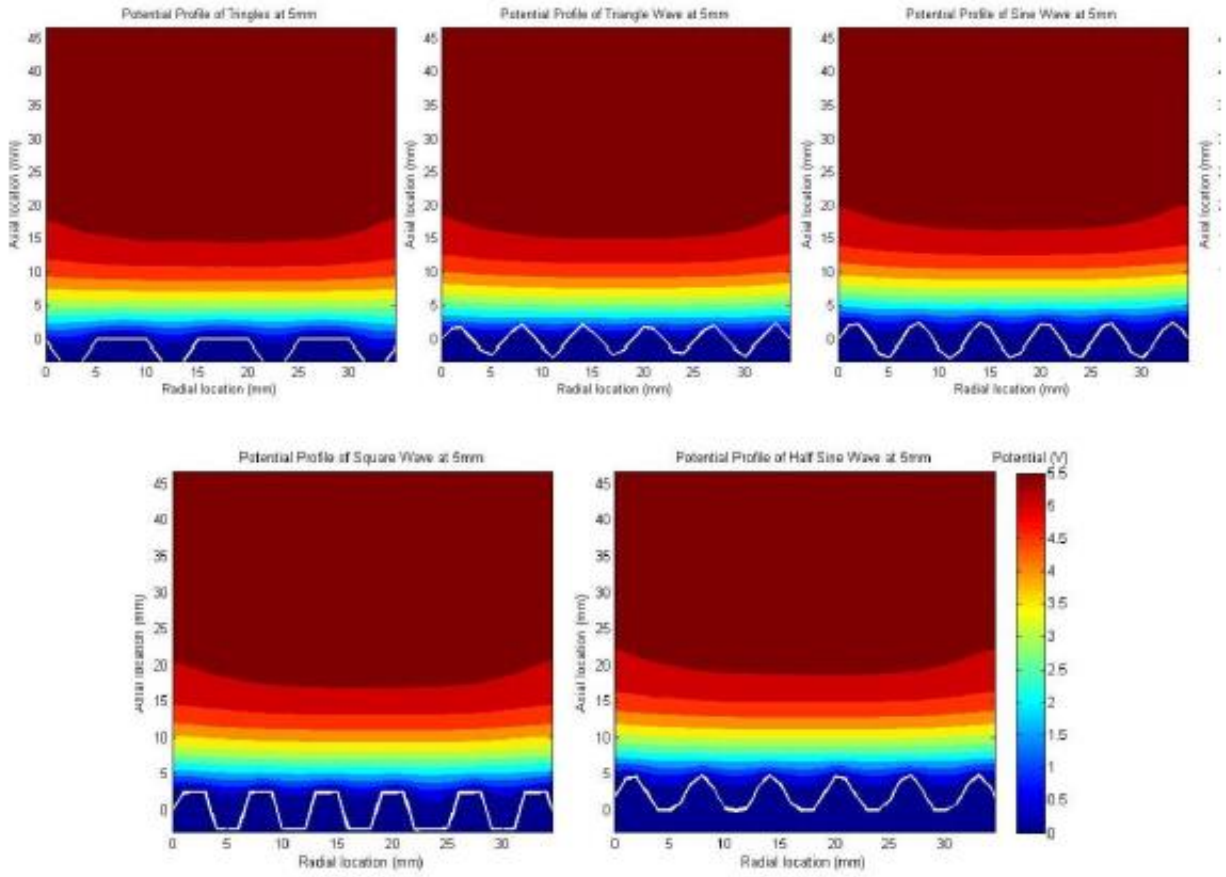

Figure 14. Calculated potential profiles for various surface roughness conditions.

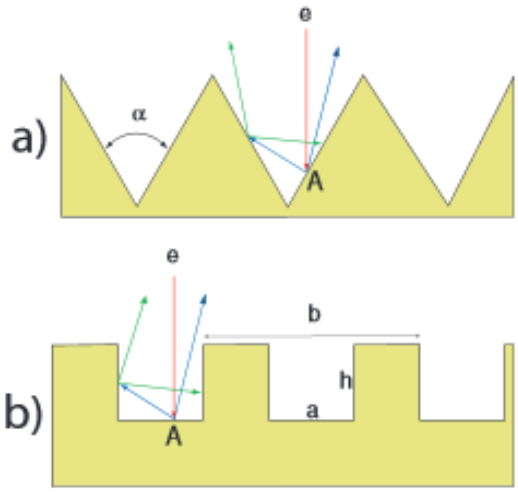

Figure 15. Several scenarios for possible SEE trapping in the cavities

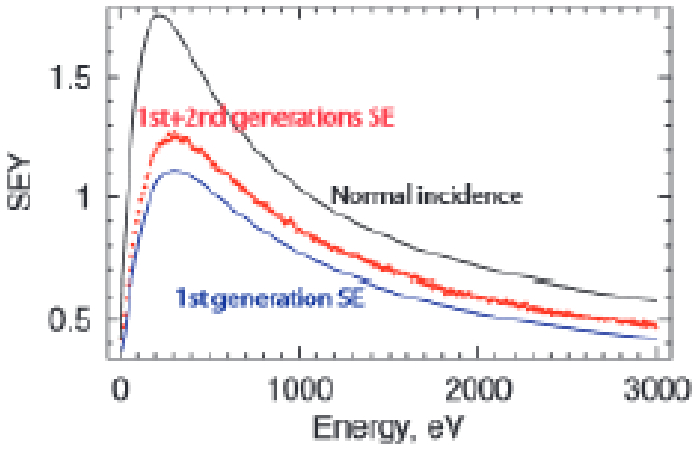

Figure 16. SEE yield as a function of electron energy with rough surface example yield

2.2.2.1 Kinetic simulations of sheath formation

For self-consistent simulation of discharge plasma maintained by a beam of energetic electrons at low gas pressure with an oblique magnetic field, we have developed a fully kinetic model of plasma with elastic/inelastic collisions for electrons and ions. The secondary electron emission from the emissive floating wall made from different materials (BN, Al_2O_3, SiO_2) is included in our kinetic model and computed with using the energy distribution function of electrons (EEDF) arriving at the surface. This full-scale modeling with a particle in cell Monte Carlo collision (PIC MCC) method allowed us to calculate all plasma parameters, as well as instability and structure features without introducing fitting and unknown parameters usual for simplified approaches.

Below in Sec. I we describe 2D PIC MCC model (with cylindrical symmetry). The results of 2D PIC MCC simulations of plasma interaction with emissive electrically isolated wall in given in Sec. II for the experimental conditions of Georgia Tech; In Sec. III b) formation of the sheath over the grooved surface in described and in Sec. IV, the results on sheath modification over the emissive wall with an increase of angle of oblique magnetic field is presented.

2.2.3 2D PIC MCC model of discharge plasma with a beam of energetic electrons in an oblique magnetic field.

We have developed a model of discharge plasma for the experimental setup of GTECH and performed fully self-consistent kinetic simulations with Particle-In-Cell Monte Carlo Collisions method. The sheath formation over the floating emissive plate was studied for different cathode voltages. The cathode voltage sets the electron beam energy. In our kinetic model, the plasma was described by the system of equations that includes the Boltzmann equations for electrons and ions distribution functions, Poisson's equation for electrical potential and the currents balance equation for the floating potential of the emissive plate. The model is two-dimensional in space and three-dimensional in terms of electron and ion velocity (2D3V). The distribution functions for electrons $f_e(\boldsymbol{r},\boldsymbol{v})$ and ions $f_i(\boldsymbol{r},\boldsymbol{v})$ are found from the Boltzmann equations:

$$\frac{\partial f_e}{\partial t} + \vec{v}_e \frac{\partial f_e}{\partial \vec{r}} - \frac{e(\vec{E} + \vec{v}_e \vec{B})}{m} \frac{\partial f_e}{\partial \vec{v}_e} = J_e, \quad n_e = \int f_e d\vec{v}_e \tag{1}$$

$$\frac{\partial f_i}{\partial t} + \vec{v}_i \frac{\partial f_i}{\partial \vec{r}} + \frac{e\vec{E}}{M} \frac{\partial f_i}{\partial \vec{v}_i} = J_i, \quad n_i = \int f_i d\vec{v}_i \tag{2}$$

Where v_e, v_i, n_e, n_i, m, and M are the electron and ion velocities, concentrations, and masses, respectively; J_e and J_i are the collisional integrals for electrons and ions with background atoms. Knowing the distribution functions for electrons and ions, we can calculate the mean energy of species, their concentrations, and elastic and non-elastic collisional rates. The zero-current balance equation into the surface of floating emissive plate:

$$j_{ep} + j_{be} + j_{esr} = j_{es} + j_i \tag{3}$$

where j_{pe} is the current of plasma electrons, j_{be} is the current of beam electrons from plasma, j_i is the ion current, j_{es} is the current of secondary electrons emitted from the plate surface and j_{esr} is the current of secondary electrons, returning back to the surface. The floating potential of the emissive plate is calculated self-consistently from the condition of a zero total current into the plate surface. Poisson's equation describes the electric potential distribution:

$$\Delta\phi = 4\pi e(n_e - n_i), \quad E = -\frac{\partial\phi}{\partial\vec{r}}. \tag{4}$$

The discharge operates in argon. The kinetics of electrons includes elastic scattering of electrons on background atoms, excitation of metastable states, and ionization. For ions, we take into account the elastic and resonant charge exchange collisions. In both the model and the experiment the plate is made from Al_2O_3, hBN, and SiO_2. These materials have large secondary emission coefficient due to the electron bombardment, which increases with the energy of an incident electrons. The secondary electron emission is calculated by accounting for the energy distribution functions of the electrons approaching the plate surface.

2.2.4 2D PIC MCC simulations of plasma interaction with emissive electrically isolated wall for the experimental conditions of GTECH

In particle-in-cell Monte Carlo collision simulations and in the experiment we study sheath formation over an emissive floating Al_2O_3 plate in a direct current discharge plasma at argon gas pressure 10^{-4} Torr. The discharge glow is maintained by the beam electrons emitted from a negatively biased hot cathode. In **Figure 17**, the electron density distribution is shown for the Georgia Tech experimental conditions. We observe **three types** of sheaths near the floating emissive plate and the transition between them is driven by changing the negative bias. In **Figure 18**, the change of potential drop over the emissive plate is shown. The comparison of computed and experimental data is shown in **Figure 19**. In **Figure 20**, the EEDF is shown for j equals 20 mA and for different voltages. The total evolution of the potential drop over the emissive plate and electron temperature is shown in |**Figure 21** and **Figure 22** for different voltages. The Debye sheath appears at lower voltages when secondary electron emission is negligible. The current balance is set by beam electron and ion current from the plasma.

With increasing applied voltage, secondary electron emission switches on and the first transition to a new sheath type, beam electron emission (BEE), takes place. In this case, the current balance is set by beam electron current from plasma, secondary electrons from plate, back-scattered secondary electrons and ion current. In this regime, the potential drop over the plate $\Delta\varphi$ is about four times larger than the temperature of plasma electrons. The virtual cathode appears near the emissive plate and its modification helps to maintain the BEE regime within some voltage range. Further increase of the applied voltage U initiates the second smooth transition to the plasma electron emission sheath regime and the ratio $\Delta\varphi/T_e$ tends to unity with increasing U. The current balance is set by beam and cold electron currents from plasma and secondary electrons from the plate.

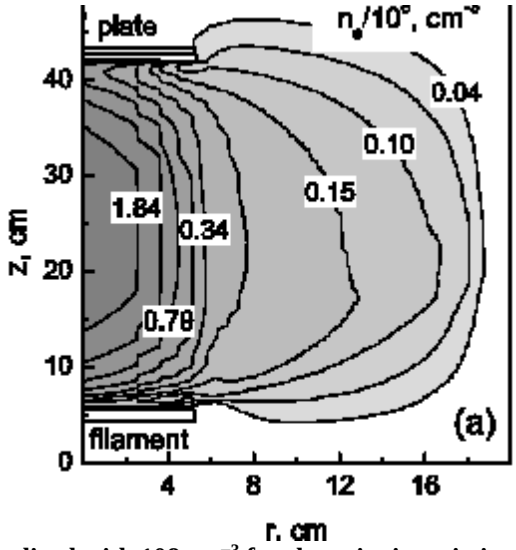

Figure 17. Electron density normalized with 108 cm^{-3} for thermionic emission current j = 30 mA and the applied voltage U = −70 V. The axis of symmetry of the cylindrical chamber is at r = 0.

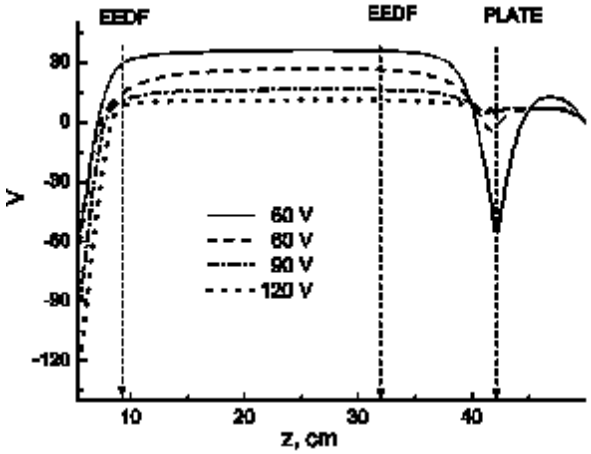

Figure 18. Potential profiles over the axis of symmetry for the applied voltage of −55 V, −60 V, −90 V and −120 V and for thermionic emission current j = 20 mA. The cathode is at z = 5.6 cm and the plate is at z = 42 cm. Vertical arrows show the place of calculation of the EEDF.

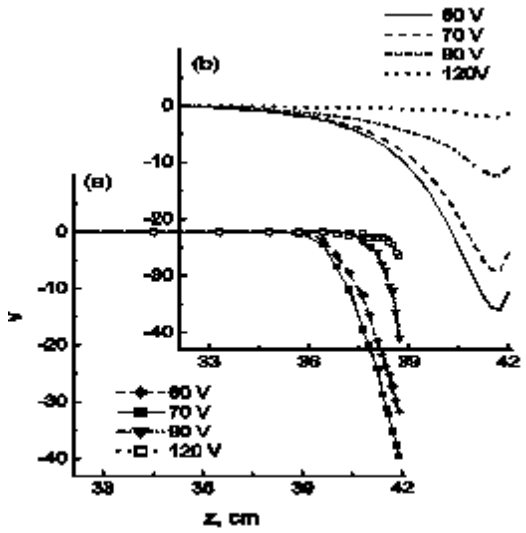

Figure 19. Measured (*a*) and calculated (*b*) potential distribution near the emissive plate for *U* = −60 V, −70 V, −90 V and −120 V at *j* = 10 mA.

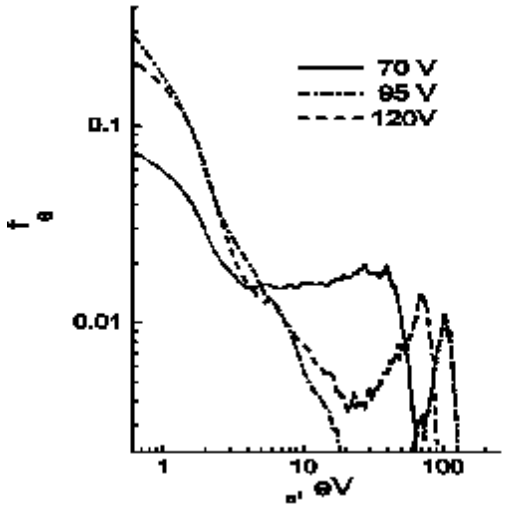

Figure 20. Energy distribution function for electrons approaching the plate surface for *U* = −70 V (solid line), −95 V (dashed line) and −120 V (dashed–dotted line) for *j* = 20 mA.

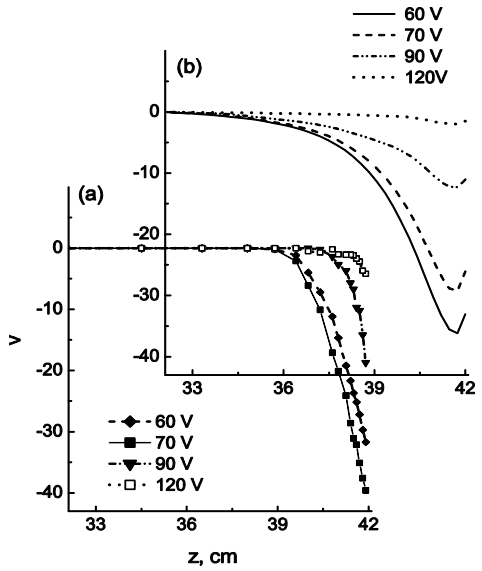

Figure 21. (*a*) Potential drop over the plate sheath φ_s relative to the plasma potential for *j* = 20 mA (squares) and *j* = 40 mA (stars), and (*b*) the virtual cathode dip φ_d relative to the plate surface for *j* = 20 mA. Debye sheath regime (D), electron beam emission (BEE) and plasma electron emission (PEE) regimes are shown.

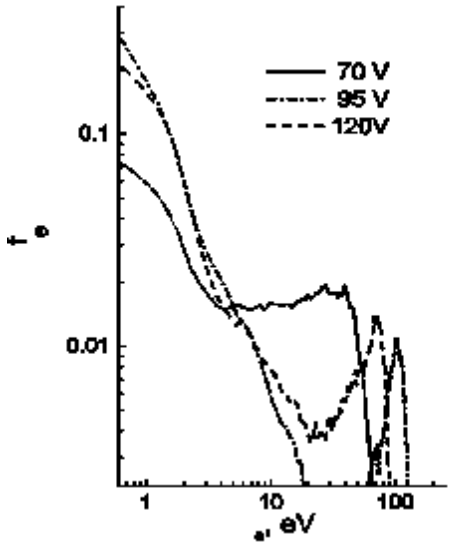

Figure 22. Mean electron temperature of plasma electrons in the center of discharge as a function of negative bias on the cathode for *j* = 20 mA (stars) and 40 mA (squares). The open symbols are from simulations and closed symbols are from the experiment.

We analyzed also the oscillatory behavior of the emissive sheath. **Figure 23**(*a*) illustrates the potential distribution at different times for *j* = 10 mA and *U* = −120 V. A fragment of oscillating floating potential is shown in **Figure 23**(*b*). The numbers in **Figure 23**(*b*) point out the time of snapshots of the potential and electron density profiles shown in **Figure 23**(*a*) and **Figure 24**. A plasmoid of slow electrons is formed near the plate and transported to the bulk plasma periodically with a frequency of about 25 kHz.

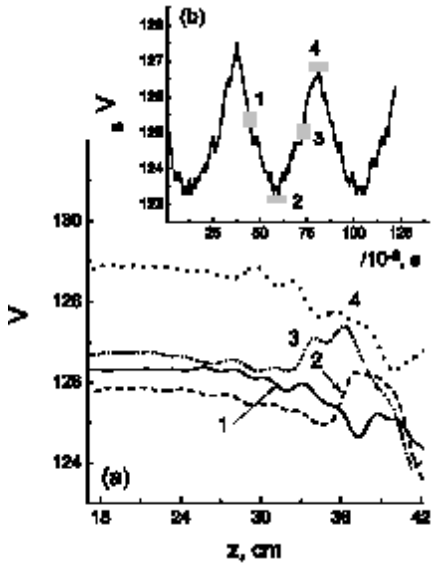

Figure 23. Electrical potential profiles at different time moments (*a*) and fragment of floating plate potential oscillations with time (*b*) for j = 10 mA, U = −120 V.

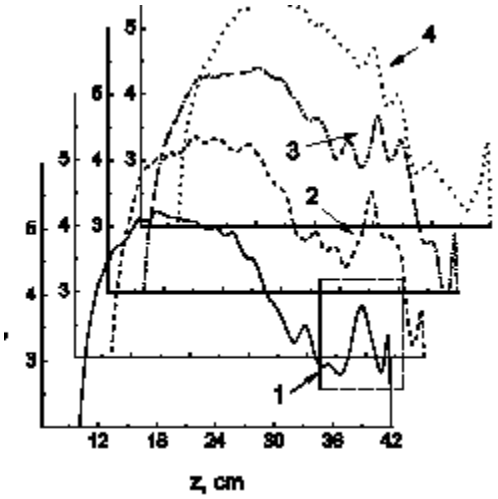

Figure 24. Electron density profiles at different time moments of oscillating floating potential shown in figure 12(*b*) for j = 10 mA, U = −120 V.

2.2.5 2D PIC MCC simulations of formation of sheath over the grooved emissive surface

For the Georgia Tech experiment with an emissive plate with grooves made from hBN, it is important to provide more accurate resolution of the area near and inside of grooves. To fulfill this requirement we use plasma parameters from previous full-scale PIC MCC simulations of plasma with a plane plate (see Sec. I). We simulated the plasma only around a grooved plate and the calculation domain was 7 cm by 5 cm. The plate with a diameter of 55 mm has four, 5 mm × 5 mm grooves on the surface. In **Figure 25**, two grooves instead of four are shown because $x = 0$ is the plane of symmetry of Cartesian coordinates.

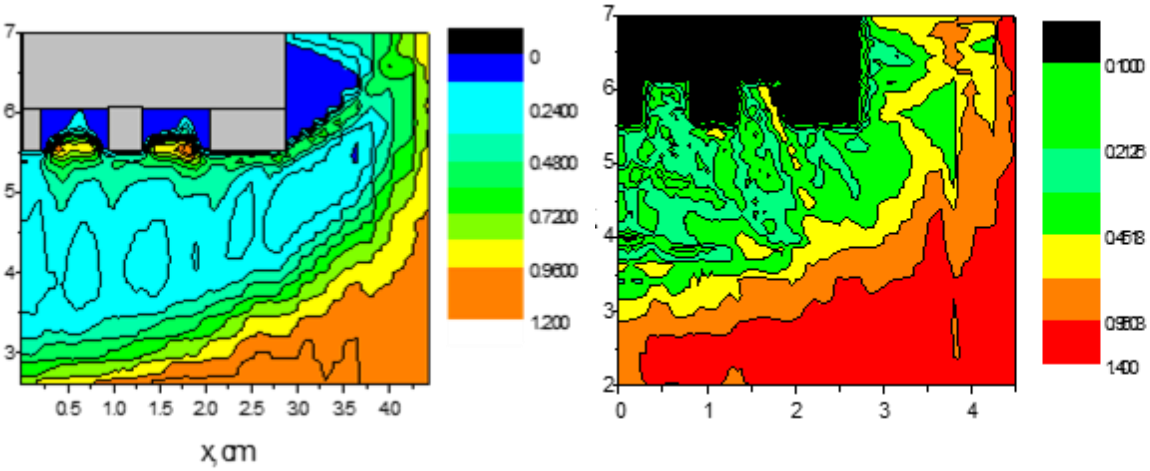

Figure 25. Electron (left) and ion (right) density distribution measured in 10^8 cm $^{-3}$ over emissive grooved surface.

For this case, the boundary conditions for the equations (1) - (4) refer to a domain imbedded in unlimited quasi-neutral plasma with Maxwellian electrons and ions with the temperatures T_e = 3 eV and T_i = 0.026 eV, respectively. Additionally, a mono-energetic electron beam enters the calculation domain from the bottom boundary. So the electron component of plasma consists of a Maxwellian part and beam electrons. The electron and ion fluxes at the boundaries are constant. Since the boundary conditions for the electrical potential refers to the quasi-neutral plasma, the potential f is $df/dz = 0$ at $z = 0$ and $z = z_{max}$, $df/dx = 0$ at $x = x_{max}$. The floating potential fs is calculated separately inside of a groove for side walls and the bottom taking into account the fluxes of electrons and ions from the plasma and the secondary electrons.

We solve the equations (1) - (4) self-consistently with PIC MCC method using PlasmaNov code developed by Schweigert V and Schweigert I. **Figure 17**, **Figure 18**, and **Figure 19** show the plasma parameters for the electron beam energy is 70 eV, the plasma density in the quasi-neutral region is 2 x 10^8 cm^{-3}.

Figure 25 shows them measured electron and ion number densities over the grooved surface in units of 10^8 cm^{-3}. The numbers 1, 2, 3, 4 in **Figure 25** denote separated areas for the floating potential calculation. The fluxes of electrons from plasma, secondary electrons, and ions approaching the plate surface are calculated to find *fs* (1), *fs* (2), *fs* (3), *fs* (4). The electrical potential distortion over the grooves is determined by the features of charge distributions. The accumulation of secondary electrons takes place near the groove entrance, whereas the electron density is much lower within the sheath. This suggests that either the grooves or the accumulated secondary electrons can potentially draw electrons from the surrounding sheath.

Figure 26 shows the measured potential distribution (Volts) and net charge $(n_e\text{-}n_i)/10^7$ cm^{-3} over the emissive grooved surface. The potential distribution shows that the grooves create areas of substantially lower potential than anywhere else on the surface of the sample.

Figure 19 shows the potential distribution from PIC simulation and the potential distribution from the experiment. The simulation results are in good agreement with the experimental measurements. The potential structure at the entrance to the grooves presented in Figure 25 and Figure 26 is similar to the experimentally measured potential structure at the entrance to the grooves in Figure 27b.

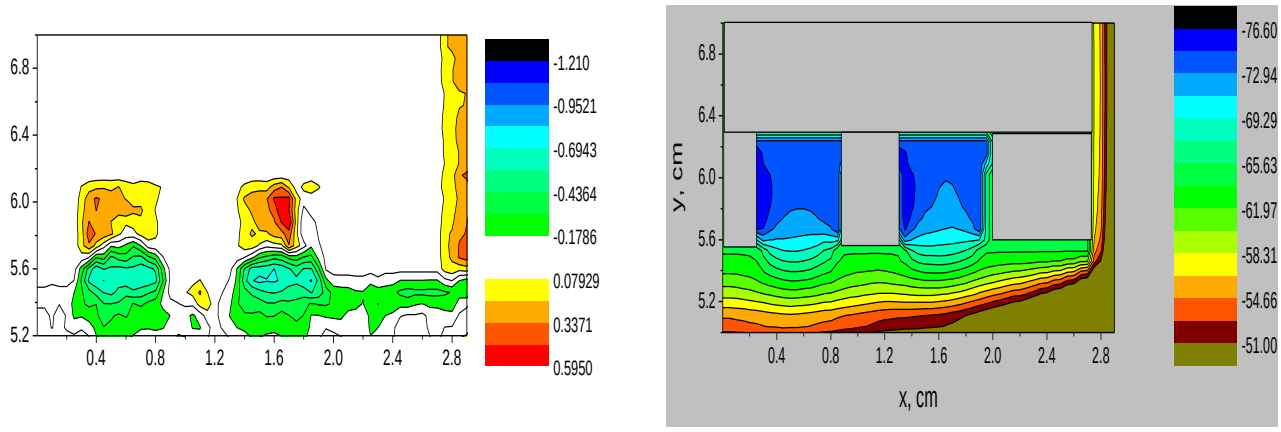

Figure 26. Distribution of charge (n_e-n_i) measured in 10^7 cm^{-3} (left) and potential in Volts (right) and over the emissive grooved surface.

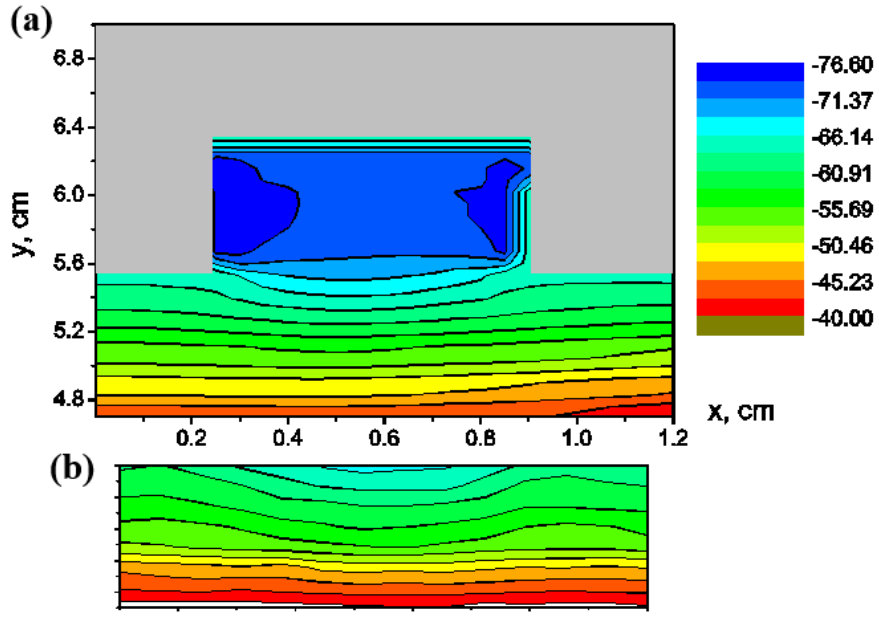

Figure 27. Potential (V) over a groove from PIC MCC simulation (a) and measured in the experiment (b).

2.2.6 2D PIC MCC simulations of sheath modification over the emissive wall with an increase of angle of oblique magnetic field

The interaction of plasma with the emissive wall in the external oblique magnetic field was studied in kinetic simulation and experiment. We consider the case of comparably weak magnetic field when the electron Larmor radius is of the order of magnitude of Debye length and much smaller than the chamber characteristic size. The ion Larmor radius is larger than the characteristic size of the plasma chamber.

The plasma is sustained in the chamber with a height of 10 cm, and radius of 4 cm at the gas pressure of 0.0001 Torr. The voltage applied to cathode U = - 90 V, the anode and side wall is grounded. The plate maintained with some distance from side wall is electrically isolated. The geometry can be seen in **Figure 28**. The axis of symmetry is at r = 0. The ionization rate is chosen to provide the plasma density about 10^8 cm^{-3}. The magnetic field B = 50 G - 150 G and an angle α_B between the normal to the plate and the magnetic field vector changes from 0 to 75 grad.

Solving equations (1) – (4), we study the sheath modification near the wall depending on the magnetic field angle. In Figure 28, the distribution of radial electric field near the plate is shown for the case α_B = 0.

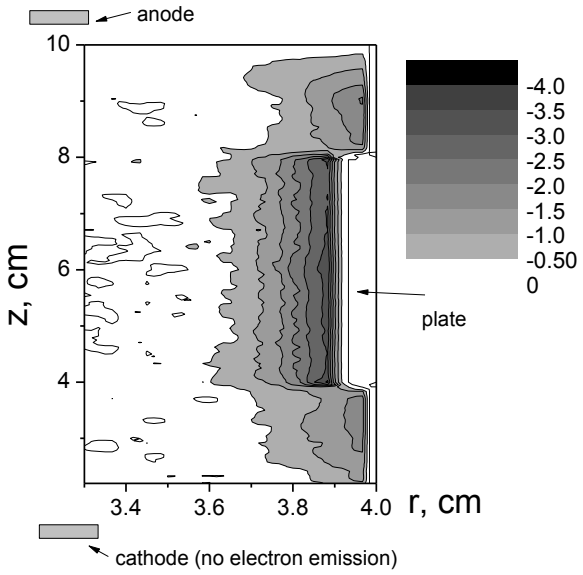

Figure 28. Computed radial component of electrical field measured in V/cm over the plate, B = 50 G, α_B = 0.

By changing the magnetic field angle, we achieved a variation in the potential drop over the plate and the electron current. **Figure 29** shows the potential profile, electron current, and electron temperature as a function of r for α_B 0 and α_B = 75 grad. The mean electron temperature T_e is about 1.5 eV, therefore, a small change of the potential drop leads to a visible increase of electron current to the plate. The experimental and computed data agree qualitatively.

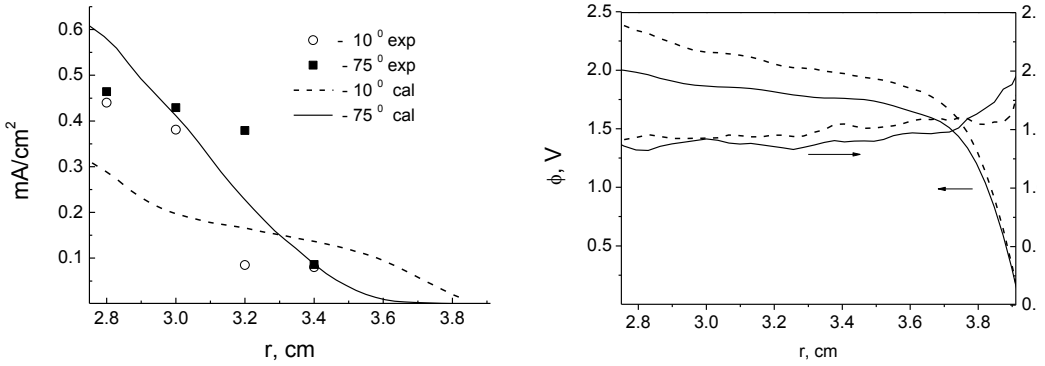

Figure 29. Potential profile (left), electron current and electron temperature (right) for α_B = 10 grad (dashed line) and α_B = 75 grad (solid line). Symbols are experimental data.

In the kinetic simulation, we found that the plasma density has a non-monotonic distribution. In **Figure 30**, the electron density distribution is shown for different α_B.

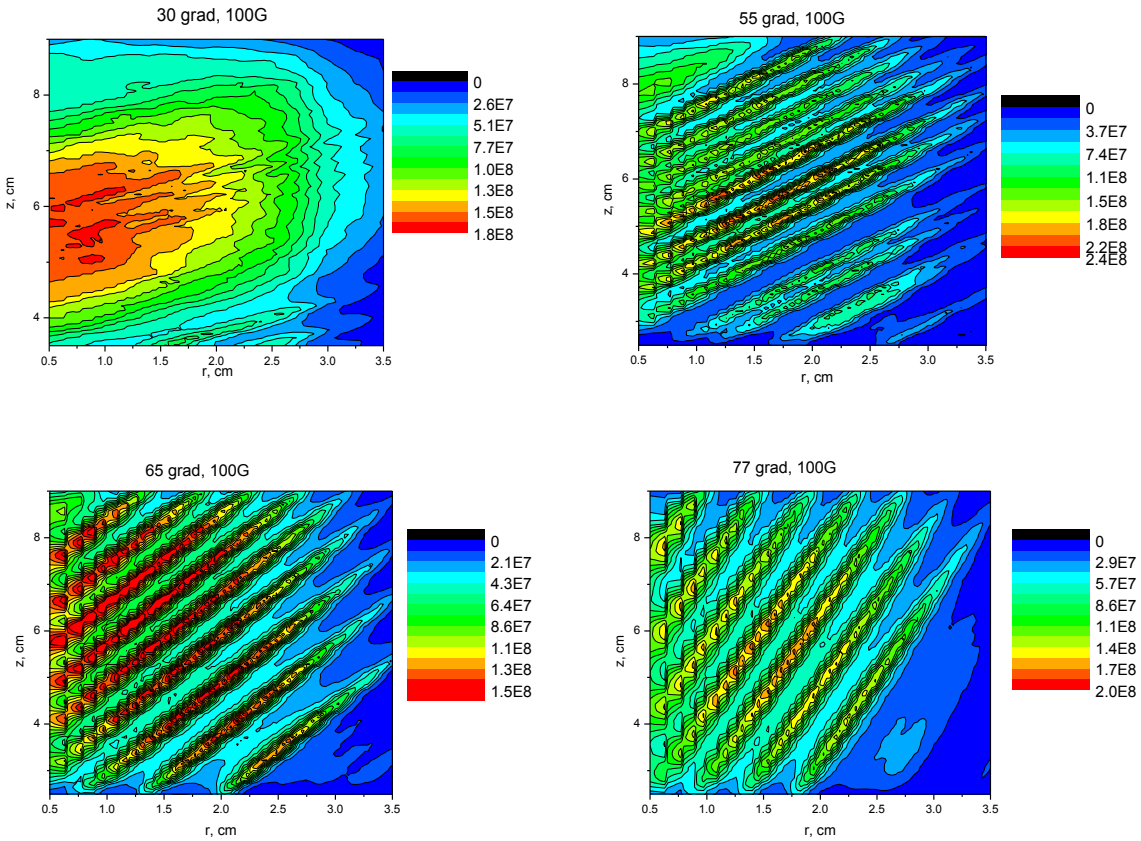

Figure 30. Electron density distribution (cm^{-3}) for α_B =30, 55, 65, 75 grad and B = 100 G.

The electron current flows over the maxima of electron density along magnetic field vector. The plasma is organized in multiple double layers in the direction of normal to the magnetic field. Figure 31 shows the charge distribution and the related multiple double layer structure.

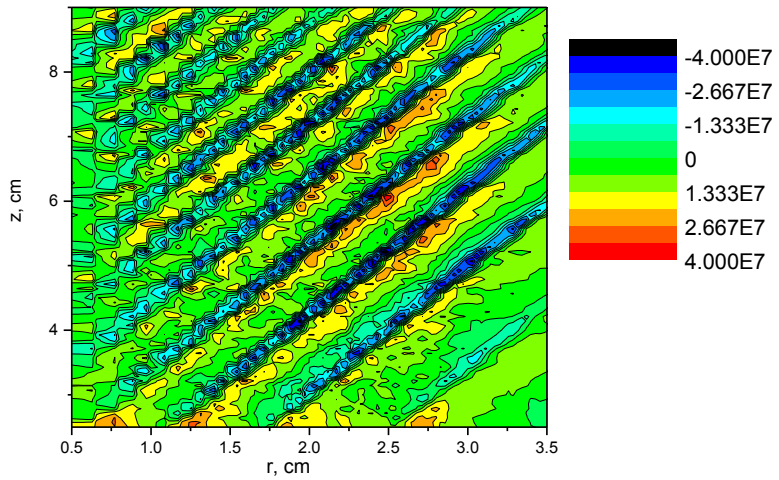

Figure 31. Charge (n_e-n_i) distribution for B = 100 G and for α_B = 75 grad.

In GWU experiment devoted to the sheath study in the oblique magnetic field, an unexpected behavior of the electron current j_e over the dielectric plate was observed. With a variation of magnetic field angle, a quick increase of j_e was observed at certain α_B. The measurements were done with the set of probes shown in the photo in **Figure 32**. The probes are situated equidistantly on the distance 2, 4, 6, 8, 10 mm from the surface. The electron current was measured simultaneously for every value of α_B over the plate.

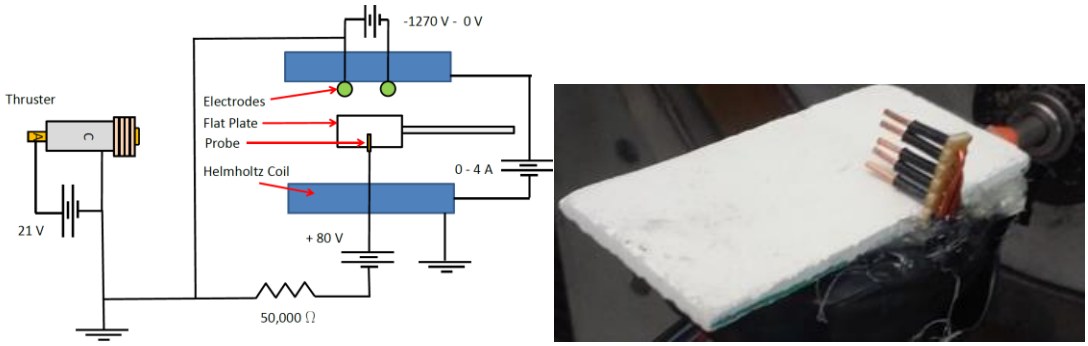

Figure 32. Experimental setup for magnetic field (left) and BN plate with electron saturation current collection probes.

Figure 33 shows the measured electron current for different α_B and for distances 6, 8, 10 mm from the surface. It is seen that the electron current peaks refer to α_B = 35 grad and α_B =6 5 grad for the distance 6 mm and 8 mm. **Figure 33** presents a simple geometrical reconstruction that illustrates the calculation inter-channel distance from the experiment data. These peaks of electron current measured in the experiment indicate the occurrence of the channels of enhanced electron current in plasma in crossed ***E***x***B*** fields in the case of weak electrical fields. The inter-channel distance of current in simulation and experiment is 0.37 cm for B = 100 G.

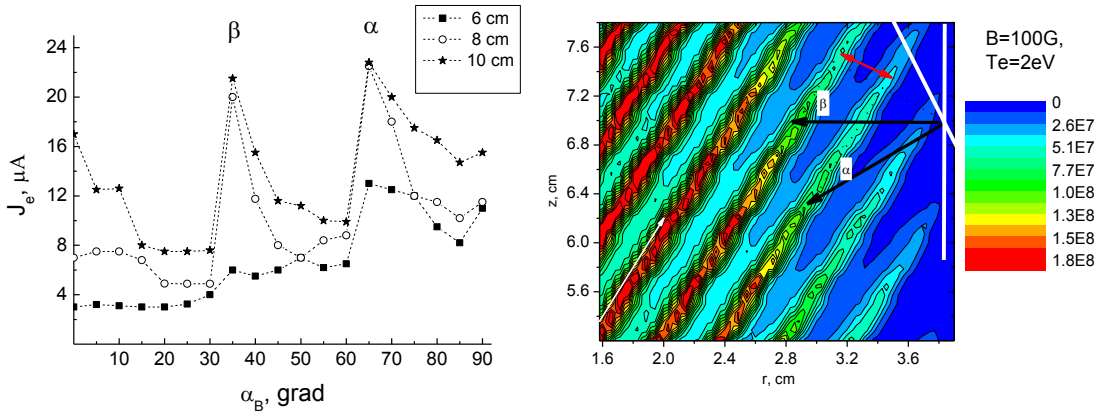

Figure 33. Measured electron current (left) and reconstruction of inter-channel distance from computed electron density for B = 100 G and for α_B = 65 grad.

The electron and ion current flows are associated with the periodic structure in the variation of the plasma density. The distance between plasma density maxima depends on the electron mean temperature T_e, plasma density and weakly on B (for our range of B). The width of the peaks is set by the electron Larmor radius. This periodical structure is a result of the interplay of electrostatic and Lorentz forces. After an ionization event, an electron and ion pair appears. The electron starts gyro motion in a magnetic field. Since in a weak magnetic field, the Lorentz force disturbs the electron trajectories the effect of polarization in quasi-neutral plasma takes place. The periodic structure forms only in the area of quasi-neutrality, where the force of the electric field is comparable to the Lorentz force. The

electrons are accelerated along magnetic field lines, because of non-zero component of electric field parallel to the magnetic field. Within the sheath, the perpendicular electric field is much stronger and the electrons drift across the magnetic field lines.

2.3 University of Alabama – Microstructure Characterization and Analysis

2.3.1 Influence of Surface Roughness on Electron Emission from Graphite and a Graphite-coated Hall Effect Thruster Chamber Wall Materials

2.3.1.1 Introduction

HETs have emerged as means for geosynchronous station-keeping and similar space-based propulsion applications[1]-[4]. The HET and similar ion thrust based proposal units, use quasi-neutral plasmas as a propulsion source[5]. One of the major lifetime limiting factor for these thrusters is the erosion of the ceramic chamber wall that protects the magnets which provide fields which encase the plasma within the thruster[6]. If these walls become fully eroded, the plasma is exposed to the magnetic casings and causes failure of the propulsion device. These chamber walls tend to be ceramics because of their high resistance to erosion, low density, and high electrical resistivity which prevents electrical grounding. Examples of these materials include hexagonal boron nitride (hBN), silica (SiO_2), and alumina (Al_2O_3)[7]. Though these materials are resistant to erosion, over an extended time, the surface is modulated from the plasma exposure. This type of erosion is created by a number of factors including sputtering and the loss of material from mechanical stress created by anisotropic thermal expansion within the ceramic material[2]. For example, Burton et al. reported how various surface features in an M26 (60 wt.% hBN – 40 wt.% amorphous-SiO_2) wall yielded both needle-like protrusions, micro-cracking, and smooth planar silica surfaces after extended plasma exposure [8].

While the properties of the bulk plasma are determined primarily by the design of the HET, the properties of the plasma sheath are controlled, in part, by the surface features of the channel wall [9][10]. These determine the wall's response to the surface electrical fields or affect its ability to re-emit electrons that escape the plasma and impact the wall surface. Hence, the variation of surface features dramatically changes the electron emission characteristics of the chamber wall with the plasma sheath and how the plasma sheath would then erode the chamber wall. These re-emitted secondary electrons (SE) and back scattered electrons (BSE) have a destabilizing effect on the plasma sheath, reducing the overall energy of the sheath, though the mechanism is not fully identified [11],[12]. Thus understanding the ways in which surface topological variations modify electron emission will allow for a more comprehensive understanding of the plasma sheath and thus the factors that cause erosion as well as plasma stability in HETs.

Though several studies have been conducted in the measurement of SEE from various material types[7].[13], to date, there has been little work in quantifying how the surface topology of such materials influences electron emission relative to the erosion features seen in HET chamber wall systems. Langendorf and Walker[14] have recently reported how the plasma sheath potential became altered between a 'rough' and 'smooth' hBN surface, though the extent of the topology change was not reported. Regardless, this result provides experimental indications that surface topology will influence the SEE that stabilizes the plasma sheath. Such emission alterations would be paramount in controlling the stability of the plasma and how the plasma interacts with the surface in terms of erosion mechanisms. The dynamical interaction of an eroding wall, which forms various surface features, and the plasma sheath that facilitates the erosion of the surface is an area rich for research investigation.

One of the major challenges to electron emission measurements from HET materials is their low electrical conductivity. In a typical electron emission study, a primary electron beam is focused onto to the surface whereupon the emitted surface electrons are captured [15]. If the sample is a dielectric, the surface will charge and repel the primary electron beam and such measurements cannot be acquired. Means to overcome this challenge have included pulsing of the primary electron beam to allow the surface to dissipate the charge build up [7]. Depending on the experimental setup, this can be an arduous experiment to ensure all the surface charge is dissipated prior to the next beam exposure. In contrast, a high electrical conductive sample does not suffer from this issues and can readily provide emission data.

We use graphite as a test case system to study how surface topology would affect emission behavior. Though not a typical HET chamber wall material, graphite has been used to understand the basic behavior of electron emission [16]. One of the key advantages of graphite is its high electrical conductivity, 15.5 $\mu\Omega$-m^{-1} [17], which would mitigate the prior charging issues discussed above. In addition, graphite has a very similar crystal structure to hBN, a common dielectric chamber wall material [7], [18], [19], both materials having the primitive hexagonal based structure of space group $P6_3/mmc$ for hBN with strong in-plane basal bonds and weak out-of-plane van der Waal bonds. This weak out-of-plane bonding leads to anisotropic cracking between the basal planes for both materials indicating the materials deform (erode) similarly. hBN is often referred to as 'white graphite' because of its similar flaking and lubricating properties for which graphite is known [20]. Since graphite is much more conductive than hBN, it then removes the subsequent surface charging effects and provides the ideal and alternate case study material for a specific study of topology effects on SEE, albeit at the expense of not providing the intrinsic SEE value specific to hBN.

Since plasma based erosion can take thousands to tens of thousands of hours of exposure [2], we have simulated modulated surface topologies through mechanical attribution using various grades of metallographic grinding and polishing pads. Furthermore, we will compare the scaling behavior of such surface features with the emission that results from an hBN-based composite that has been eroded under a plasma environment. For this channel wall, we have sputter coated graphite to reduce, if not eliminate the charging issues mentioned above. Though coating the surface will again give the emission characteristics of graphite, it provides a coverage of the topology allowing us to reasonably provide a conducting surface that mimics the underlying roughness of the chamber wall that was created from plasma exposure. By eliminating the charging issue, one can deduce how the effective emission changes based on the various plasma-specific erosion patterns along the chamber wall.

2.3.1.2 Experimental Setup

EC-17 grade, ultra-fine grain Electro Discharge Machining (EDM) graphite was chosen as the case study material. This was done to ensure that the graphite was as similar to the hBN material as possible that is used in HET. This graphite was acquired from Tokai Carbon where it was isostatically pressed and sintered with a resulting average grain size of approximately 2 μm with a density of 99+/-0.5 %. The hBN used in the plasma chamber wall was composed of 60 wt% hBN- 40 wt.% amorphous silica, denoted as M26 Combat© manufactured by Saint-Gobain. The silica is used to as a binder to help improve the structural strength of the composite. The hBN grains were of similar size to the graphite ensuring that the two microstructures were similar. The M26 HET chamber wall was sectioned from a P5 xenon plasma thruster that was operated at 1.5-5.0 kW for approximately 2000 hrs [6]. Two different regions of erosion – denoted as high and mild erosion – were secured. The details of the characterization of the erosion patterns in this wall material can be found in reference [8]. Both sets of samples – graphite and M26 - were sectioned into approximately 1cm x 1cm squares with thicknesses of approximately 5 mm.

All of the samples were mounted into 3.175 cm cold mount pucks using a Buehler SamplKwik acrylic cold mounting system which was then cut out of the mount after grinding or polishing. For the samples denoted as *polished*, they were all polished to 0.05 μm using an alumina-based polishing solution. The two *roughened* graphite samples surfaces were mechanically attritioned with either a 120-grit or 1200-grit SiC metallographic grade paper. Post grinding/polishing, all of the samples were cleaned of any surface contaminants by ultrasonic vibration in acetone followed by rinsing in isopropanol and deionized water and finally dried under compressed air. X-ray Photo-spectroscopy (XPS) performed in a Kratos Axis 165 XPS/Auger confirmed the removal of any polishing containments prior to SEE measurements. The M26 chamber wall materials exposed to the plasma were not mounted and polished in any manner but left in their as-eroded condition. To prevent surface charging, they were mounted onto a 15 mm x 15 mm piece of Ta foil with carbon tape on the backside of the sample after which an approximately 10 nm to 15 nm graphite coating was applied over the surface using a Cressington 208C Turbo Carbon Coater evaporator. Though the roughness of these features would likely prevent complete conformal coverage over all the surface because shadowing created by the roughness itself with line-of-sight sputtering, the coating was found to be sufficient to eliminate charging.

The samples surfaces were imaged by scanning electron microscopy (SEM) using a JOEL 7000 at 1000x magnification at a working distance of 10.0 mm with an acceleration voltage of 10 keV while imaging in secondary electron (SE) modes. Optical profilometry, to quantify the roughness, was performed by Evan's Analytical Group[21] using a Bruker Contour GT-X8 with a 50X optical lens. Three 1.3 mm x 0.95 mm areas were scanned from each sample where each scan had a vertical resolution of 6 nm and a lateral resolution of 6 μm. Roughness statistics were then collected across the entire scanned surfaces with root mean square (RMS) roughness (S_q), given below, as the primary statistic considered:

$$S_q = \sqrt{\{\Sigma (Z_i - Z_{avg})^2 / N\}} \quad (5)$$

where Z_i is the height of the feature, Z_{avg} is the average Z value within the scanned image, and N is the number of points in the image. For comparison to other roughness analytical methods, the geometric mean or average surface roughness (S_a) has also been calculated and is given as

$$S_a = (\Sigma Z_i) / N \quad (6)$$

The secondary electron emission coefficient was collected in a custom constructed stainless steel vacuum chamber at a base pressure of approximately $1x10^{-6}$ Torr pumped by mechanical and turbomolecular pumps. A primarily accelerating electron beam was rastered across each sample at energies between 50 eV to 100 eV and then 100 eV to 500 eV at 100 eV step sizes. The electron current through the sample was then measured while under the primary e-

beam irradiation. After each measurement, the sample was charged to +100 Volts to recollect all escaping secondary and backscattered electrons. The new net current of re-collected electrons (i_N) and the current from the primary electron beam (i_P) then used to calculate the SEE coefficient, δ, from:

$$\delta = 1 - (i_N / i_P). \quad (7)$$

The value for delta was collected once every 5 s, for 600 s and the value for delta, at the particular energy level, was the average of the last twenty values. The error for this energy level was also calculated from this same data set.

2.3.1.3 Results and Discussion

The micrographs and optical profilometry height maps of the graphite samples can be seen in Figure 34. From these images, one can easily discern the ever increasing level of surface roughness. At the highest roughness, the clear and coarse polishing lines are evident within the surface. At all levels of polishing, the graphite revealed some level of mechanical instability in the microstructure evident by the graphite grains showing some jagged features that have been termed flaking. The average roughness (S_a) and RMS roughness (S_q) of the polished graphite were 0.070 ± 0.004 μm and 0.110 ± 0.022 μm, the 1200 grit graphite was 0.780 ± 0.022 μm and 0.990 ± 0.019 μm, and the 120-grit graphite was 5.60 ± 0.842 μm and 7.10 ± 1.23 μm, respectively.

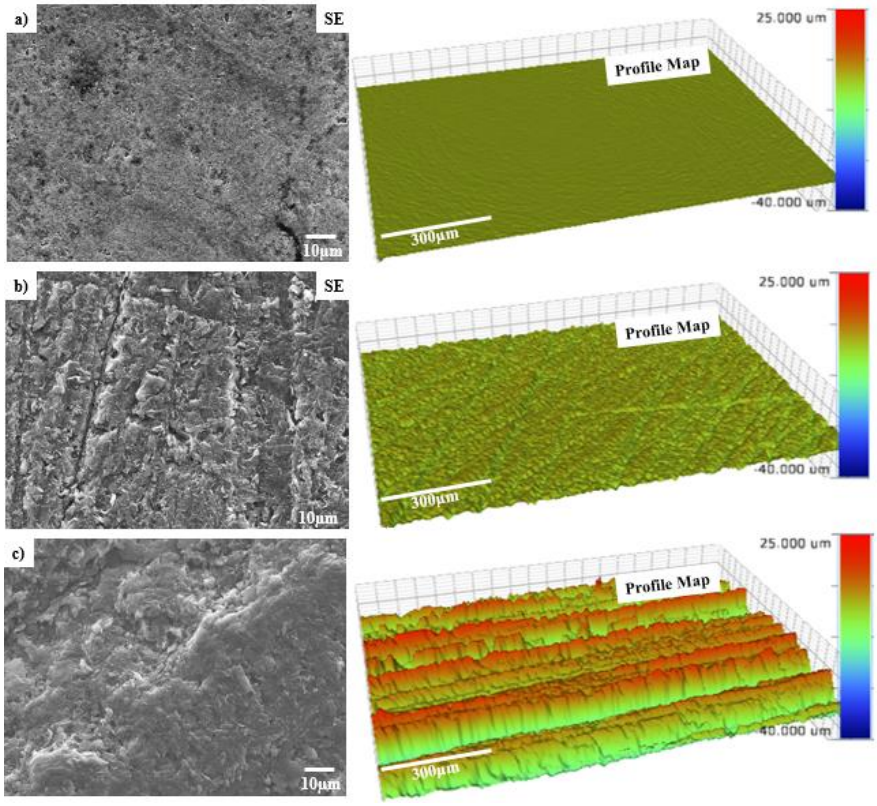

Figure 34. The secondary electron micrograph and the optical profilometry map of the (a) **polished graphite,** (b) **1200-grit roughened graphite, and** (c) **120-grit roughened graphite samples.**

The SEE coefficient as a function of primary electron beam energy and surface preparation is plotted in Figure 2. As to be expected, the polished graphite surface had the highest SEE coefficient, with a maximum value near 300 eV. The smooth and planar surface provided the conditions where the vast majority of electrons were able to emit from the surface and contribute to the measurement. The next highest emission came from the roughest surface – graphite 120 grit – and was approximately one-third lower in its emission coefficient than the polished or smooth surface. It too followed a similar trajectory of increasing and decreasing emission, with a maximum emission near 200 eV, with the primary electron beam energy. Finally, the lowest emission sample was the middle roughness surface – graphite 1200 grit – with a substantially lower emission coefficient value than either of the other surfaces with a maximum

emission near 100 eV. Interestingly, at 50 eV, the emission coefficient for this sample increased with this response repeated and confirmed. This increase is contributed to electrons that are elastically reflected from the surface, rather than being absorbed and re-emitted [22]. It is not clear why this effect was not observed in the other two surfaces; however, the value for the two roughest surfaces at 50 eV are approximately equivalent. At 300 eV and larger primary electron beam energies, both roughened surfaces – graphite 120 and 1200 grit – converge with nearly similar SEE coefficient values suggesting at higher energies, any differences in roughness have been overcome. The standard deviation around these average δ values was approximately $2x10^{-3}$, and never rose higher than $4x10^{-3}$ for any measurement. Note that this small error value in each of these measurements precluded error bars from being readily observable in Figure 35.

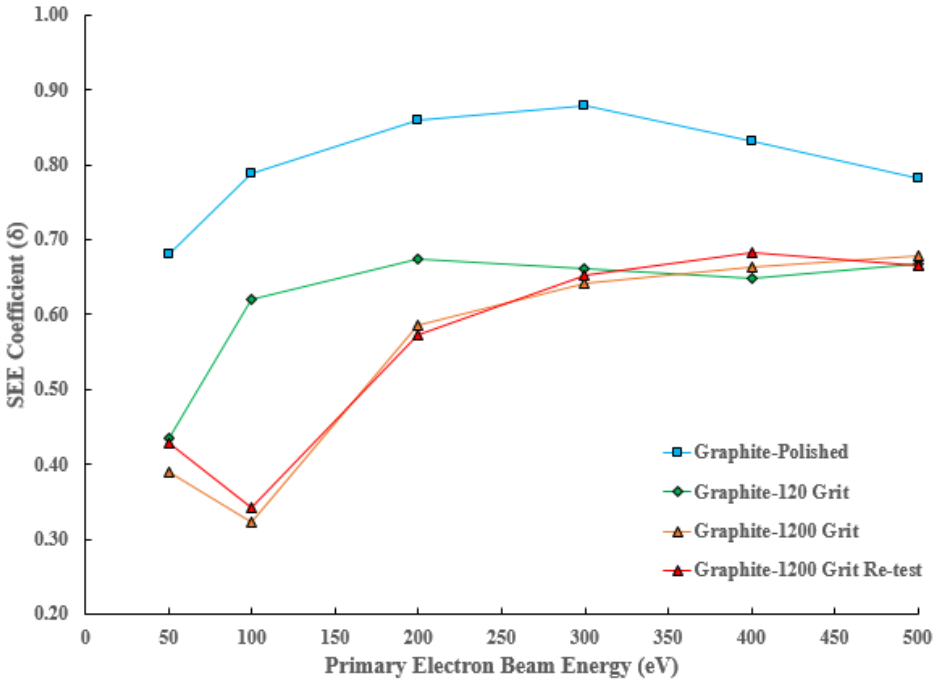

ap

Figure 35. The measured secondary electron coefficient at each energy level are plotted. Note that the roughest sample, 120 grit, does not correspond to the lowest emission response.

From these scans, it appears that a critical length scale influences the SEE coefficient. One could assume that the rougher the surface, the lower the SEE as more of the surface could obstruct emission. This is not the case. The graphite 120 grit roughest surface (7.10 ± 1.23 μm) has a SEE coefficient value that is lower than the graphite 1200-grit surface (0.990 ± 0.019 μm) when the primary electron energy is lower than 300 eV. At the lowest energies, SEE would be the most sensitive because the electrons would need sufficient energy to escape. Langendorf [23] reported a ray trace model for electron trapping as a function of modulated topologies. In this model, as the depth of a groove increased, the probability of an emitted electron to escape the groove decreased because it had a greater opportunity to collide and be absorbed by the side walls with of the groove. Similarly, if the spacing between grooves decreased, then the emission decreased, for a fixed groove depth, because less surface area above the groove would be present.

To illustrate the effect of roughness as a function of length scale, the average roughness values have been replotted as a function of partition area in Figure 36 with the error being the deviation of such averages. Hence for the largest partitioned area, this is taken as the entire surface roughness, with the subsequent partitioning of that area in ever reducing half-values of the preceding size. By reducing the scanned area and reporting the average and standard deviation of the roughness between different areas, one can glean how at smaller viewed length scales, the measured roughness changes and various between ever smaller and smaller areas.

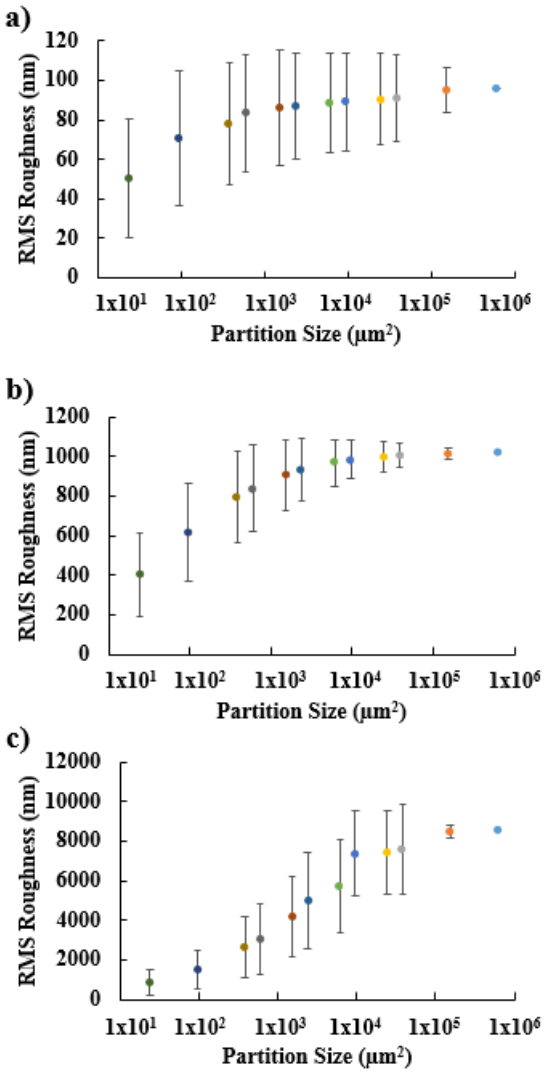

Figure 36. The roughness as a function of reduced binned areas for the (a) polished graphite, (b) 1200-grit graphite, and (c) 120-grit graphite samples.

As can be seen in Figure 36(a), for the smoothest surface, as the sampling area or partitioned size decreased, there was very little change in roughness indicating that at both small and larger fields of view, the surface is relatively uniform in its roughness. In contrast, for the 120- and 1200-grit samples, as one reduced the partitioned size, the mean roughness dramatically decreased meaning that at a finer feature size, the mean surface is less rough. However, the large error bars within each partitioned size does indicate dramatic variations from sampled region to sampled region. By considering this mean at approximately 10^3 μm^2 and 10^4 μm^2 the onset of a reduction of the mean roughness occurred for the 1200-grit and 120-grit conditions respectively. For the extremes in partitioned sizes for these samples, the mean values are outside the error range indicating that the roughness of the surface does decrease as one views an ever decreasing field of view. This change is most notable in the 120-grit graphite – or the largest macroscopic roughness. At the finest partition size, it equivalent to the majority of values quantified for the 1200-grit graphite. The reduction of the error about the average RMS value, particularly, at the finer partition areas, is also the most pronounced as compared to the other surfaces. Hence, at the finest sizes, the differences in roughness are not as large. Due to the limited resolution of the optical roughness measurement for partition sizes, the convergence of partition sizes between all three surfaces could not be achieved.

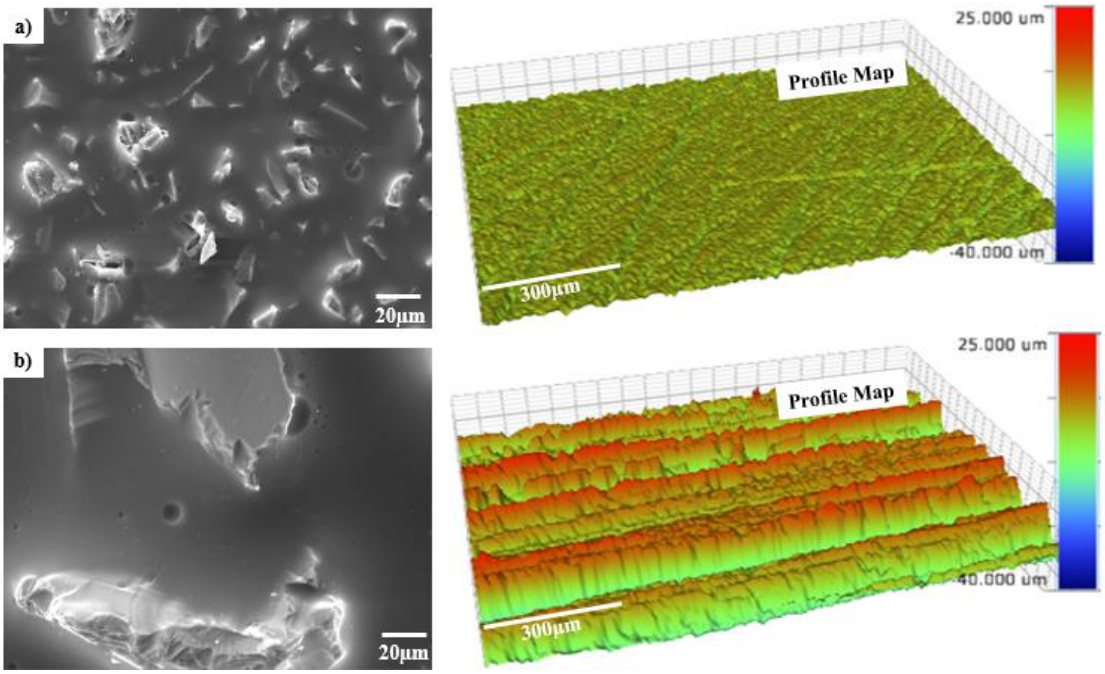

Figure 37. The surface of the silicon carbide polishing pads showing the grinding media and the binder that holds it to the pad for the (a) 1200-grit pad, and (c) 120-grit pad.

From Figure 36, the influence of the macroscale roughness became less and less pronounced suggesting that a that a critical roughness value exists where a surface with an overall coarser macroscopic roughness, but a local smooth surface at a finer scale, can have a less pronounced effect on the trapping electrons. Such an effect can be inferred from the optical profilometry scan of the 120-grit surface in Figure 34(c). Large scale scratch lines can be seen in this image. These features are formed from the larger particulates used in the 120 grit paper, shown in Figure 37a). Though these particulates are larger and yield a rougher surface or one with deeper grooves, their size does leave a smoother surface if the field of view is limited. Moreover, the larger particulates will also produce a surface with the spacing between each polishing line to be further spaced apart. For the 1200-grit paper, the particulates, Figure 37(b), are finer than the 120 grit creating a reduced overall roughness (a less deep groove) as well as a finer spaced variation of topology as the polishing lines are closer. Though the overall surface for the 1200 grit is smoother than the 120 grit, if the surface modulations are sufficiently modulated at a finer scale it can reduce the emission. However, if these finer scale modulations eventually become sufficiently smoothed –the polished graphite – electron emission can be recovered and increased.

Though the roughness of the 120 grit is still larger than the 1200 grit, which refers to the groove depths, the limited lateral spatial resolution of the optical profilometer prevented the necessary resolution to quantify the roughness between the polished lines. Based on the SEM micrographs of Figure 4, one can infer that the spacing between the polished lines created by the particulates from the polishing paper surface would be further apart for the 120-grit sample as compared to the 1200-grit paper. Between such polished lines, the material surfaces would be smooth (no deep grooving) and yield high-emission regions. Hence, one must consider both groove depth and spacing for the trapping of electrons as reported by Langendorf [23].

Analysis of graphite coated HET wall samples.

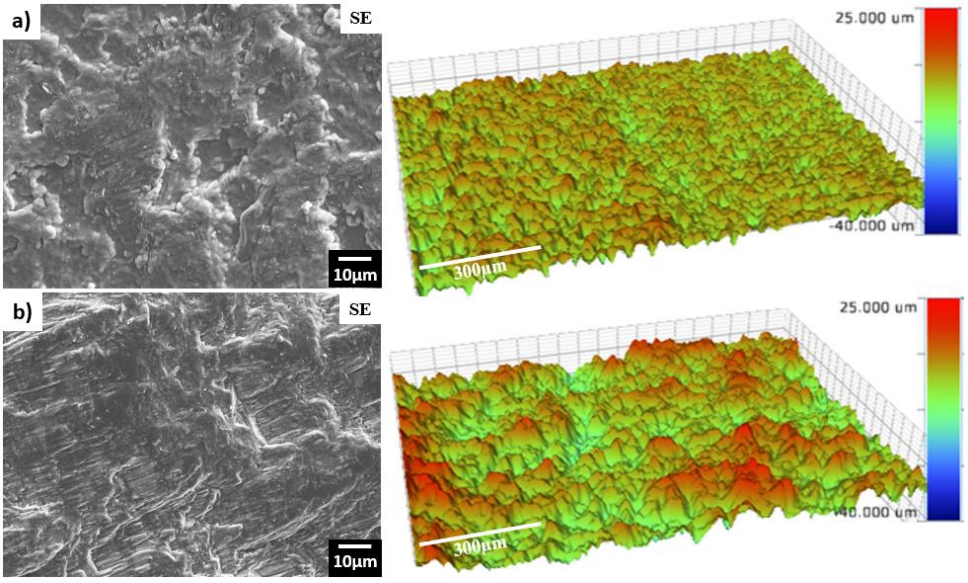

Figure 38. The secondary electron micrograph and the optical profilometry map of the (a) mild erosion HET, and (b) high erosion HET samples.

To determine if a roughness dependence of SEE existed in the M26 chamber wall, the SEE coefficient from the mild and high eroded surfaces was found (via a graphite surface coating). Figure 38 is the SEM micrographs and optical profilometry of each of the relevant HET surfaces. The average roughness (S_a) and RMS roughness (S_q) of the mild erosion HET wall were 3.00 ± 0.88 μm and 4.00 ± 0.95 μm, respectively, and the highly eroded HET wall was 4.70 ± 0.67 μm and 5.80 ± 0.75 μm, respectively. As seen in Figure 39, the highly eroded surface exhibited a higher emission than the mildly eroded surface.

While the roughness of the mild and high erosion surfaces are similar, the statistics show that the mild surface is approximately half as rough as the high erosion. In comparison, the graphite 120-grit and 1200-grit roughness were an order of magnitude different and the topologies are different because of how the attrition occurred. Regardless of these differences, both samples reported that the roughest surface does not necessarily result in the lowest SEE. Using the reduced field of view (smaller partitioned size), the value of how the roughness changed was noted. What was particularly surprising was that the higher roughness sample from the wall material has a nearly equivalent value and trend as the polished graphite sample from above. This value has been inserted in Figure 6 for easier viewing. As noted above, this suggested that a critical length size for emission existed as a function of roughness.

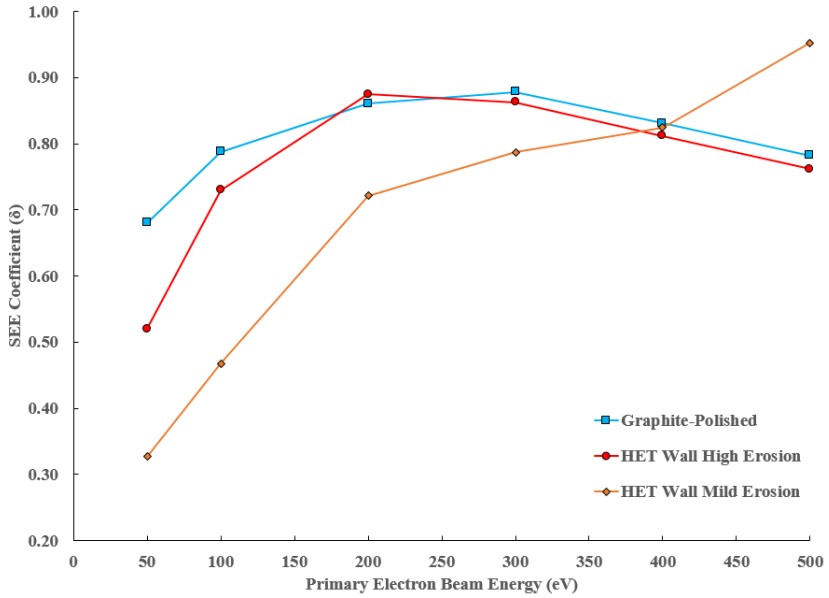

Figure 39. The secondary electron micrograph and the optical profilometry map of the (a) mild erosion HET, and (b) high erosion HET samples.

2.3.1.4 Conclusions

This study investigated how surface roughness influenced the SEE behavior in both the graphite and in a graphite coated HET chamber wall that had a modulated surface roughness. Graphite provided an ideal case study in that it was electrically conductive for ease SEE measurements and shares common crystallography with hBN, a common HET chamber wall. It was found that the smoothest surface yielded the highest SEE. This was expected because such a surface would have very limited obstructions for electron emission. However, the roughest surface did not have the lowest SEE. Rather a surface with moderate roughness yielded the lowest emission. At sufficiently high electron beam energies (> 300 eV), the emission between these two roughened samples became equivalent. The difference in emission for lower energies for the two roughened surfaces was explained in terms of a reduction of the roughness as a function of a finer field of view. Though a surface may have a coarse roughness, the emission comes from a local surface which, in of itself, could be smoother. Thus, how a material surface roughness is reduced at finer length scales must also be considered. For the roughest graphite surface, this noticeable change in mean roughness occurred at nearly in order of magnitude larger area than that of the moderate roughness surface. Thus, the roughest surface does not necessary mean the lowest emission. Similarly, a graphite coated plasma eroded chamber wall, which had coarser and moderately eroded regions showed similar behavior, with the moderate roughness having a lower emission. Collectively, this suggests that a critical length scale in terms of roughness existed for the SEE from these materials.

2.3.1.5 Acknowledgements

The authors would like to gratefully acknowledge the support of Abhishek Kumar for his technical assistance in the partitioning of the roughness data.

2.3.1.6 References

[1] D. Y. Oh, T. Randolph, S. Kimbrel, and M. Martinez-Sanchez, "End-to-End Optimization of Chemical-Electric Orbit-Raising Missions," J. Spacecr. Rockets, vol. 41, no. 5, pp. 831–839, Sep. 2004.

[2] K. De Grys, A. Mathers, B. Welander, and V. Khayms, "Demonstration of 10,400 Hours of Operation on 4.5 kW Qualification Model Hall Thruster," AIAA Pap., vol. 6698, p. 2010, 2010.

[3] N. Gascon, M. Dudeck, and S. Barral, "Wall material effects in stationary plasma thrusters. I. Parametric studies of an SPT-100," Phys. Plasmas, vol. 10, no. 10, p. 4123, 2003.

[4] S. Barral, K. Makowski, Z. Peradzyński, N. Gascon, and M. Dudeck, "Wall material effects in stationary plasma thrusters. II. Near-wall and in-wall conductivity," Phys. Plasmas, vol. 10, no. 10, p. 4137, 2003.

[5] A. Aanesland, A. Meige, and P. Chabert, "Electric propulsion using ion-ion plasmas," J. Phys. Conf. Ser., vol. 162, p. 12009, Apr. 2009.

[6] R. R. Hofer, I. G. Mikellides, I. Katz, and D. M. Goebel, "BPT-4000 Hall thruster discharge chamber erosion model comparison with qualification life test data," in 30th International Electric Propulsion Conference, 2007, pp. 17–20.
[7] V. Viel-Inguimbert and others, "Secondary electron emission of ceramics used in the channel of SPT," in 28th International Electric Propulsion Conference, Toulouse, France, 2003.
[8] T. Burton, A. M. Schinder, G. Capuano, J. J. Rimoli, M. L. Walker, and G. B. Thompson, "Plasma-Induced Erosion on Ceramic Wall Structures in Hall-Effect Thrusters," J. Propuls. Power, vol. 30, no. 3, pp. 690–695, 2014.
[9] D. M. Goebel and I. Katz, Fundamentals of electric propulsion: ion and Hall thrusters, vol. 1. John Wiley & Sons, 2008.
[10] R. Franklin, "The plasma–sheath boundary region," J. Phys. Appl. Phys., vol. 36, no. 22, p. R309, 2003.
[11] G. Hobbs and J. Wesson, "Heat flow through a Langmuir sheath in the presence of electron emission," Plasma Phys., vol. 9, no. 1, p. 85, 1967.
[12] M. Campanell, A. Khrabrov, and I. Kaganovich, "General cause of sheath instability identified for low collisionality plasmas in devices with secondary electron emission," Phys. Rev. Lett., vol. 108, no. 23, p. 235001, 2012.
[13] P. Dawson, "Secondary electron emission yields of some ceramics," J. Appl. Phys., vol. 37, no. 9, pp. 3644–3645, 1966.
[14] S. Langendorf and M. Walker, "Effect of secondary electron emission on the plasma sheath," Phys. Plasmas 1994-Present, vol. 22, no. 3, p. 33515, 2015.
[15] A. Shih, J. Yater, C. Hor, and R. Abrams, "Secondary electron emission studies," Appl. Surf. Sci., vol. 111, pp. 251–258, 1997.
[16] M. Woods, B. Hopkins, G. Matthews, G. McCracken, P. Sewell, and H. Fahrang, "An investigation of the secondary-electron emission of carbon samples exposed to a hydrogen plasma," J. Phys. Appl. Phys., vol. 20, no. 9, p. 1136, 1987.
[17] "EDM Graphite Grade Info." [Online]. Available: https://rapidholdingsystems.com/product/ec-17-mwi-high-precision-grade-edm-graphite/. [Accessed: 05-May-2016].
[18] N. Pellerin, L. Balika, S. Pellerin, C. Focsa, E. Véron, D. Pagnon, and M. Dudeck, "Ageing of ceramics in a Hall Effect Plasma thruster," in 20th International Symposium on Plasma Chemistry (ISPC), 2011, p. xx.
[19] V. Kim, V. Kozlov, A. Semenov, and I. Shkarban, "Investigation of the Boron Nitride based Ceramics Sputtering Yield Under its Bombardment by Xe and Kr ions," in International Electric Propulsion Conference, IEPC-01-073, Pasadena, Ca, 2001.
[20] K. A. Schwetz, "Boron carbide, boron nitride, and metal borides," Ullmann's Encycl. Ind. Chem., 1985.
[21] "Evan's Analytical Group." [Online]. Available: http://www.eag.com/mc/optical-profilometry.html. [Accessed: 02-Mar-2016].
[22] R. Cimino, I. Collins, M. Furman, M. Pivi, F. Ruggiero, G. Rumolo, and F. Zimmermann, "Can low-energy electrons affect high-energy physics accelerators?," Phys. Rev. Lett., vol. 93, no. 1, p. 14801, 2004.
[23] S. J. Langendorf, "Effects of Electron Emission on Plasma Sheaths," 2015.

2.3.2 Effect of Debye-scale surface features on space charge saturation of plasma sheaths

2.3.2.1 Introduction

HETs are plasma-based electric propulsion devices used in low thrust, high impulse applications such as those for geosynchronous satellite station keeping[1]. In the HET design, a magnetic field is used to trap electrons in a closed azimuthal drift that concentrates the electric field of a direct current (DC) discharge to accelerate propellant ions. The ions accelerate through a quasi-neutral plasma region that contains both ions and electrons. Thus, the thrust density is not influenced by the space charge limit. Figure 40 shows a representative diagram and in-operation photo of a HET.

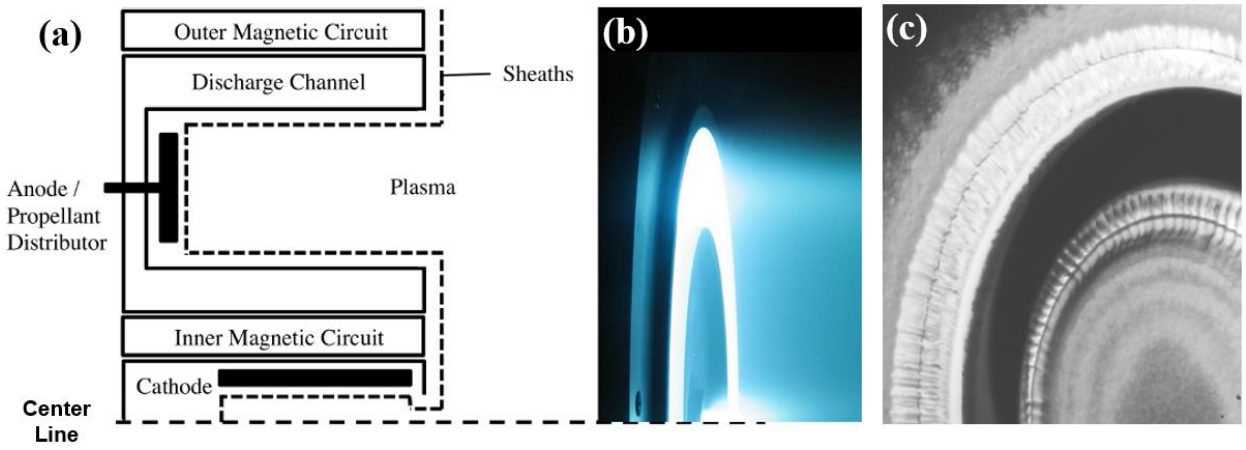

Figure 40. (a) Schematic and a photo of HET cross section, shown with a center-mounted cathode. (b) A photo of a 6-kW xenon ion HET in operation (Photo credit: NASA/JPL-Caltech), and (c) the erosion ridges formed on the chamber wall after 10,400 hrs of operation on a 4.5-kW HET [2].

In the development of HETs, plasma–wall interactions have been found to play a key role in the thruster operation and performance [3]-[5]. With ion and electron movement in the plasma region, their impact into the thruster wall and electrodes create heat, material erosion, and a loss of thruster efficiency. In addition, space charge saturation of the plasma sheath can form along the discharge channel wall and contribute to electric field oscillations and anomalously high levels of electron transport to the thruster anode [6]. Since these impacts are continuous and related to the plasma density, the surface wall morphology will evolve during service creating a dynamic plasma-wall interaction. Burton et al. have reported on sub- and near sub-micron erosion patterns in a hexagonal boron nitride (hBN) - amorphous silica (SiO_2) HET wall material exposed to a krypton plasma [7]. A variety of jagged protrusions were noted as well as smooth planar surfaces created from the exfoliation of entire grains from stress created by the anisotropic thermal expansion of hBN. Such surface features and their accompanying surface area will modify the secondary electron emission (SEE) yield from the wall and thus influence the plasma sheath stability.

SEE from the discharge channel wall has been found to have a significant effect on power efficiency and bulk plasma electron temperatures in HETs [8]-[10]. It has been reported that significant levels of SEE from the HET channel walls can lead to dramatic drops in the magnitude of the sheath potential as these emitted electrons neutralize the ion-rich sheath. This situation is sometimes referred to as a "space-charge-saturation" of the sheath [11],[12]. These differences are suspected to depend on the length scale of the surface structure. Langendorf and Walker [8], using different metallographically-polished hBN surface finishes, noted these changes in the plasma sheath potential if the surface was smooth or rough. The length scale of these metallographically-polished surface topologies was on the order of tens of microns dependent on the polishing grit paper. For a HET that has a high plasma density and a thin plasma sheath on the order of tens of microns, even a 'smooth' wall can appear 'rough' creating dissimilarities in the near-surface plasma characteristics[8]. If the chamber wall is exposed to the discharge plasma for an extensive time, radially-symmetric surface modulations, at a larger characteristic length scale than the plasma sheath thickness, have been observed and are shown in Figure 40(c). In the effort here, we have extended the prior work of Langendorf and Walker [8] to address plasma-material interactions that are at larger length scale modulations (orders of millimeters) on the material surface. Though such large length scale surface topologies in HET thruster walls can take thousands of hours of operation to form (Figure 40(c)), quantifying their effect on the plasma sheath is essential for predicting HET efficiency and long-term behavior [8],[13],[14].

One of the challenges in investigating plasma-wall interactions and discharge channel plasma sheaths is the need to make measurements *in situ.* For a thruster, this poses a significant challenge because of its high plasma density and tens of microns sheath spacing. However, due to the scalability and dimensionless formulation of sheath theories [15]-[17], it is feasible to examine the physics in a nominal plasma environment with a lower plasma density. By creating surface features at the Debye length of lower density plasma, on the millimeter length scale, we can use a Langmuir probe to measure the sheath behavior between the different topologies. Effects of surface features smaller-than-Debye length scales on SEE were previously investigated [13],[18] and found to be consistent with a trapping of the secondary electrons near the wall surface. How such behavior may be altered at the more macroscopic length scale created by a coarser topology is the subject of this work. By quantifying this length scale behavior, we were able to elucidate how

the plasma sheath behaves near these coarser variations in the discharge channel wall and how current theories are able to capture the physics of this interaction.

2.3.2.2 Experimental Setup

The plasma used in this study was non-Maxwellian with a significant fraction of energetic primary electrons that intentionally stimulated SEE from our modified surfaces. By varying the energy of the primary electrons, we were able to determine the critical energy at which the emitted electron density is sufficient to neutralize and/or saturate the sheath, creating the collapse voltage transition. This plasma was generated in a low-density multi-dipole plasma cell lined with permanent magnets that created confining cusp fields, as shown in the diagram of Figure 41. These cusp magnetic fields decay rapidly away from the permanent magnet dipoles around the boundary, so the main plasma volume of the device is not magnetized. The cell was cylindrical in shape and had a radius of 30.5 cm and a height of 91 cm with the cell walls being aluminum and grounded. Typical plasma densities used were approximately 10^{13} m^{-3} at an electron temperature of 3 eV with a 1-10% energetic electron population.

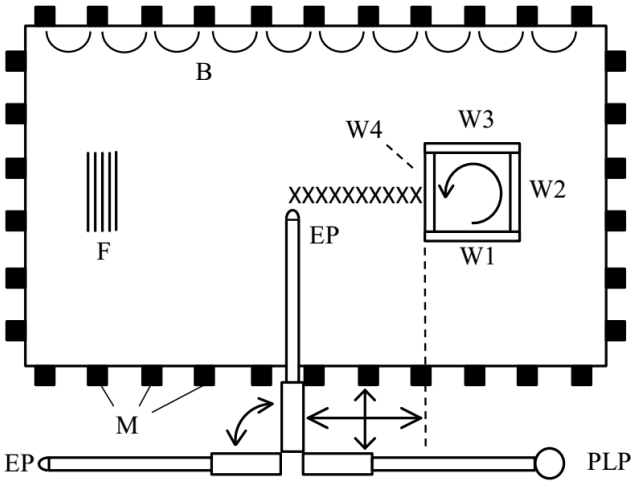

Figure 41. Diagram of plasma cell and diagnostics. F = filaments, M = magnets, B = nominal magnetic field, PLP = planar Langmuir probe, EP = emissive probe, W = wall material sample, X = nominal data measurement location. Emissive probe orientation rotated 90° in the figure to show hairpin tip geometry. Not to scale.

The plasma was generated by collisional ionization of ultra-high purity (UHP) 99.999% argon gas with energetic electrons emitted from thoriated-tungsten filaments positioned inside the cell. The electrons are accelerated into the sample by application of the discharge voltage (between -60 V to -175 V) between the filaments and the device frame. The Debye length for the plasma under these conditions was calculated from probe measurements to be between 3 mm and 5 mm for the lower discharge voltages and higher discharge voltages respectively. The plasma cell is housed in a large vacuum chamber which achieved a base pressure of ~1 x 10^{-8} Torr [19]. During operation, 500 standard cubic centimeters (sccm) of UHP argon was flowed into the chamber using an MKS 1179A01352CS1BV mass flow controller to achieve the experimental pressure of ~1 x 10^{-4} Torr.

Disks were made from the dielectric materials of hBN that measured 7.6 cm in diameter and 0.64 cm in thickness. This material has a large SEE coefficient due to the electron bombardment which increases with the energy of incident electrons. It is also a commonly used ceramic chamber wall material in HETs. The purity grade of the hBN was AX05 (99.9%). Five (5) mm wide grooves were machined into the surface of the disks, Figure 41(a)-(b), which were spaced 10 mm apart with uniform depths of either 1 mm or 5 mm, Figure 41(c). A control disk with no grooves was also used for comparison. Prior to insertion into the plasma chamber, the disks were cleaned with acetone, deionized water then air dried. The hBN disks were mounted to a box holder made of stainless steel.

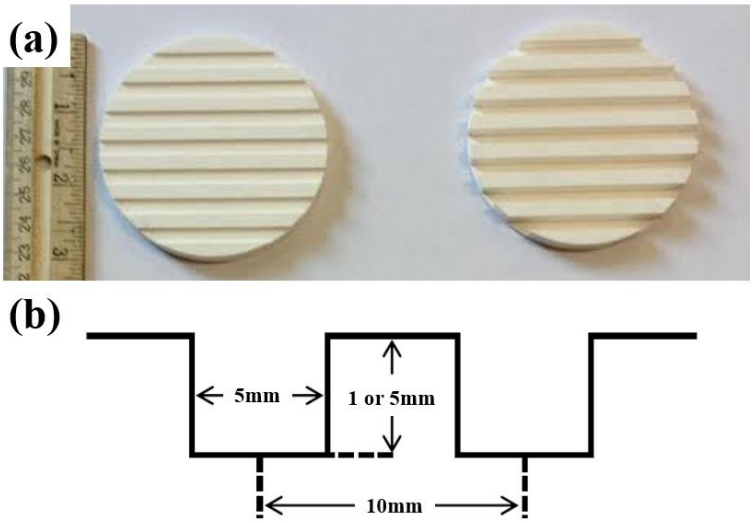

Figure 42. Photos of the a) hBN prior to the experiment, ruler included for scale reference. b) A diagram of the grooves that were machined into the disks with the important geometries labeled.

The sheath potential over the wall material samples was measured using an emissive probe constructed of telescoping alumina tubing and a hairpin 0.127 mm diameter thoriated tungsten filament tip. The emissive probe is biased with a Keithley 2410 Sourcemeter. Bulk plasma parameters were measured using a planar Langmuir probe positioned in the center of the plasma device. The probe was cleaned by ion bombardment at 500 V bias for a period of 15 min before data collection; the probe was re-cleaned at 500 V for 30 s after the collection of each trace. The Langmuir probe body was constructed of alumina tubing. The tip was made from 0.5-mm thick tungsten foil cut into a 7.70-mm diameter circle. Five linear stair sweeps from -200 to 0 V were collected with an average dwell time of 20 ms at each voltage at a step interval of 0.2 V. The probe characteristics were corrected for singly-charged argon ion- and electron-induced SEE using data for tungsten from reference [20].

2.3.2.3 Computational Methods

Since the grooves provide a modulated surface topology for SEE that will impact the plasma sheath, modeling these electron trajectories from such features were undertaken and forward fed to plasma models to simulate the sheath behavior. These simulations were then compared to the experimental characterization of the sheath to gain insights into the potential mechanisms that govern plasma characteristics over such macroscopic topological features.

The optical obstruction model is based on a defined geometry which can result in electron trapping. This model assumed electrons are diffusely emitted from the surface and followed an unperturbed ray trajectory. If these electrons intersect a surface feature, they are unable to 'emit' from the material and are considered trapped. Hence this model is independent of material type but dependent on surface topology. The groove height (h) divided by the groove width (w) is referred to as the aspect ratio (AR). The view factor expressions are then defined in terms of AR as the following:

$$F_{\frac{ES}{SE}} = \sqrt{(1 + AR^2)} - AR \tag{8}$$

$$F_{EB} = \frac{1 + AR - \sqrt{(1 + AR^2)}}{2} \tag{9}$$

where $F_{ES/SE}$, is the view factor expression for an infinite strip adjoining another strip at a 90° angle and where F_{EB} is the view factor expression for two strips separated by a given width, these form the geometric construction of the grooves as shown schematically in Figure 42(a)

The overall reduction in SEE, which is denoted as the ratio of emission, γ, normalized by the nominal emission from a smooth or non-grooved surface, γ_0, was constructed from the view factor equations above and given as:

$$\frac{\gamma_{groove}}{\gamma_0} = {F_{EB}}^2 + 2F_{ES} \times F_{ES} \tag{10}$$

where F_{EB} is the contribution from the bottom of the groove, Eq. (2), and F_{ES} and F_{SE} are the emission contributions from the two side walls of the groove, Eq. (1). The nominal emission, γ_0, was referenced from a smooth surface (no grooves) and assumed to be a constant. Note that Eq. (3) only accounts for the aspect ratio and does not account for the groove ratio. To incorporate the groove ratio (*GR*), which is the groove spacing (*s* in Figure 42(a)), divided by the groove width, the SEE emission ratio becomes

$$\frac{\gamma}{\gamma_0} = GR\left(\frac{\gamma_{groove}}{\gamma_0}\right) + (1 - GR). \tag{11}$$

The resulting effective SEE yield (γ/γ_o) curves for a set of grooved ratios are plotted as a function of the aspect ratio in Figure 43(b). Using this plot we note that at high aspect ratios (deep grooves), very few straight-line paths are available for the electrons to escape the groove. However, at high groove ratios (bottom curve in Figure 43(b)), the density of grooves to trap electrons greatly increases. While at an equal aspect ratio, the effective SEE yield decreased by nearly 70% as compared to a smooth surface, *i.e.*, an aspect ratio of zero. With a decreasing groove ratio, which means either the groove width increased or the groove spatial wavelength decreased, the effective SEE yield will increase.

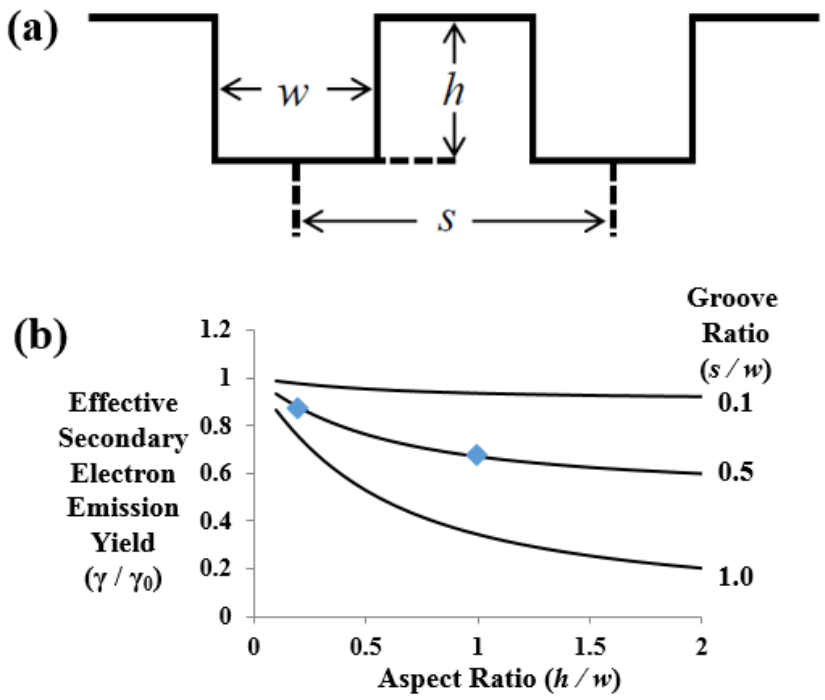

Figure 43. a) Geometric variables of the grooves that were machined into the disk samples. (b) Results of the optical trapping model showing the decreasing emission from differently shaped grooves. The blue diamond markers indicate the geometries of the grooved samples in this experiment.

The experimental geometries studied are indicated by the diamond markers on Figure 43(b). For the h = 1 mm groove sample with an aspect ratio = 0.2 and a spacing ratio = 0.5, a SEE reduction factor of ~0.87 is expected. While the h = 5 mm groove sample with an aspect ratio = 1.0 and groove ratio = 0.5 will result in a SEE reduction factor of ~0.67. Having obtained an estimate of SEE reduction because of surface topology, *i.e.* the grooved topology, the γ/γ_0 values from Eq. 4 were incorporated into an analytical one-dimensional plasma kinetic sheath model to obtain predicted SEE which was compared to the experimental results, Figure 44(b) described in the results section.

In our kinetic models, the plasma was described by the system of equations that included the Boltzmann equations for electron and ion distribution functions, Poisson's equation for electrical potential and the currents balance equation for the floating potential of the emissive plate. These generic equations can be found in reference [13], [21]. In the first model, referred to as the 'collapse voltage model,' a simplified 1D construction of the plasma sheath was undertaken for a truncated geometry which was based on the classical model by Hobbs and Wesson [11] with the inclusion of the kinetic considerations as developed by Sheehan [22]. This allowed for the analysis of the sheath

collapse at a wide variety of groove geometries and primary electron energy levels without the significant computational expense. However, we only considered the 1D directional flow of plasma ions and electrons into the sheath and their impact on the wall as well as secondary electrons emitted from the wall returning back to the plasma. The distribution functions for the bulk plasma electrons (Maxwellian at sheath entrance), secondary electrons (half Maxwellian emitted from the wall), and energetic primary electrons emitted from the discharge filament (isotropic mono-energetic at the sheath entrance) were computed. The energy levels of the electrons and ions for this simulation were T_e = 3 eV and T_i = 0 eV, respectively. The floating wall potential was solved to enforce the current balance condition and the electric field and potential in the sheath which was determined to be self-consistent from the spatial densities of the charged-particle populations. The SEE yield of the wall was calculated from a user-specified curve of total SEE yield versus incident electron energy. This energy-dependent SEE yield was integrated across the incident electron distributions at the wall and was multiplied by the γ/γ_0 value (given above in section III.A) approximating the influence of the grooves on SEE. This enabled the study of the sheath collapse phenomena of interest. A more detailed description of the 1D sheath model is given in reference [8] with further information concerning the derivations of the optical and kinetic models found in reference [21].

The second model is a full simulation of the plasma where the sheath is allowed to form simply because of the near-surface boundary conditions. From this simulation, distributions of charge and potential changes can be created albeit at the expense for one set of geometries and primary electron energy level. To model these surface interactions, a Particle-In-Cell (PIC) Monte Carlo Collisions (MCC) method was employed. The PIC model was two-dimensional in space (2D) and three-dimensional in terms of electron and ion velocity (3D). The distribution functions for the electrons and ions were found from the Boltzmann equations given as

$$\frac{\partial f_e}{\partial t} + \vec{v}_e \frac{\partial f_e}{\partial \vec{r}} - \frac{e\vec{E}}{m} \frac{\partial f_e}{\partial \vec{v}_e} = J_e, \quad n_e = \int f_e d\vec{v}_e \tag{12}$$

$$\frac{\partial f_i}{\partial t} + \vec{v}_i \frac{\partial f_i}{\partial \vec{r}} + \frac{e\vec{E}}{M} \frac{\partial f_i}{\partial \vec{v}_i} = J_i, \quad n_i = \int f_i d\vec{v}_i \tag{13}$$

where v_e, v_i, n_e, n_i, m, and M are the electron and ion velocities, concentrations, and masses, respectively; J_e and J_i are the collisional integrals for electrons and ions with background atoms. Knowing the distribution functions for these electrons and ions, the mean energy of charged species was calculated along with their concentrations, and elastic and non-elastic collisional rates and assumed a zero-current balance into the surface of the floating emissive plate. The floating potential of the emissive plate was calculated to be self-consistent from the condition of a zero total current into the hBN plate surface using Poisson's equation describing the electric potential distribution.

Since the discharge operated in argon, the kinetics of electrons included an elastic scattering of electrons on background atoms, excitation of metastable states, and ionization. For ions, we took into account the elastic and resonant charge exchange collisions. The SEE coefficient is calculated by accounting for the energy distribution functions of the electrons approaching the plate surface. Since we are most interested in the grooved feature, the PIC simulations for the plasma was only near these features with a calculated domain size of 7 cm x 5 cm with the plate having a diameter of 55 mm with four 5 x 5 mm grooves on its surface.

The grooved boundary conditions were referred to a domain embedded in unlimited quasi-neutral plasma with Maxwellian electrons and ions at the temperatures T_e = 3 eV and T_i = 0.026 eV, respectively for PIC. Additionally, a mono-energetic electron beam entered the calculation domain from the bottom boundary so that the electron component of the plasma consisted of a Maxwellian part and beam electrons. The electron and ion fluxes at the boundaries were constant with the electrical potential being that of a quasi-neutral plasma. The floating potential was calculated separately inside of the groove for the side walls and the bottom taking into account both the fluxes of electrons and ions from the plasma and the secondary electrons. All of the equations were then self-consistently solved using the PlasmaNov code for the PIC described in full detail in reference [13] for a primary electron beam energy of 70 eV and a plasma density in the quasi-neutral region of 2 x 10^8 cm^{-3}.

2.3.2.4 Results and Discussion

From the data shown in Figure 44(a), the discharge voltage at which the plasma sheath above the sample collapsed is denoted by the arrows and will be referred to as the 'collapse voltage' for the remainder of the paper. The hBN samples revealed some reduction in the effective SEE from the wall for both types of grooved surfaces. This can be seen by the increase in the collapsed voltage which resulted in the decrease in the SEE as compared to the planar surface. Specifically, the collapse voltage increased by 44% and 89% for the 1 mm and 5 mm grooved samples, respectively. The sheath collapses when there is a sufficient number of secondary electrons to neutralize the potential

barrier of the wall [11]. From these experimental results, it is clear that macroscopic grooving, on the same size scale or larger than the Debye length of the plasma, will reduce SEE requiring increased plasma energies or temperatures to collapse the sheath.

The γ/γ_o ratio in Figure 44(b) represents the SEE reduction caused by the different grooved features, with γ/γ_o = 1 being the planar surface, γ/γ_o = 0.87 being the 1-mm groove and γ/γ_o = 0.67 being the 5-mm groove, as calculated from Eqs. (1-4).

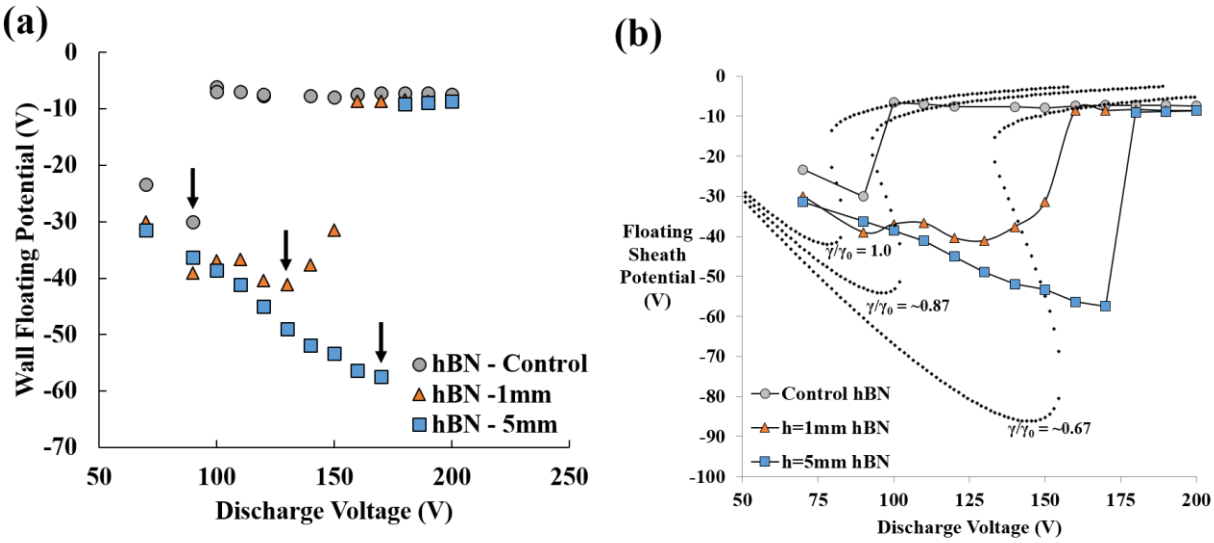

Figure 44. Plots of the floating wall potential vs. discharge voltage for the a) hBN samples with the discharge voltages indicated with arrows. b) hBN with optical trapping model results of SEE trapping using the kinetic sheath model with hBN SEE yield data. The values for the SEE reduction (γ/γ_0) are 1.0 for the control sample, 0.87 for the shallow groove sample, and for the deep groove sample.

Figure 44(b) is a plot of the experimental data from Figure 44(a) overlaid with the predicted curves based on both geometry and one-dimensional plasma kinetics. The control surface showed relatively good agreement with the simple kinetic model's ideal planar surface (γ/γ_0 = 1.0) as both the prediction and experimental values followed a similar sheath potential curve and had approximately similar collapse voltages near 80 V. The postponement of the increased collapse voltage for the h = 5 mm sample was ~ 175 V with the prediction at ~ 150 V. For the h = 1 mm sample, an even higher discrepancy between the experimental collapse voltage of ~150 V was found as compared to the predicted ~ 100 V. In addition, for the h = 1 mm grooves, the experimental data suggested a more gradual transition between a stable and unstable sheath condition. This is noted by the relatively smooth increase in the experimentally-measured sheath potential versus discharge potential. Upon grooving the samples, the simple one-dimensional kinetic model appeared to be insufficient in capturing the physics of the experimentally measured response.

For the planar surface, the assumptions of linear electron trajectories and constant electron temperature and electron and ion densities appear sufficient to explain the collapse voltage conditions. Similarly, the general trend for collapse voltage increasing with a deeper grove was predicted. This can be rationalized that for a deeply-grooved sample, where one could assume that the electron density will be lower deeper into the groove. For example, electron emission that is not normal to the surface will likely collide and be absorbed by the side walls. This would result in a lower number of emitted electrons from regions deeper in the grooves and hence a higher discharge voltage as shown. For the electrons that do emit from the groove, they are likely to be more normal to the surface as they have had to navigate through a high aspect ratio feature to reach the free surface. This may explain why the deeper groove (similar to the planar surface) showed similar sheath potential curve behavior. In contrast, a shallower groove would be able to have more electrons escape and emit at a distribution of angles from the groove, which could have created the conditions for a gradual collapse.

To quantify the dependence of electron density with the grooved feature, Figure 45(a) is the electron density distribution over the emissive grooved surface for the h = 5 mm or deep groove geometry. The numbers 1, 2, 3, and 4 in Figure 45(a) represent separated areas for the floating potential calculation. From this distribution map, it is seen that an accumulation of secondary electrons exists near the groove entrance, whereas the electron density is much lower within the sheath. The electrons appear to preferentially concentrate at the groove entrance because of the

electrostatic forces from the nearby floating walls and their overlapping semi-sheaths. This concentration of electrons, as it related to groove geometry, likely contributes to the deviations from the predicted one-dimensional model noted above. The distribution of potential, measured in volts, over the same grooved hBN surface, Figure 45(b), clearly shows that as the groove deepened, a substantially lower potential formed as compared to anywhere else on the surface of the sample.

By drawing electrons into the lower potential grooves, the surrounding sheath potential reduced. Hence, from these findings, it is possible that at geometries that are a specific fraction of the Debye length, large changes in the electron densities will be found. If similar electron densities develop in Debye-scale surface depressions in HET channels, they could focus ions into the depressions and thus contribute to the growth of the anomalous large-scale erosion ridges observed in some HET lifetime tests, though further work is needed to concretely confirm this effect or its contribution to deep groove erosion patterning [14].

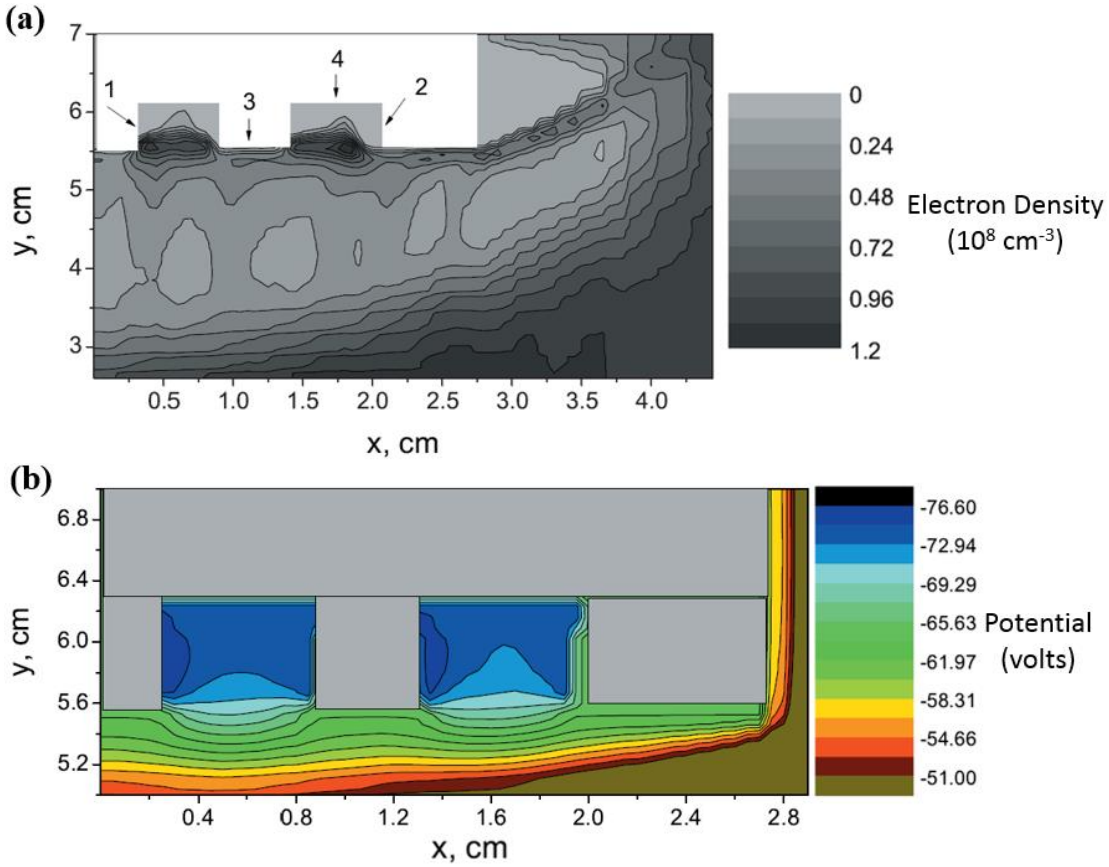

Figure 45. (a)The electron density distribution as modeled using the PIC MCC over the modeled grooved hBN surface, the numbers 1, 2, 3, 4 show separate areas of summation of charged particle currents. (b) The distribution of potential, in Volts, over the modeled grooved sample surface. Two grooves are shown instead of four, as simulated, because x = 0 is the plane of symmetry in the Cartesian coordinates.

2.3.3 Conclusions

In this work, we have compared experimental results with models of electron trapping from hBn surface grooves that were similar to the Debye length of a plasma. The results confirmed that the space-charge saturation of the plasma sheath over a grooved surface was dependent on the size of these geometric grooves. Using a one-dimensional optical model for electron trapping with a plasma kinetic model, reasonable agreement in the prediction of the collapse voltage for a planar surface was found between the experiment and model. When the surface was grooved, some discrepancies between the model predictions and the experimental findings, particularly for the shallowest grooves (h = 1 mm), were noted. This breakdown in the one-dimensional model is believed to be a result of the complex interactions of electron densities near the grooved entrances, which was quantified through a PIC MCC simulation. These findings confirm

that changes in plasma sheath stability will occur for surfaces whose features sizes evolve at these Debye length scales. These results suggest that larger scale features may also need to be considered in HET plasma models where similar surface structures are noted to develop from plasma induced erosion.

2.3.4 References

[1] D. Y. Oh, T. Randolph, S. Kimbrel, and M. Martinez-Sanchez, "End-to-End Optimization of Chemical-Electric Orbit-Raising Missions," *J. Spacecr. Rockets*, vol. 41, no. 5, pp. 831–839, Sep. 2004.

[2] R. R. Hofer, I. G. Mikellides, I. Katz, and D. M. Goebel, "BPT-4000 Hall thruster discharge chamber erosion model comparison with qualification life test data," in *30th International Electric Propulsion Conference, 2007*, pp. 17–20.

[3] K. De Grys, A. Mathers, B. Welander, and V. Khayms, "Demonstration of 10,400 Hours of Operation on 4.5 kW Qualification Model Hall Thruster," *AIAA Pap.*, vol. 6698, p. 2010, 2010.

[4] N. Gascon, M. Dudeck, and S. Barral, "Wall material effects in stationary plasma thrusters. I. Parametric studies of an SPT-100," *Phys. Plasmas*, vol. 10, no. 10, p. 4123, 2003.

[5] S. Barral, K. Makowski, Z. Peradzyński, N. Gascon, and M. Dudeck, "Wall material effects in stationary plasma thrusters. II. Near-wall and in-wall conductivity," *Phys. Plasmas*, vol. 10, no. 10, p. 4137, 2003.

[6] A. Morozov and V. Savel'Ev, "Theory of the near-wall conductivity," *Plasma Phys. Rep.*, vol. 27, no. 7, pp. 570–575, 2001.

[7] T. Burton, A. M. Schinder, G. Capuano, J. J. Rimoli, M. L. Walker, and G. B. Thompson, "Plasma-Induced Erosion on Ceramic Wall Structures in Hall-Effect Thrusters," *J. Propuls. Power*, vol. 30, no. 3, pp. 690–695, 2014.

[8] S. Langendorf and M. Walker, "Effect of secondary electron emission on the plasma sheath," *Phys. Plasmas* 1994-Present, vol. 22, no. 3, p. 33515, 2015.

[9] S. Barral, Y. Jayet, S. Mazouffre, M. Dudeck, E. Veron, and others, "Hall Effect Thruster with an AlN discharge channel," in *29th International Electric Propulsion Conference*, IEPC-2005-152, Princeton, NJ, 2005.

[10] J. Lawless and V. Subramaniam, "Theory of onset in magnetoplasmadynamic thrusters," *J. Propuls. Power*, vol. 3, no. 2, pp. 121–127, 1987.

[11] G. Hobbs and J. Wesson, "Heat flow through a Langmuir sheath in the presence of electron emission," *Plasma Phys.*, vol. 9, no. 1, p. 85, 1967.

[12] D. M. Goebel and I. Katz, *Fundamentals of electric propulsion: ion and Hall thrusters*, vol. 1. John Wiley & Sons, 2008.

[13] I. Schweigert, S. Langendorf, M. Walker, and M. Keidar, "Plasma-Wall Interaction Controlled by Secondary Electron Emission," 2015.

[14] A. M. Schinder, M. Walker, and J. J. Rimoli, "Three-Dimensional Model for Erosion of a Hall-Effect Thruster Discharge Channel Wall," *J. Propuls. Power*, vol. 30, no. 5, pp. 1373–1382, 2014.

[15] R. Chodura, "Plasma–wall transition in an oblique magnetic field," *Phys. Fluids* 1958-1988, vol. 25, no. 9, pp. 1628–1633, 1982.

[16] L. Oksuz and N. Hershkowitz, "Plasma, presheath, collisional sheath and collisionless sheath potential profiles in weakly ionized, weakly collisional plasma," *Plasma Sources Sci. Technol.*, vol. 14, no. 1, p. 201, 2005.

[17] G.-H. Kim, N. Hershkowitz, D. Diebold, and M.-H. Cho, "Magnetic and collisional effects on presheaths," *Phys. Plasmas* 1994-Present, vol. 2, no. 8, pp. 3222–3233, 1995.

[18] Y. Raitses, D. Staack, A. Dunaevsky, and N. Fisch, "Operation of a segmented Hall thruster with low-sputtering carbon-velvet electrodes," *J. Appl. Phys.*, vol. 99, no. 3, pp. 36103–36103, 2006.

[19] S. Langendorf and M. Walker, "Hysteresis and mode transitions in plasma sheath collapse due to secondary electron emission," *J. Appl. Phys.*, vol. 119, no. 11, p. 113305, 2016.

[20] J. Sheehan and N. Hershkowitz, "Emissive probes," *Plasma Sources Sci. Technol.*, vol. 20, no. 6, p. 63001, 2011.

[21] S. J. Langendorf, "Effects of Electron Emission on Plasma Sheaths," 2015.

[22] J. Sheehan, I. Kaganovich, H. Wang, D. Sydorenko, Y. Raitses, and N. Hershkowitz, "Effects of emitted electron temperature on the plasma sheath," *Phys. Plasmas* 1994-Present, vol. 21, no. 6, p. 63502, 2014.

2.4 GT Materials Modeling - Modeling of Micro-Cracking in SiO_2-BN Composites

2.4.1 Introduction

Material-plasma interaction is a very complex phenomenon that leads to changes in the surface of the material (erosion) which, in turn, may affect the plasma configuration. Our research demonstrated that various mechanisms are responsible for the erosion process on the material surface, including differential sputtering and thermal cracking. However, the extent to which each mechanism contributes to the overall erosion patterns across the different scales is not entirely clear. From a modeling perspective, the first step towards elucidating this issue is to generate predictive models that can capture such mechanisms both independently and coupled. During the early years of this project, we developed models for differential sputtering able to predict the evolution of surfaces due to plasma exposure before thermal cracks occur. Subsequently, we developed models based on direct numerical simulation of polycrystalline materials to predict the concentration of thermal stresses at the triple points. Even though the latter models were able to predict stress concentrations, they still lack the capability of predicting crack evolution, which is perhaps the most important aspect of thermo-mechanical erosion due to exposure to plasma. Over the last year of the project, we focused on the development of a concurrent multiscale modeling framework to predict the thermomechanical response of polycrystalline structures including crack nucleation and propagation.

2.4.2 Concurrent Multiscale FE Model

Our framework can be summarized as follows. At the micro-scale, the thermal conductivity within each grain is known to depend on both grain size and shape. That is, the size and morphology of individual grains (and how they are distributed) can alter the temperature distribution within the material, and consequently the distribution of thermal stresses and cracks. To capture these effects, we compute the thermal conductivity within each grain by resorting to the Boltzmann Transport Equation under the relaxation time approximation. The thermal problem is then solved at the macroscale through a classic Fourier heat transport model. Finally, the mechanical solver obtains thermomechanical deformation by explicitly resolving the microscopic geometric features of the material. Due to the non-linear nature of the problem as well as to its irreversible nature, an iterative coupling scheme between the thermal and mechanical aspects of this problem has been devised to achieve converged results.

To capture the effect of arbitrary geometric features within the material on the thermal conductivity tensor, we implemented a ray-casting technique which calculates the distances from the point of phonon emission to the boundaries of the geometric features of interest, e.g. grain boundaries that may cause phonon dispersion [1]. Thus, the thermal conductivity of the material depends on the location of the point of interest (phonon emission) and the nearby geometric features of the material (grain boundaries or external surfaces). Our methodology also allows us to calculate the anisotropic thermal conductivity of grains, mostly found when they have elongated shapes. The thermal conductivity values obtained at the sub-grain level then inform a mesoscale thermal transport model. In this way, the coupling between the scales is achieved at the integration points of the mesh: the full thermal conductivity tensor is computed at each quadrature point considering the actual geometric features of the grain. The sub-grain thermal conductivity tensor is then adopted as material property for the continuum model. Finally, we need to couple the thermal and mechanical problems at the mesoscale, while accounting for the nucleation and evolution of thermal cracks.

The implemented work constitutes a concurrent multiscale scheme, as computation at both scales takes place simultaneously. Ideally, this procedure should be performed after every integration step during computation as thermal conductivity depends on temperature, which evolves with time. In practice, computational cost can be reduced by performing this operation only after a predetermined temperature threshold ΔT_c is attained at the quadrature point. The precise value of the temperature change threshold can be determined through a convergence analysis. The overall solving strategy for the thermos-mechanical evolution of intergranular cracks is depicted in **Figure 46**.

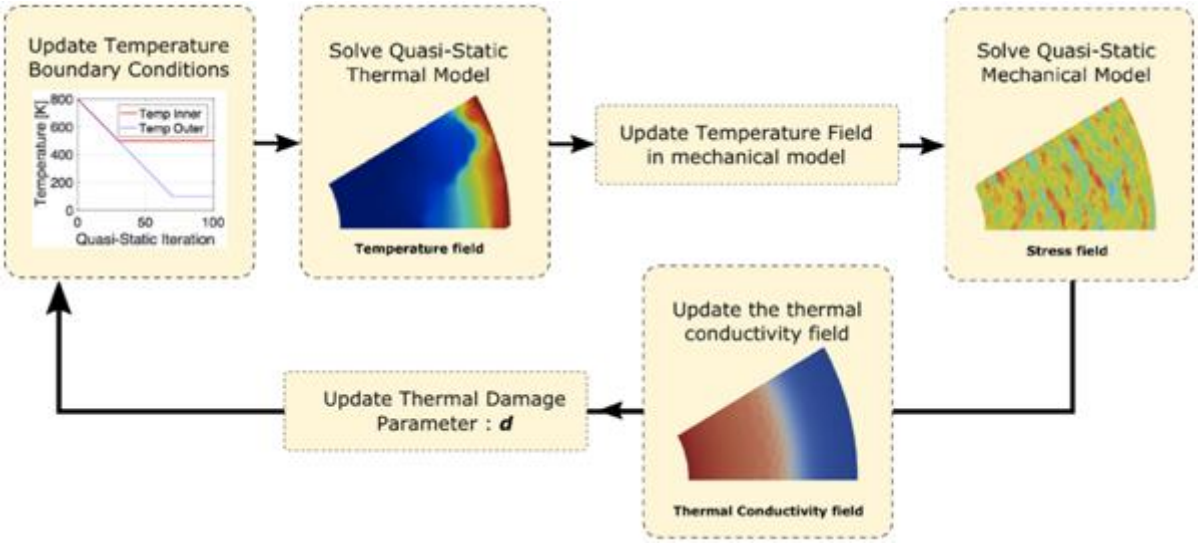

Figure 46. Thermomechanical Framework

2.4.3 Thermal Cracks Modeling

Recently, the focus of our research has been on the modeling and implementation of the thermal cracks. For that part of the work, the coupling needs to be considered at two levels: for the bulk elements and for the interface elements.

The thermomechanical coupling in the bulk material is performed in a standard way such that

$$\sigma_{ij} = C_{ijkl}(\epsilon_{kl} - \alpha_{kl}\Delta T) \tag{14}$$

where σ is the stress tensor, C is the (anisotropic) elasticity tensor for a single crystal, ϵ is the strain tensor, α is the thermal expansion matrix, and ΔT is the change in temperature at a point with respect to a stress-free configuration. It is clear from this expression that the change of temperature directly impacts the stress field.

At the interface between grains where cracks may develop, information needs to be transferred from the mechanical to the thermal model:

- the mechanical opening of the interface element is driven by the traction-separation law. In our code, we implemented the PPR traction-separation law from [2]. Thus, for stress levels large enough, the interface elements start to open - representing crack nucleation and crack propagation.
- the thermal interface element is impacted by the mechanical opening. Indeed, the thermal flux within the element is given by

$$q = (1 - d)D[\![T]\!] \tag{15}$$

where q is the thermal flux, D is the thermal conductivity, $[\![T]\!]$ is the temperature jump and d is the damage parameter accounting for the opening such that $0<d<1$. For $d=0$, the interface elements are undamaged and the thermal flux is unchanged. For $d=1$, the interface element is fully opened and no the thermal flow is annihilated.

The result of the thermomechanical implementation is displayed in **Figure 47**. On the bottom box, the crack between the grains behaves as a thermal barrier and the thermal flux is prevented. On the top box, the opening surrounding the grain is incomplete such that the thermal flux is impacted by not entirely prevented.

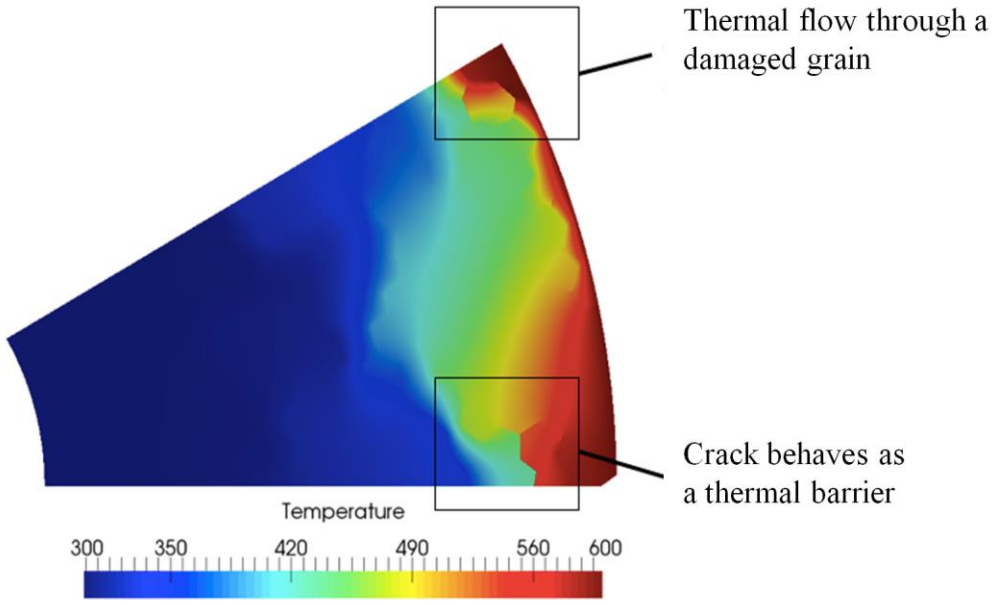

Figure 47. Thermomechanical Example

It is important to highlight how tightly coupled the crack evolution is to the consequent redistribution of heat flux within the material. Once a crack is formed between two grains, the heat flux through their interface is drastically reduced, leading to a redistribution of heat flux within the material. This redistribution, in turn, can lead to the generation of new stress concentration spots which may generate new cracks.

2.4.4 Current Developments and Future Work

Our most recent work focuses on integrating the thermal crack capabilities with our concurrent multiscale model. Preliminary results have proven that the thermal conductivity distribution largely impacts the crack nucleation and propagation process. However, those results are obtained by the use of a uniform mesh to which the thermal conductivity is enforced.

Thus, our present development aims at modeling the impact of the size-effect on the interface elements. Indeed, for graded polycrystals, the regions with smaller grains have more interface elements, leading to some extra artificial compliance. In order to correctly account for this effect, the properties of the interfaces need to take into account the geometric features of the microstructure. The accomplishment of this task is of prime importance to ensure the accuracy of the modeling. Once again, modeling techniques accounting for size-effect in interface modeling have not been reported in the literature.

2.4.5 References

[1]: Bouquet, J. B. and Rimoli, J. J., 2015. A length-dependent model for the thermomechanical response of ceramics. Journal of the Mechanics and Physics of Solids, 82, pp.82-96.

[2]: Park, K., Paulino, G.H. and Roesler, J. R., 2009. A unified potential-based cohesive model of mixed-mode fracture. Journal of the Mechanics and Physics of Solids, 57(6), pp.891-908.

2.5 Georgia Tech Research Institute – Detailed Investigation of Surface Feature Growth during Plasma Erosion

2.5.1 Overview

In years three and four of the AFOSR effort, an experiment was conducted to test whether or not the process of plasma erosion is affected by the presence of mechanical stress within a material. This experiment, called the stressed erosion experiment in subsequent writing, exposed pairs of material samples to an argon plasma. One of the samples in the pair is loaded in uniaxial compression. The other control sample is placed beside the loaded sample in a sheet metal basket and is free to expand. Detailed surface statistics are measured before and after each exposure. In years three and four, fused silica samples were studied. Fused silica is amorphous and has no microstructural detail, so the development of the surface is uninfluenced by the material volume itself. A pattern of sharp-cusped paraboloidal cells are seen to develop on the fused silica surfaces post-exposure, but only in areas where there was initial surface structure present. Analysis of the pre and post-test roughness profile shows that the final surface structures developed from the initial surface structures. Features are amplified to the same extent across all tested samples.

In year five of the effort, further exposures were conducted for the stressed erosion experiment. M26 borosil composite samples were produced and exposed to an argon plasma for 12 hours. The evolution of the M26 samples is governed by the material's heterogeneous microstructure. In addition, the cell patterns developed on the fused silica samples the previous year are explained as a consequence of the angle-dependence of the sputtering yield of the underlying material. Simulations of an erosion process reproduce surfaces that are similar to the final surfaces from initial surface profiles taken on the fused silica samples.

2.5.2 Background

HETs are limited in their useful operating lifespan by the erosion of the ceramic discharge channel walls. Ions, created within the discharge channel, attain sufficient energy during acceleration to sputter material from the channel near the exit-plane of the thruster. The eventual erosion through the channel wall exposes the magnetic circuit of the thruster to the plasma: This is considered the end of life of the thruster. Further operation can sputter ferrous material from the magnets into the spacecraft environment, or disrupt the magnetic circuit leading to unpredictable behavior. Present models for the erosion of the discharge channel wall treat the material as a homogeneous isotropic solid, with an empirically derived sputtering yield law. Present models use axisymmetric 2D models for the plasma and the material geometry, therefore, certain features, such as the anomalous erosion ridges cannot be reproduced by these models. The mechanism for forming the anomalous erosion ridges in HETs is currently unexplained.

In year three, a hypothesis, called the Strain relief hypothesis (SRH) was proposed to potentially explain the formation of the anomalous erosion ridges in HETs. The SRH proposed that the anomalous ridges develop as an instability driven by variations in the strain energy density near the surface of a material under a thermo- mechanical stress. Based on the theory behind the SRH, predictions were made for the range of unstable wavelengths expected as a function of the applied thermo-mechanical stress.

An experiment was designed to test whether and how the process of plasma erosion might depend on mechanical strain energy in a material. Two materials were selected for the experiment: Fused silica and grade M26 boron nitride-silica composite. The fused silica material was selected because it is an amorphous isotropic substance without polycrystals or a heterogeneous microstructure. The erosion process of fused silica is not perturbed by microstructural details in the material. M26 borosil is a composite material with a complex microstructure that is popular in HETs, such as the Russian SPT series, PPSX000-ML, PPS-1350G, and others[1][2][3]. M26 borosil was ordered from St. Gobain, and 3x1x0.25 in. samples were machined.

2.5.3 Model Explaining Year Four Fused Silica Cell Pattern

The cell patterns seen in the exposures of year four are explicable in terms of a simple mechanism: These patterns can result from the angle dependence of the sputtering yield of the fused silica acting on an initial surface. Figure 48 shows these cell patterns. Under normal ion bombardment, the local angle that the surface makes to the incoming ions varies from point to point on the surface and modifies the local sputtering yield and speed of erosion. In sputtering yield theory and experiment, the yield tends to peak at ion incidences of 80º from the surface normal of the target. In a semi-infinite medium, there will be an angle at which the repulsive action of the surface atoms prevents the ions from penetrating into the target (and hence a reduction in yield from the maximum). At lower angles, though, the size of the region of energized target atoms that lie close enough to the surface to allow atoms to escape the target scales as $1/\cos(\theta)$, with θ being the ion angle relative to the surface normal. If the ion mass is greater than the atomic mass

of the target, as is the case for argon and xenon with a SiO_2 target, then $1/\cos(\theta)$ is a good model. If the masses are more nearly equal, the angle dependence scales as $1/\cos(\theta)^{5/3}$ [5].

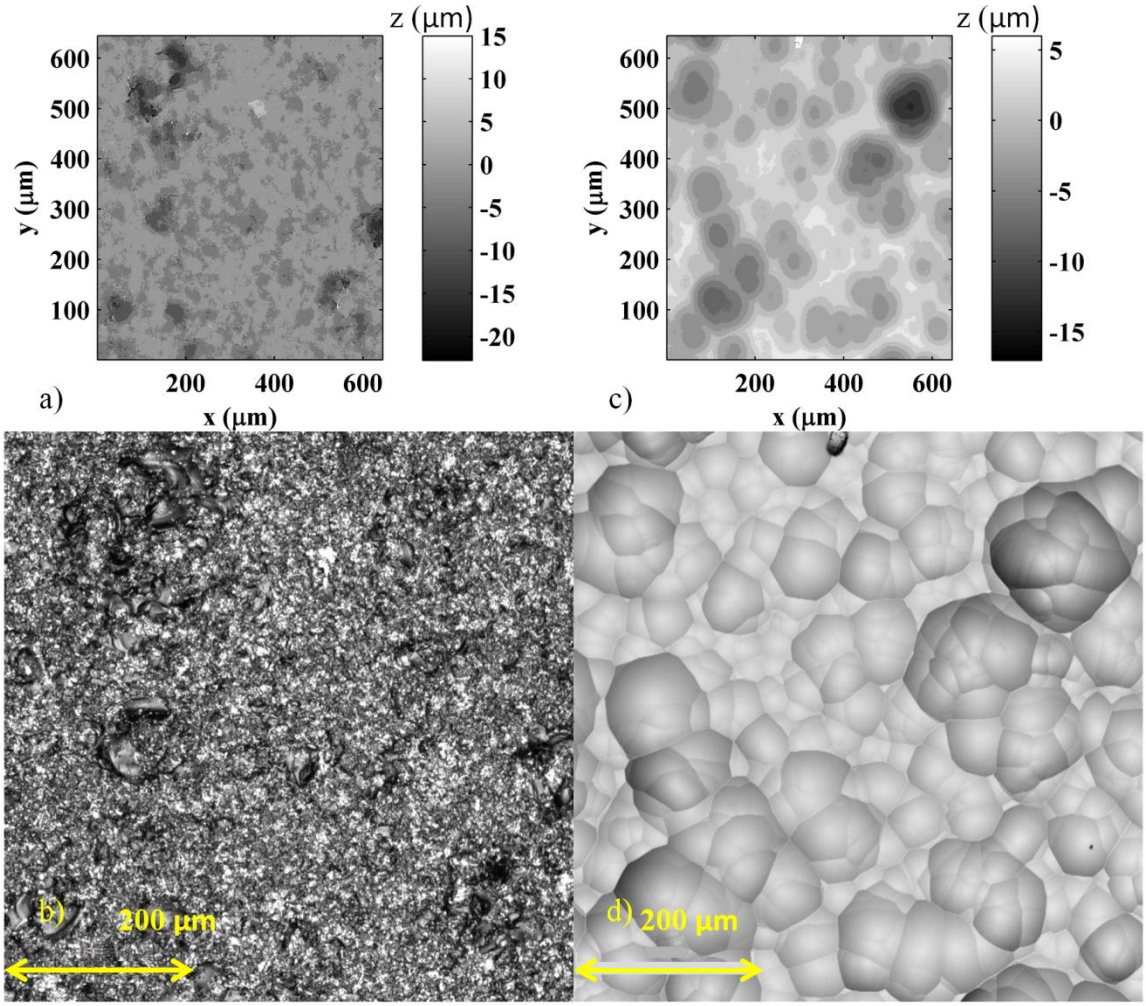

Figure 48. Pre and post-test sample microscopy: SA6 (loaded), 20x, center of exposed surface, a, b) pretest height and laser image, c, d) post-test height and laser image.

For the following analysis, a curve fit of the modified Yamamura form is made to empirical angle dependent yield data collected by Yalin *et al.* for xenon sputtering of fused quartz [6]. The form of the model is given in equation 1, and the coefficients of the model are given in

Table 1. The angle dependence of the yield is shown in **Figure 49**, showing that a 3rd-degree polynomial fit to the data peaks at 55º ion incidence to the surface normal.

$$Y(E,\theta) = f(\theta)g(E) = (B_0 + B_1\theta + B_2\theta^2 + B_3\theta^3)k\sqrt{E}\left(1 - \sqrt{\frac{E_{th}}{E}}\right)^{2.5} \quad (16)$$

Table 1. Yield model fitting coefficients.

Variable	Value	Unit
k	5.0×10^{-3}	$mm^3/C\text{-}eV^{0.5}$
E_{th}	15.0	eV
B_0	1	1
B_1	0	1/deg
B_2	1.11×10^{-3}	$1/deg^2$
B_3	-1.37×10^{-5}	$1/deg^3$

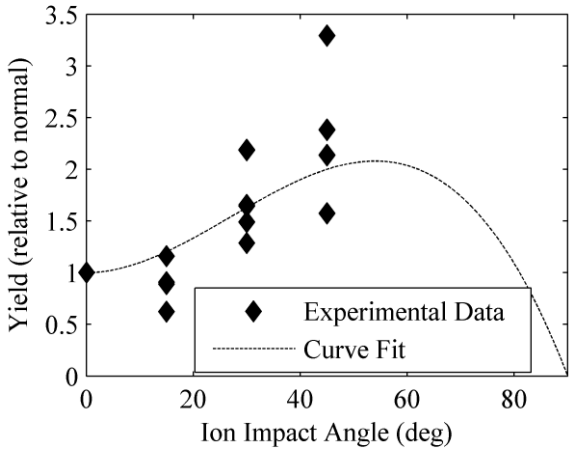

Figure 49. The sputtering yield of fused quartz as a function of ion incidence angle. Data from [6].

Townsend noted that due to the higher sputtering yield of surfaces at an angle to an ion beam, certain initial surface profiles, such as spheres or sinusoidal surfaces would develop, over time, into cones or cusps as erosion proceeds (Townsend, Kelley, & Hartley, 1976). A one-dimensional simulation of the evolution of a surface profile by atomic sputtering is constructed which demonstrates this behavior. The simulation calculates the rate of erosion at each point along a surface profile as a function of the surface normal of the neighboring area elements. The simulation evolves the surface profile in time, producing eroded surface profiles from un-eroded surface profiles. Timesteps of 5 s are used to simulate the evolution of surface profiles with a 0.4 nm horizontal spacing between nodes. The model uses ion current densities of 10 mA/cm^2 and ion energies of 100 eV, similar to conditions in the IAD chamber experiment. **Figure 50** shows relative error as a function of the timestep. This demonstrates that the simulation is well converged for 5-s timesteps. The reference solution is one run at 2.5-s timesteps, to which the other solutions are compared.

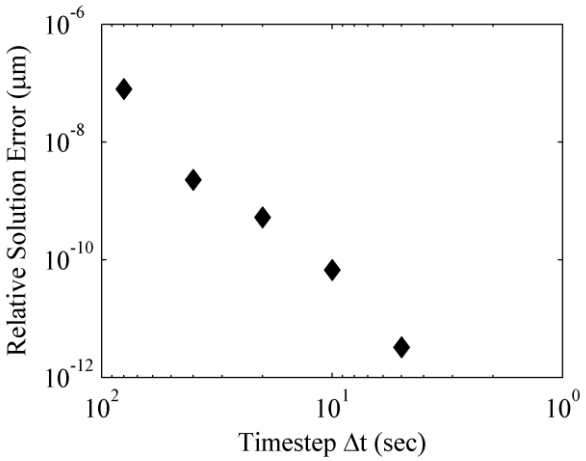

Figure 50. Convergence: Error relative to 2.5 s timestep solution as a function of the timestep.

A 500-μm section is taken from the pre and post-test line-scans for sample SA6. A simulation of the erosion of the top surface is propagated forward in time. At erosion depths similar to the ones reached during the 11-hour experimental exposure, a profile with features similar to the experimental post-test surface is observed. Figure 51 shows the pre and post-test line-scans in blue and several time-steps of the simulated evolution of the top profile in black. The actual surface is two-dimensional, and so there is an extra dimension for the profile to be off-normal to the ion beam. However, even with a one-dimensional simulation, features of a similar depth and profile to the post-test surface develop.

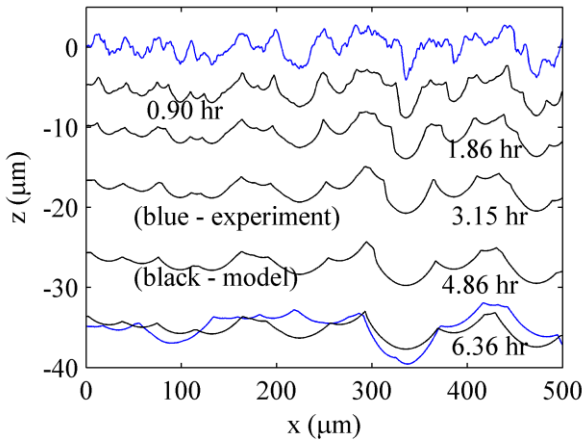

Figure 51. Measured and simulated surface profiles as a function of time.

Fifty, 1-mm long samples of the surface line-scans are propagated to the average erosion depth using the model, and Fourier statistics, similar to those in last year's report are derived. Figure 52 shows a comparison of the amplification function for the experimental and modified profiles for sample SA6. These amplification functions have less spatial frequency resolution than the ones shown in the year four report due to the smaller length of the simulated domain but show the same general trend. Both the simulated and experimental amplification profile show growth of features with a longer wavelength than 0.1 mm, and damping of smaller wavelengths. The amplification statistics agree well until approximately 30 mm^{-1}. The simulation shows less damping at higher spatial frequencies than the physical process. This might point to the existence of a smaller order diffusive process not captured in the model. Arguably, high spatial frequency information, due to the smaller order of magnitude initial and final amplitudes, is noisier and less important to defining the pre and post-test surfaces. The agreement at spatial frequencies below 30 mm^{-1} corresponds to the qualitative similarity between the modeled and experimental post-test surfaces.

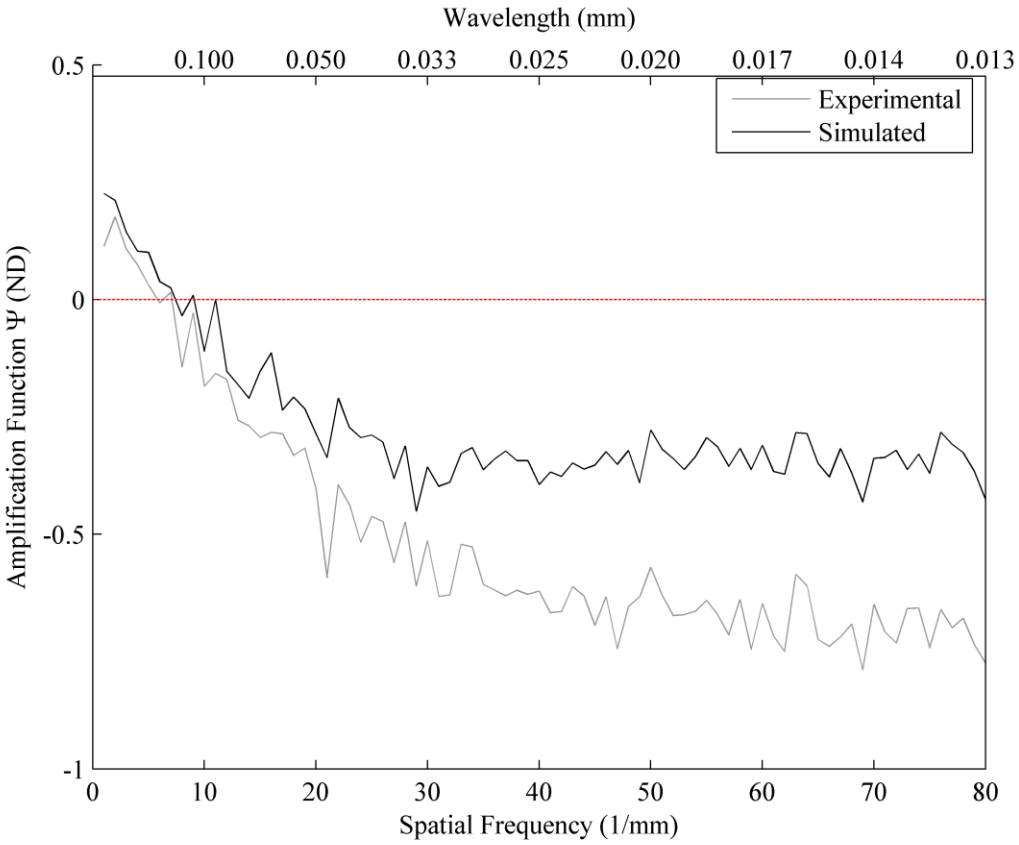

Figure 52. Amplification function Ψ as a function of spatial frequency for experimental and simulated profiles.

2.5.4 Stressed Erosion Experiment: M26 Exposures

In year five, M26 borosil samples are stressed and exposed in the IAD chamber. Borosil is of interest because it is a material, along with pure grades of boron nitride, which are used in Hall Effect Thrusters. Fused silica was studied in previous years because it has a simple amorphous microstructure. Fused silica was studied to isolate the effects of mechanical strain energy on plasma erosion from micro-structurally dependent effects. M26 is studied because it has the most complex microstructure of the materials used in HETs, to see whether the grain-dependent processes or stress concentrations could potentially lead to plasma erosion being sensitive to the presence of mechanical stress. M26 is formed by hot-pressing boron nitride (BN) and silica powder. M26 is a much more complex material than fused silica or purer grades of boron nitride. **Figure 53** shows a SEM image of a representative cross section of M26 and shows that the material is composed of triangular flakes of BN, 10's of μm wide by 100's of nm thick interspersed in a silica matrix. Rectangular M26 samples are acquired from St. Gobain and machined into 3x1x0.25 in. samples to fit within the testing region and test fixture.

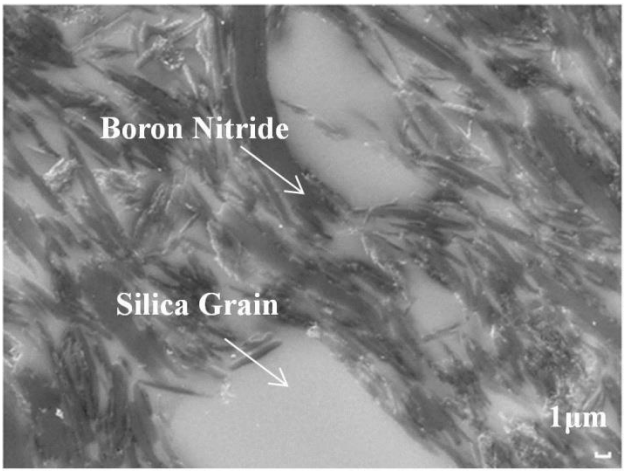

Figure 53. SEM of M26 borosil cross-section

Four 3x1x0.25 in. borosil samples are exposed in two exposures. Each sample is machined, and then the surface is prepared with SiC polishing grit, as with the fused silica samples. A pre-test surface roughness of 1.55 ± 0.10 μm is present due to the polishing. The surfaces of each sample are cleaned with an alcohol bath, water, and dry nitrogen air-blast.

Prior to exposing the M26 samples, one of the 3x1x0.25 samples (SC2) is tested to destruction in the clamp. The sample fails at a strain of 1350 microstrain, or a stress of 30.8 ± 4.2 MPa. Initial test loads are chosen to fall under this threshold to avoid prematurely cracking the samples. Table 2 presents the conditions for each exposure, and the calculated relaxed loads given the equilibrium test temperatures. After each exposure, average erosion depths of 12.5 ± 2.5 μm are developed on each sample surface.

Table 2. M26 borosil exposure conditions.

Exposure	Exp. 1C	Exp. 2C
Loaded Sample	SC1	SC4
Control Sample	SC3	SC5
Initial Stress State (MPa)	23.4 ± 3.1	27.2 ± 3.7
Equilibrium Temp (°C)	241.3 ± 15.6	258.6 ± 2.4
Relaxed Stress State (MPa)	20.6 ± 3.3	24.1 ± 3.4
Relaxed Stress State (% original)	77.6 ± 12.3	77.8 ± 1.1
Duration (hrs)	12	12

Figure 54 shows an overlay of the pre and post-test roughness statistics measured on the exposed surfaces of the borosil samples. Unlike the fused silica roughness statistics, it is not the difference between the pre and post-test statistics that is similar between samples, but the post-test statistics. What this indicates is that the post-test surfaces that develop on the borosil samples are not sensitive to the pre-test surfaces which are present, as they are with fused silica. Unlike fused silica, borosil composites have a complex heterogeneous microstructure, and the difference in the sputtering yield of the components present in the material volume is the dominant influence on how the surface evolves. In the fused silica samples, due to the simple amorphous microstructure, the only input to the evolution of each surface is the pre-existing surface structure. As with the fused silica, no apparent differences are present in the pre and post-test surface statistics between loaded and control samples. Each post-test Fourier transformed roughness curve is the same to within 0.01 μm/wave mode.

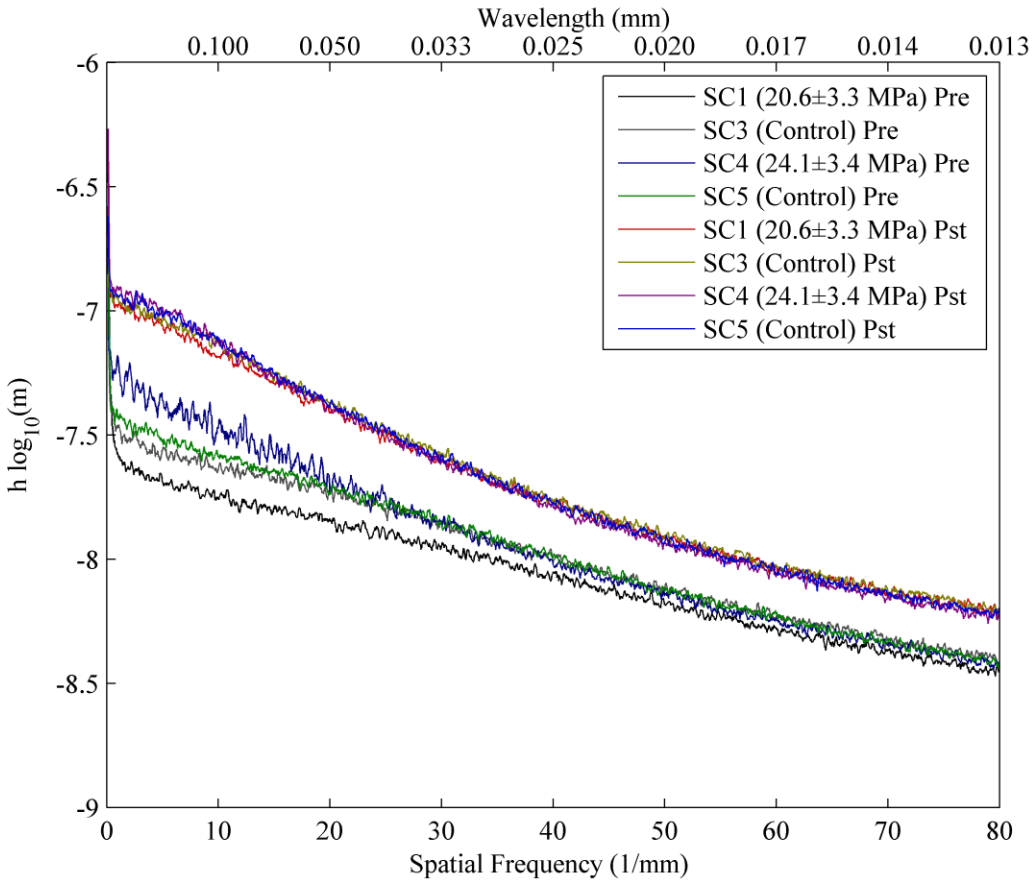

Figure 54. Pre vs. post-exposure averaged Fourier transformed surface amplitude as a function of spatial frequency (surface roughness statistics) for M26.

Figure 55 shows visible light and laser-height-map images of the center of sample SC3. Pre-test, the surfaces are whitish in color, without visible differentiation between silica and BN grains. Post-test, all surfaces have evolved into shapes defined by the nature of the underlying grains. M26 is a composite of boron nitride flakes in a silica matrix. In the post-test images shown, flat flake-like regions (the BN flakes) protrude at random angles from a background of silica. Regions with lots of silica erode slightly faster to form depressions. The nature of the surface appears to be determined almost entirely by the atomic-sputtering properties of the grains. All samples have surfaces with similar appearances. The RMS roughness is greater post-exposure: $4.26 \pm 0.66\ \mu$m. In the post-exposure visible light images, the BN flake/protrusion regions appear darker in color.

Higher magnification images have a finer vertical resolution and show the BN ridge phenomenon more clearly. Figure 56 shows a high-magnification image of a BN rich region in the dark lower-left corner, protruding from the surrounding material.

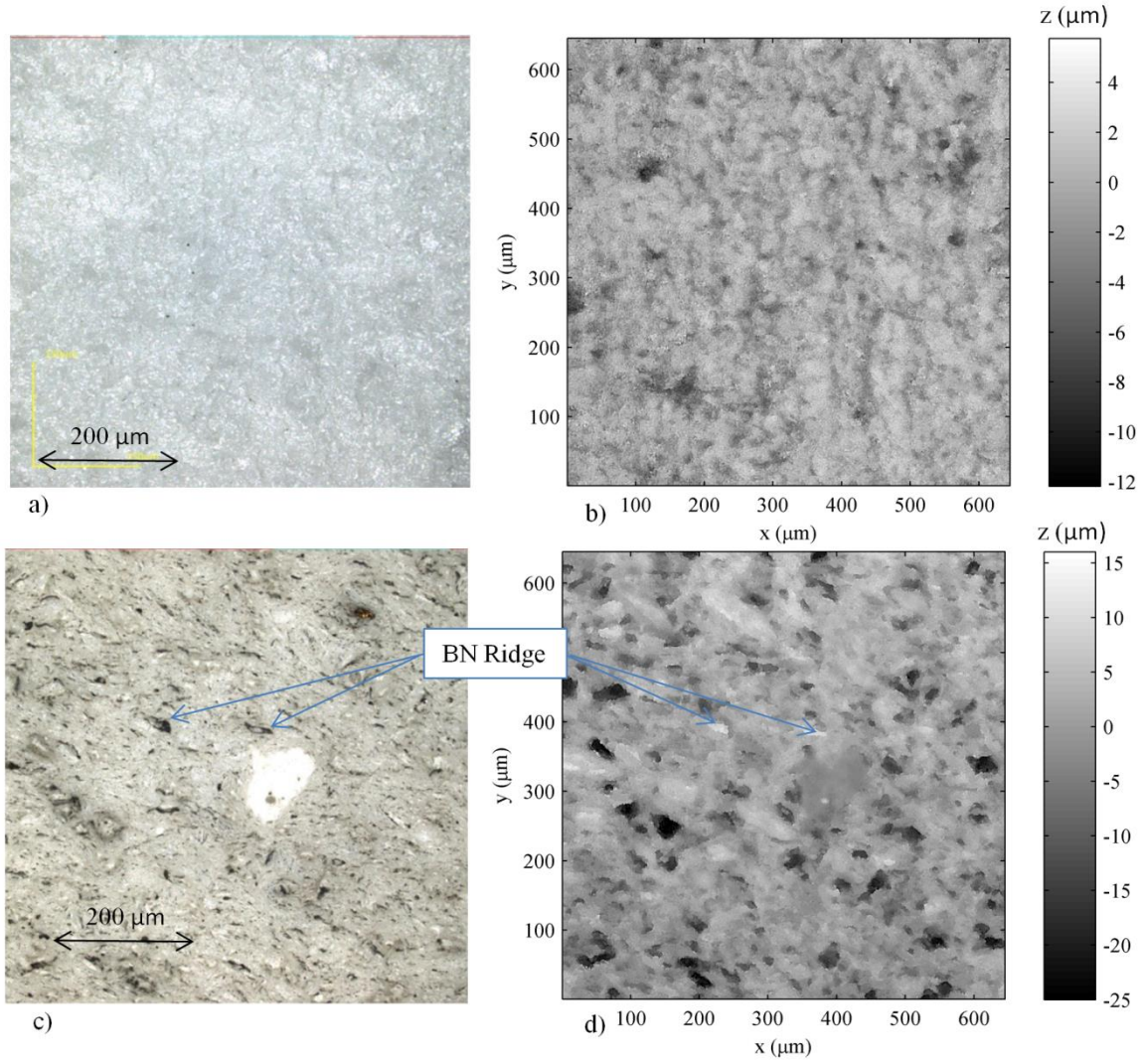

Figure 55. SC3 Pre-exposure surfaces a) visual image, b) laser height map, Post-test surfaces c) visual image, and d) height map.

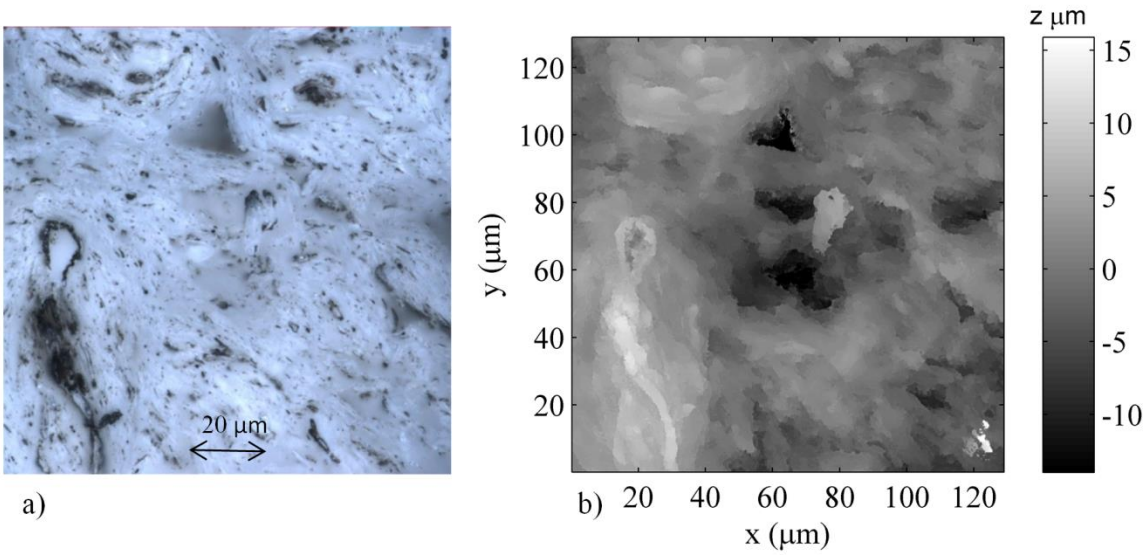

Figure 56. SC1 100x magnification post-exposure a) visible light image, b) laser height map.

The evolution of the M26 surface is insensitive to the differences in the initial surface roughness statistics. Instead, the evolution of the M26 surfaces appears to be governed by the distribution of grains in the material volume. The boron nitride grains and silica matrix each have different sputtering yields, and the difference in the sputtering yields drives the evolution of the surface. Boron nitride flakes protrude from the surface at random angles, as shown in Figure 56. Silica-rich regions erode faster to form depressions.

The evolution of the surface is similar to that investigated with the 3D model for the erosion of heterogeneous materials created in year three. This model used ray-tracing and a 3D model of the distribution of grains within a material surface to reproduce some of the features observed in the eroded channel wall of the AFRL/UM P5 HET. In the model, raytracing was used to determine what portion of a simulated surface profile was exposed to incoming ions at a certain incidence angle. The model calculates the local sputtering rate based on the ion energy and local impact angle, as well as the exposed material type. The surface geometry was updated as time advanced. In the year-three simulations, the simulations used ion incidence angles of 5, 30, 45, and 60º, and the simulation reproduced the cliff-and-valley structures observed in the exit plane of the P5.

The stressed erosion experiment exposed the sample surfaces to ions at normal incidence, unlike in a HET, where ions impact at shallow incidence angles due to being accelerated axially. This was done to maximize the erosion depth attainable in the stable operating time of the plasma source. The 3D heterogeneous sputtering model is used to model the erosion of the M26 at normal incidence. A small-scale material domain model of triangular BN flakes oriented randomly in a silica matrix is constructed. Table 3 presents the parameters used in the simulation. A convergence analysis for the small scale domain model conducted in [18] shows that simulated values for RMS roughness attained using timesteps of 0.5 s came to within 5% of the asymptotic value using 0.05-s timesteps. The simulated surface was propagated to 12.5-μm average erosion depth, as in the experiment.

Figure 58 shows the simulated surface with exposed material and variations in surface height. While the distribution of grain sizes may need to be adjusted to obtain a material domain exactly analogous to the domain imaged in Figure 56, the similar qualitative behavior is seen to result from the model. Regions of high BN concentration tend to protrude from the more silica-rich regions of the matrix, leading to areas of higher elevation. Two such regions are circled in the material map and height-map of Figure 58.

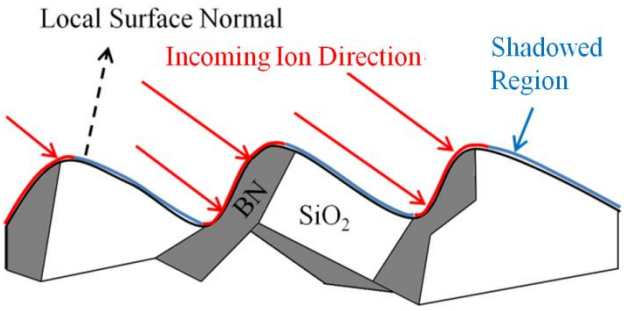

Figure 57. Ray-tracing approach to modeling differential sputtering.

Table 3. Model Parameters

Parameter	Value	Unit
Surface Mesh Size	200x200	
Domain Dimensions (x×y×z)	120x120x50	μm
Triangle Length Scale	5.0 - 20.0	μm
Triangle Thickness Scale	0.1 - 1.5	μm
Ion Beam Energy	120	eV
Ion Beam Number Density	1.00×10^{17}	$\#/m^3$
Ion Beam Angle	Normal	
Timestep	0.5	s

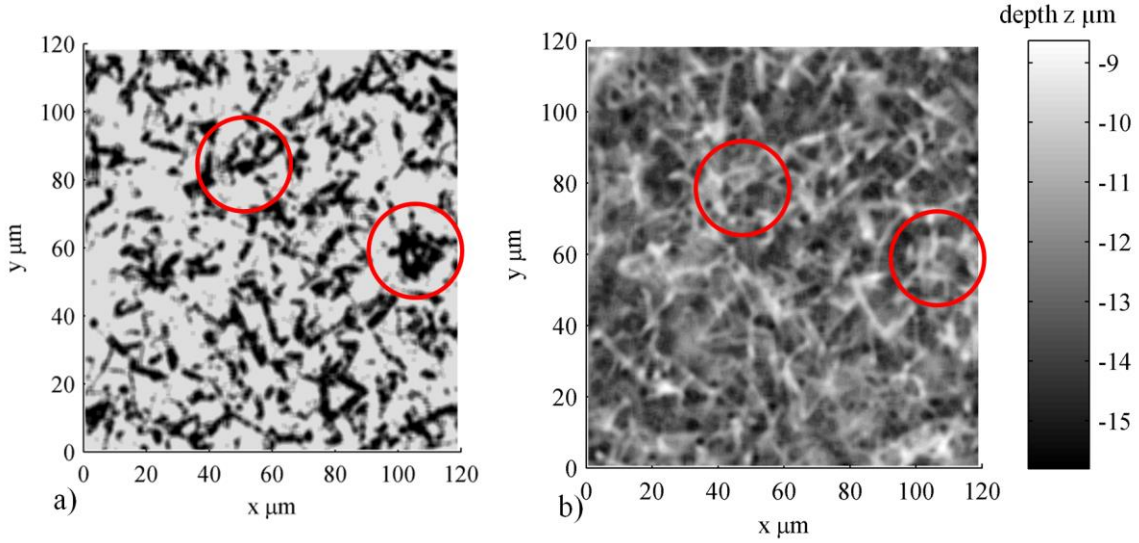

Figure 58. Simulated domain a) exposed material (black is BN, light gray is SiO_2) b) height profile. Regions of high BN concentration and larger heights are circled.

2.5.5 Summary of Results

In year five, the stressed erosion experiment was continued, and new data was taken. First: The results for the fused silica exposures in year four were explained. The angle dependence of the sputtering yield of the fused silica can reproduce the formation of the sharp-cusped cell patterns and surface statistics observed for fused silica.

Second, new exposures were conducted with M26. For amorphous isotropic fused silica, the evolution of the surface profile is dependent only on the initial surface profile. No microstructural detail is present in the material to affect the process. Unlike for fused silica, M26 is a complex heterogeneous composite material composed of BN grains in a silica matrix. The evolution of the M26 surface is insensitive to the initial surface roughness (for initial roughnesses on the order of 1.55±0.10 μm). The evolution of the surface is instead governed by the difference in sputtering yield between grains of different types within the material volume.

Third, for both fused silica and M26 boron nitride, no difference in the evolution of each surface has been detected for material stresses up to 25.0 MPa, for pre-roughened surfaces. In order to detect an effect due to mechanical stress, a difference of more than 0.15 (nondimensional) for the amplification function, or greater than 0.01 μm/wave mode would have to be seen in the final roughness statistics of the loaded sample compared with the control sample.

2.5.6 References

[1] M. Gamero-Castaño and I. Katz, "Estimation of Hall thruster erosion using HPHall," Princeton University, 2005.

[2] S. Mazouffre, "Plasma induced erosion phenomena in a Hall thruster," in Recent {Advances} in {Space} {Technologies}, 2003., Istanbul, Turkey, 2003.

[3] S. Mazouffre, P. Echegut and M. Dudeck, "A calibrated infrared imaging study on the steady state thermal behaviour of Hall effect thrusters," Plasma Sources Science and Technology, vol. 16, no. 1, p. 13, 2007.

[4] A. J. Satonik and J. L. Rovey, "Modification of Boron Nitride Ceramic to Replicate Hall Effect Thruster Surface Wear," in 50th Aerospace Sciences Meeting, Nashville, TN, 2012.

[5] P. Townsend, J. Kelley and N. Hartley, "Chapter 6: Sputtering," in Ion implantation, sputtering, and their applications, Academic Press, 1976, pp. 111 - 147.

[6] A. P. Yalin, B. Rubin, S. R. Domingue, Z. Glueckert and J. D. Williams, "Differential Sputter Yields of Boron Nitride, Quartz, and Kapton Due to Low Energy Xe+ Bombardment," AIAA Paper, vol. 5314, 2007.

Summary

The efforts of each of the teams culminated into a significant increase in knowledge related to plasma-wall interactions. The High-Power Electric Propulsion Lab at Georgia Institute of Technology continued their research into plasma sheath physics. Hysteresis is observed in the floating potential of wall material samples immersed in a low-temperature plasma, as the energy of a prevalent non-thermal electron population is varied from 30-180 eV. Hysteresis is found to be due to secondary electron emission from the wall material surface. Immersed LaB_6-coated steel and roughened boron nitride (NB) wall material samples are mounted on the face of a radiative heater, and the wall temperature is controlled from 50-400 ºC. Thermionic emission from the LaB_6-coated sample is not significant at these temperatures. The energy of the primary plasma electrons is increased above 110 and 130 eV for LaB_6 and rough BN respectively. As primary electron energy is subsequently decreased, the floating potentials do not "un-collapse" until lower energies of 80 and 100 eV, respectively. The hysteresis behavior agrees with a kinetic model. These results may help explain observations of global hysteresis and mode transitions in bounded plasma devices with dielectric walls.

The University of Alabama performed two studies in year five. The first effort investigated the influence of surface roughness on electron emission from graphite and graphite coated HET materials. In this study, the effect of surface roughness on SEE in graphite and graphite coated channel wall materials is investigated. Surfaces were polished by metallographic polishing. The smoothest surface produced the highest SEE yield, as expected. However, a moderately rough surface was found to have a lower yield than the roughest surface. This trend is also observed in an eroded channel wall, where the roughest surface did not yield the lowest SEE. This suggests that the surface roughness has a characteristic length scale associated with emission.

The second study was done in concert with the sheath experiments conducted at HPEPL: Investigating the effect of Debye-scale surface features on the space-charge saturation of plasma sheaths. A series of grooved hexagonal boron nitride (hBN) surfaces with different aspect ratios, designed to mimic the anomalous erosion ridges, were exposed to an argon plasma. The change in the plasma sheath characteristics, particularly the 'collapse voltage' which occurs when the discharge voltage is sufficient to produce enough secondary electrons to collapse the sheath, was found to be 44% and 89% higher for a 1 mm and 5 mm grooved depth compared to a planar surface. A ray-trace optical model for secondary electron emission reduction with a one-dimensional kinetic model for the plasma was used to simulate the responses. The simple model was found to be inadequate to capture the correct collapse voltage, which is attributed to a variation of electron and ion charge densities near the groove entrance. Results were found which provide insights into how larger length-scale surface topology features, on the order of the Debye length, influence the dynamic interactions between a surface and plasma sheath.

In year five, the Computational Solid Mechanics Lab at Georgia Tech created models of the development of cracks in polycrystalline materials. This work builds on efforts in earlier years to directly numerically model thermal stress concentrations in polycrystals. Preliminary results have proven that the thermal conductivity distribution largely impacts the crack nucleation and propagation process. CSML contributed towards a concurrent multi-scale model capable of predicting the thermo-mechanical response of polycrystalline structures including crack nucleation and propagation.

The cell pattern that was observed to occur on fused silica samples in the year-four exposures in the stressed erosion experiment was modeled successfully as the result of the angle-dependence of the sputtering yield of fused silica. An erosion model accounting for the angle dependence of sputtering is capable of reproducing both qualitative and quantitative aspects of the cusped cell pattern. The evolution of fused silica surfaces is found to be explained by a local mechanism that autonomously evolves initial surfaces to final surfaces without input from the underlying surface structure, or any apparent effect from the presence of mechanical stress.

The stressed erosion experiment is extended to a new material: M26 borosil, a common channel wall material used in HETs. Unlike amorphous, isotropic fused silica, M26 has a complex heterogeneous microstructure. Samples pairs are placed in a test fixture. The experiment samples are loaded to 20.6 ± 3.3 MPa and 24.1 ± 3.4 MPa, respectively. The control samples are unloaded and free to expand. Each sample pair is exposed for 12 hours to argon plasma in GTRI's IAD chamber. The evolution of M26 is found to be governed by the material microstructure, unlike the fused silica samples. While the fused silica post-exposure surfaces had statistics which were proportional to the pre-exposure surface statistics, the M26 samples had post-exposure statistics which were *independent* of the pre-exposure statistics. M26 sample surfaces are governed by the heterogeneous microstructure and the difference in sputtering yield between the boron nitride and silica grains. Again, no differences between the post-test surface statistics for the loaded and unloaded samples are found. The loaded and unloaded post-test surface statistics are similar to within 0.01 μm/wave mode. No evidence for mechanical stress in materials affecting plasma erosion of surfaces at these erosion depths, and for stresses of 25.0 MPa has been found.

2.5.7 Acknowledgements

The authors gratefully thank grant AFOSR-FA9550-11-1-0160 for supporting this work.

2.5.8 Team Publications

Conference Publications:

- Brieda, L., Keidar, M., "Development of the Starfish Plasma Simulation Code and Update on Multiscale Modeling of Hall Thrusters," 48th AIAA/ASME/SAE/ASEE Joint Propulsion Conference (JPC), Atlanta, GA, Aug., 2012
- Burton, T., Schinder, A., Capuano, G., Rimoli, J., Walker, M. L. R., Thompson, G., "Erosion Characteristics in a Composite BN-SiO2 Hall Effect Thruster Chamber Wall," 37th Annual Conference on Composites, Materials, and Structures hosted by the United States Advanced Ceramics Association, 28-31 January 2013.
- Langendorf, S., Walker, M. L. R., L. Rose, Keidar, M., Brieda, L., "Study of the Plasma-Wall Interface –Measurement and Simulation of Sheath Potential Profiles," 49th AIAA/ASME/SAE/ASEE Joint Propulsion Conference (JPC), San Jose CA, July 15-17, 2013
- Schinder, A., Walker, M. L. R., Rimoli, J., "3D Model for Atomic Sputtering of Heterogeneous Ceramic Compounds," 49th Joint Propulsion Conference and Exhibit, San Jose, CA, July 15-17, 2013.
- Langendorf, S., Walker, M. L. R., Rose, L., Brieda, L., Keidar, M., "Effect of ion-neutral collisions on sheath potential profile," 33rd International Electric Propulsion Conference (IEPC), Washington DC Oct. 6-9, 2013.
- Geng, J., Rose, L., Brieda, L., Keidar, M., "On the potential solver in Hall Thruster," 33rd International Electric Propulsion Conference (IEPC), Washington DC Oct. 6-9, 2013.
- Schweigert, I., Langendorf, S., Keidar, M., Walker, M. L. R., "Sheath Structure Transition Controlled by Secondary Electron Emission at Low Gas Pressure," 67th Annual Gaseous Electronics Conference, Raleigh, NC, November 2-7, 2014.
- Langendorf, S., Walker, M. L. R., "Effects of Wall Material, Wall Temperature, and Surface Roughness on Plasma Sheath," 50th Joint Propulsion Conference and Exhibit, Cleveland, OH, July 28-30, 2014.
- Langendorf, S., Walker, M. L. R., "Effects of Wall Material and Surface Roughness on the Plasma Sheath," 41st IEEE International Conference on Plasma Science, Washington DC, USA, May 25–29, 2014.
- Schweigert, I., Langendorf, S., Walker, M. L. R., Keidar, M., "Plasma-Wall Interaction Controlled by Secondary Electron Emission," IEPC-2015-343, 34th International Electric Propulsion Conference, Kobe-Hyogo, Japan, July 4-10, 2015.
- Burton, T. S., Butts, D., Joly, A., Thompson, G. B., Vacuum Plasma Sprayed LaB_6 Microstructure and Surface Emission Characteristics TMS 2016 Annual Meeting & Exhibition, Nashville, Tennessee, February 14-18, 2016
- Schinder, A. M., Rimoli, J. J., Walker, M. L. R., "Plasma Erosion of Stressed Fused Silica and M26 Borosil," AIAA/SAE/ASEE 52nd Joint Propulsion Conference and Exhibit, Salt Lake City, Utah, July 25-27, 2016.

Peer-Reviewed Publications:

- Brieda, L., Keidar, M., "Plasma-wall interaction in Hall thrusters with magnetic lens configuration," J. Appl. Phys., vol. 111, 123302, 2012.
- Geng, J., Brieda, L., Rose, L., Keidar, M., "On applicability of the thermalized potential solver in simulations of the plasma flow in Hall Thrusters," J. Applied Physics, 114, 103305, 2013.
- Burton, T. S., Schinder, A., Capuano, G., Rimoli, J., Walker, M. L. R., Thompson, G. B., "Plasma Induced Erosion Microstructures in Boron Nitride-Silica Composites," Journal of Propulsion and Power, 2014. 1-6.

- Schinder, A., Walker, M. L. R., Rimoli, J., "3D Model for Erosion of a Hall Effect Thruster Discharge Channel Wall," Journal of Propulsion and Power, Volume 30, Number 5, September-October 2014, pg. 1373-1382.
- Schweigert, I., Langendorf, S., Walker, M. L. R., Keidar, M., "Sheath structure transition controlled by secondary electron emission," Plasma Sources Science and Technology, February 2015, Vol. 24, No. 2, 025012.
- Langendorf, S., Walker, M. L. R., "Effect of Secondary Electron Emission on the Plasma Sheath," Physics of Plasmas, March 2015, Vol. 22, 033515 (2015).
- Langendorf, S. J., Walker, M. L. R., "Hysteresis and Mode Transitions in Plasma Sheath Collapse Due to Secondary Electron Emission," Journal of Applied Physics, Volume 119, March 2016, pp. 113305 1-5.
- Schinder, A., Rimoli, J., Walker, M. L. R., "Investigation of Plasma Material Erosion Under Mechanical Stress," Journal of Propulsion and Power, July 2016. – Accepted.
- Burton, T. S., Langendorf, S., Walker, M. L. R., Schweigert, I., Keidar, M., Thompson, G. B., "Effect of Debye-scale Surface Features on Space Charge Saturation of Plasma Sheaths" under review Journal of Propulsion and Power 2016
- Burton, T. S., Back, T. C., Fairchild, S. B., Thompson, G. B., "Influence of surface roughness on electron emission from graphite and a graphite-coated hall effect thruster chamber wall materials," under review, Journal of Applied Surface Science, 2016
- Burton, T. S., Back, T. C., Fairchild, S. B., Butt, D, Thompson, G. B., "Vacuum Plasma Sprayed LaB_6 Microstructure and Surface Emission Characteristics" in preparation for submission, Journal of Thermal Spray Technology 2016

References

[1] Jahn, R. G., Dover Publications, 2006, ISBN 978-0486450407.
[2] Kim, K-S, JA Hurtado, and H Tan. "Evolution of a Surface-Roughness Spectrum Caused by Stress in Nanometer-Scale Chemical Etching." *Physical Review Letters* 83, no. 19 (1999): 3872.

AFOSR Deliverables Submission Survey

Response ID:7157 Data

1.

Report Type

Final Report

Primary Contact Email

Contact email if there is a problem with the report.

mitchell.walker@ae.gatech.edu

Primary Contact Phone Number

Contact phone number if there is a problem with the report

4043852757

Organization / Institution name

Georgia Institute of Technology

Grant/Contract Title

The full title of the funded effort.

Comprehensive Study of Plasma-Wall Sheath Transport Phenomena

Grant/Contract Number

AFOSR assigned control number. It must begin with "FA9550" or "F49620" or "FA2386".

FA9550-11-1-0160

Principal Investigator Name

The full name of the principal investigator on the grant or contract.

Mitchell L. R. Walker

Program Officer

The AFOSR Program Officer currently assigned to the award

Mitat Birkan

Reporting Period Start Date

01/31/2011

Reporting Period End Date

06/30/2016

Abstract

In order to facilitate the development of the next generation of electric propulsion (EP) devices for USAF space assets and overcome current limitations in power density and specific mass, investigators from Georgia Institute of Technology (GT), University of Alabama (UA), and George Washington University (GWU) performed a comprehensive multidisciplinary study on the nature and transport properties of the interaction between a plasma and a confining wall material. Hysteresis effects observed in the floating potential of wall material samples immersed in a low-temperature plasma were studied. Hysteresis is found to be due to secondary electron emission from the wall material surface. The impact of surface roughness and sheath-scale surface profiles on space charge saturation of plasma sheaths was investigated. The preliminary results of models have proven that the thermal conductivity distribution largely impacts the crack nucleation and propagation process in boron nitride. The experimental investigation of the erosion of stressed materials was continued for fused silica and M26 borosil. The work shows that the evolution of the M26 surface is governed by the complex microstructure of the material.

Distribution Statement

This is block 12 on the SF298 form.

Distribution A - Approved for Public Release

Explanation for Distribution Statement

If this is not approved for public release, please provide a short explanation. E.g., contains proprietary information.

SF298 Form

Please attach your SF298 form. A blank SF298 can be found here. Please do not password protect or secure the PDF The maximum file size for an SF298 is 50MB.

sf0298_10252016.pdf

Upload the Report Document. File must be a PDF. Please do not password protect or secure the PDF . The maximum file size for the Report Document is 50MB.

AFOSR_Final Report_Georgia Tech_10252016.pdf

Upload a Report Document, if any. The maximum file size for the Report Document is 50MB.

Archival Publications (published) during reporting period:

• Brieda, L., Keidar, M., "Plasma-wall interaction in Hall thrusters with magnetic lens configuration," J. Appl. Phys., vol. 111, 123302, 2012.
• Geng, J., Brieda, L., Rose, L., Keidar, M., "On applicability of the thermalized potential solver in simulations of the plasma flow in Hall Thrusters," J. Applied Physics, 114, 103305, 2013.
• Burton, T. S., Schinder, A., Capuano, G., Rimoli, J., Walker, M. L. R., Thompson, G. B., "Plasma Induced Erosion Microstructures in Boron Nitride-Silica Composites," Journal of Propulsion and Power, 2014. 1-6.
• Schinder, A., Walker, M. L. R., Rimoli, J., "3D Model for Erosion of a Hall Effect Thruster Discharge Channel Wall," Journal of Propulsion and Power, Volume 30, Number 5, September-October 2014, pg. 1373-1382.
• Schweigert, I., Langendorf, S., Walker, M. L. R., Keidar, M., "Sheath structure transition controlled by secondary electron emission," Plasma Sources Science and Technology, February 2015, Vol. 24, No. 2, 025012.
• Langendorf, S., Walker, M. L. R., "Effect of Secondary Electron Emission on the Plasma Sheath," Physics of Plasmas, March 2015, Vol. 22, 033515 (2015).
• Langendorf, S. J., Walker, M. L. R., "Hysteresis and Mode Transitions in Plasma Sheath Collapse Due to Secondary Electron Emission," Journal of Applied Physics, Volume 119, March 2016, pp. 113305 1-5.
• Schinder, A., Rimoli, J., Walker, M. L. R., "Investigation of Plasma Material Erosion Under Mechanical Stress," Journal of Propulsion and Power, July 2016. – Accepted.

New discoveries, inventions, or patent disclosures:

Do you have any discoveries, inventions, or patent disclosures to report for this period?

No

Please describe and include any notable dates

Do you plan to pursue a claim for personal or organizational intellectual property?

Changes in research objectives (if any):

None

Change in AFOSR Program Officer, if any:

N/A

Extensions granted or milestones slipped, if any:

None

AFOSR LRIR Number

LRIR Title

Reporting Period

Laboratory Task Manager

Program Officer

Research Objectives

Technical Summary

Funding Summary by Cost Category (by FY, $K)

	Starting FY	FY+1	FY+2
Salary			
Equipment/Facilities			
Supplies			
Total			

Report Document

Report Document - Text Analysis

Report Document - Text Analysis

Appendix Documents

2. Thank You

E-mail user

Oct 26, 2016 00:00:53 Success: Email Sent to: mitchell.walker@ae.gatech.edu